

University of St Andrews



Full metadata for this thesis is available in
St Andrews Research Repository
at:

<http://research-repository.st-andrews.ac.uk/>

This thesis is protected by original copyright

Exciton Saturation, Spin Relaxation And All-Optical Switching In InGaAs(P) Multiple Quantum Wells

James T. Hyland, B.Sc. M.Sc.



*J.F. Allen Physics Research Laboratories
Department of Physics and Astronomy
University of St Andrews
North Haugh
St Andrews KY16 9SS
Scotland*

A thesis submitted to the University of St Andrews
in application for the degree of Doctor of Philosophy

January 1999





Tu

D312

I, James Theodore Hyland, hereby certify that this Thesis, which is approximately 23000 words in length, has been written by me, that it is the record of work carried out by me and that it has not been submitted in any previous application for a higher degree.

Date: 25/1/99 Signature of candidate

I was admitted as a research student in 1995 and as a candidate for the degree of Doctor of Philosophy in Physics. The higher study for which this is a record was carried out in the University of St. Andrews between 1995 and 1998.

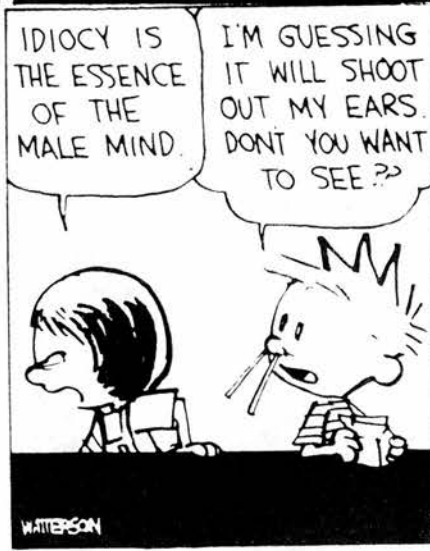
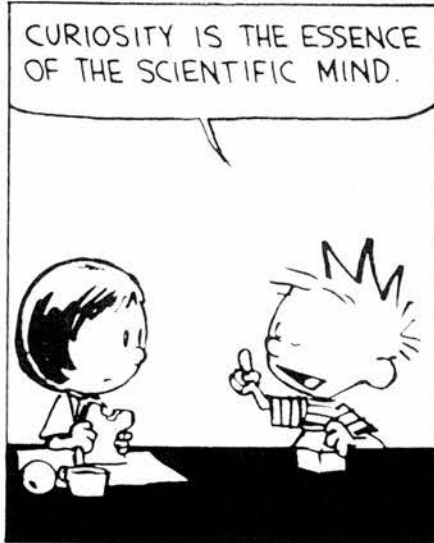
Date: 25/1/99 Signature of candidate

I hereby certify that the candidate has fulfilled the conditions of the Resolution and Regulations appropriate for the degree of Doctor of Philosophy in the University of St. Andrews and that the candidate is qualified to submit this thesis in application for that degree.

Date... 27/1/99 ... Signature of supervisor

In submitting this thesis to the University of St. Andrews I understand that I am giving permission for it to be made available for use in accordance with the regulations of the University Library for the time in force, subject to any copyright vested in the work not being affected thereby. I also understand that the title and abstract will be published, and that a copy of the work may be made and supplied to any bona fide library or research worker.

Date... 25/1/99 ... Signature of candidate.



WATTERSON

“Report writing, like motor-car driving and love-making, is one of those activities which almost every Englishman thinks he can do well without instruction. The results are of course usually abominable.”

Tom Margerison

Abstract

This thesis presents an investigation of exciton absorption saturation processes in InGaAs(P) / InGaAsP multiple quantum wells using both picosecond and femtosecond duration optical pulses.

Exciton saturation was investigated with a degenerate pump-probe study employing circularly polarised light. The bandwidth of the near 100 fs pulses allowed the effects of Coulomb screening to be easily separated from those of lineshape broadening. The temporal resolution of the experiments allowed exciton-exciton saturation mechanisms to be determined. A rate equation analysis of the data allowed a comparison of the Coulomb screening and phase space filling contributions to the exciton saturation, while a comparison of the results obtained with both femtosecond and picosecond pulses showed that broadening had little significance in the samples under investigation.

An investigation into electron spin relaxation at room temperature has been carried out as a function of quantum well width. The observed increase in electron spin relaxation time with decreasing well width are in good agreement with previously reported results, suggesting that the D'Yakonov-Perel mechanism is the dominant spin flip mechanism for electrons in InGaAs(P) / InGaAsP quantum wells at room temperature.

The first demonstration of a spin dependent all-optical polarisation switch operating at the preferred telecommunications wavelength around 1.5 μm is achieved. The switch makes use of the spin dependent refractive index change in multiple quantum wells giving observed switch recovery time of 4.8 ps, determined by the electron spin relaxation time, making it a potentially useful element for future all-optical soliton communication systems.

| | | |
|-----------|--|----|
| Chapter 1 | Introduction | 3 |
| 1.1 | References | 7 |
| Chapter 2 | Properties of quantum wells | 8 |
| 2.1 | Summary | 8 |
| 2.2 | Growth considerations | 8 |
| 2.3 | Bulk III-V semiconductors | 9 |
| 2.4 | Multiple quantum wells | 11 |
| 2.5 | Quantisation of energy levels | 13 |
| 2.6 | Density of states | 17 |
| 2.7 | Excitons | 19 |
| 2.8 | Optical excitation | 20 |
| 2.9 | Resonant optical nonlinearities | 22 |
| 2.9.1 | Coulomb screening | 22 |
| 2.9.2 | Band and phase space filling | 23 |
| 2.9.3 | Lineshape broadening | 24 |
| 2.10 | References | 26 |
| Chapter 3 | Experimental techniques | 27 |
| 3.1 | Summary | 27 |
| 3.2 | Introduction | 27 |
| 3.3 | Linear absorption | 27 |
| 3.4 | Degenerate time-resolved pump-probe | 29 |
| 3.4.1 | Coupled cavity mode-locked KCl:Ti ⁰ (1) colour-centre laser | 29 |
| 3.4.2 | Titanium:sapphire pumped PPLN OPO | 32 |
| 3.4.3 | Diagnostics | 34 |
| 3.4.4 | Pump-probe experimental set-up | 37 |
| 3.4.5 | Spin relaxation studies | 38 |
| 3.5 | References | 40 |
| Chapter 4 | Sample description and optical properties | 41 |
| 4.1 | Summary | 41 |
| 4.2 | Introduction | 41 |
| 4.3 | Sample MR535 | 42 |
| 4.4 | Sample MR610 | 44 |
| 4.5 | Sample MR611 | 46 |
| 4.6 | Sample MR850 | 48 |
| 4.7 | Single beam saturation measurements | 50 |
| 4.8 | Discussion | 55 |
| Chapter 5 | Carrier lifetime measurements | 56 |
| 5.1 | Summary | 56 |
| 5.2 | Introduction | 56 |
| 5.3 | Experimental details | 58 |
| 5.4 | Results | 59 |
| 5.5 | Discussion | 63 |
| 5.5 | References | 63 |
| Chapter 6 | Screening, broadening and phase space filling | 65 |
| 6.1 | Summary | 65 |
| 6.2 | Introduction | 65 |
| 6.3 | Experimental details | 70 |
| 6.4 | Results | 70 |
| 6.5 | Data Analysis | 78 |

| | | |
|------------|--|-----|
| 6.5.1 | Exciton-exciton saturation | 81 |
| 6.6 | Discussion | 92 |
| 6.7 | Conclusions | 94 |
| Chapter 7 | Spin relaxation | 96 |
| 7.1 | Summary | 96 |
| 7.2 | Introduction | 96 |
| 7.3 | Spin relaxation in bulk semiconductors | 97 |
| 7.4 | Spin relaxation in quantum wells | 98 |
| 7.5 | Dynamical description of spin relaxation | 100 |
| 7.6 | Experimental details | 102 |
| 7.7 | Results | 103 |
| 7.8 | Discussion | 107 |
| 7.9 | Conclusion | 112 |
| 7.10 | References | 114 |
| Chapter 8 | Optical switching | 118 |
| 8.1 | Summary | 118 |
| 8.2 | Introduction | 118 |
| 8.3 | Spin dependent refractive index change | 120 |
| 8.4 | Experimental details | 122 |
| 8.5 | Results | 123 |
| 8.6 | Modelling of polarisation switching | 127 |
| 8.6.1 | Modelling results | 129 |
| 8.7 | Discussion | 136 |
| 8.8 | Conclusion | 137 |
| 8.9 | References | 138 |
| Chapter 9 | Conclusions | 141 |
| Chapter 10 | Publications | 144 |
| 10.1 | Journal publications | 144 |
| 10.2 | Conference publications | 144 |
| Chapter 11 | Acknowledgements | 146 |

Chapter 1 Introduction

The problem of the particle in a square well potential is familiar to any student of quantum mechanics. Anyone who has struggled to come to terms with the counter-intuitive nature of such problems must have wished for a practical experiment to help demonstrate the effects described by Schrodinger's theory of quantum mechanics. With the advent of epitaxial growth techniques such as molecular beam epitaxy (MBE) and metal-organic chemical vapour deposition (MOCVD) in the 1970's it finally became possible to grow a square well potential.

MBE and MOCVD allow the growth of semiconductor layers on an atomic scale, allowing semiconductor compositions to be grown with a previously unheard of accuracy. The precision of these techniques are such that it is possible to produce semiconductor layers with thickness of the order of the Bohr radius of an exciton. The simplest structure is a single quantum well, where a thin layer of semiconductor is confined between two layers of a different semiconductor, having a larger bandgap energy. Carriers confined in the smaller bandgap "well" material have properties that are more accurately described by a 2-dimensional system than a 3-dimensional one. Thus, the carriers are confined in a square well potential and, if the well is narrow enough (of the order of 10nm), quantum effects can be observed [1.1]. The confinement also causes an enhancement of the absorption due to the quasi-particle, known as an exciton, compared to the absorption observed in bulk material, making exciton absorption readily observable at room temperature in quantum wells [1.2].

If many quantum wells are grown together, then a multiple quantum well is formed. The advantage of the multiple quantum well over a single quantum well is most apparent in optical studies. Ideally a multiple quantum well will have the same properties as a single quantum well, but the optical density experienced by any light passing through the structure parallel to the growth direction will be increased by a factor n , where n is the number of quantum wells. It is the optical properties of such structures that will be investigated in this thesis.

The energy levels of a quantum well can be manipulated in many straightforward ways, such as varying the well width, doping level and voltage bias of a sample. This has led to the development of novel quantum well lasers [1.3], switches [1.4] and modulators [1.5]. Quantum wells also show a number of new properties when compared to bulk material. One such feature is the quantum confined Stark effect [1.6], which produces a red shift in the absorption edge when an electric field is applied across quantum well layers. The discovery of this effect has led to the realisation of electroabsorption devices such as the self electro-optic effect device (SEED) [1.7]. Such devices have led to many applications of quantum well structures in optical communications. Quantum well semiconductor lasers and detectors are routinely used in conjunction with low loss optical fibre to transmit data world-wide at ever increasing rates. Early work with quantum wells in optical communications made use of the GaAs / AlGaAs system, which operated at a wavelength of 850nm. This materials system was chosen because of the good lattice matching between GaAs and AlGaAs for a wide range of compositions. More recently work in optical communications has concentrated on wavelengths of 1.3 μ m or 1.55 μ m, where the fibre attenuation is at a minimum as shown in figure 1.1.

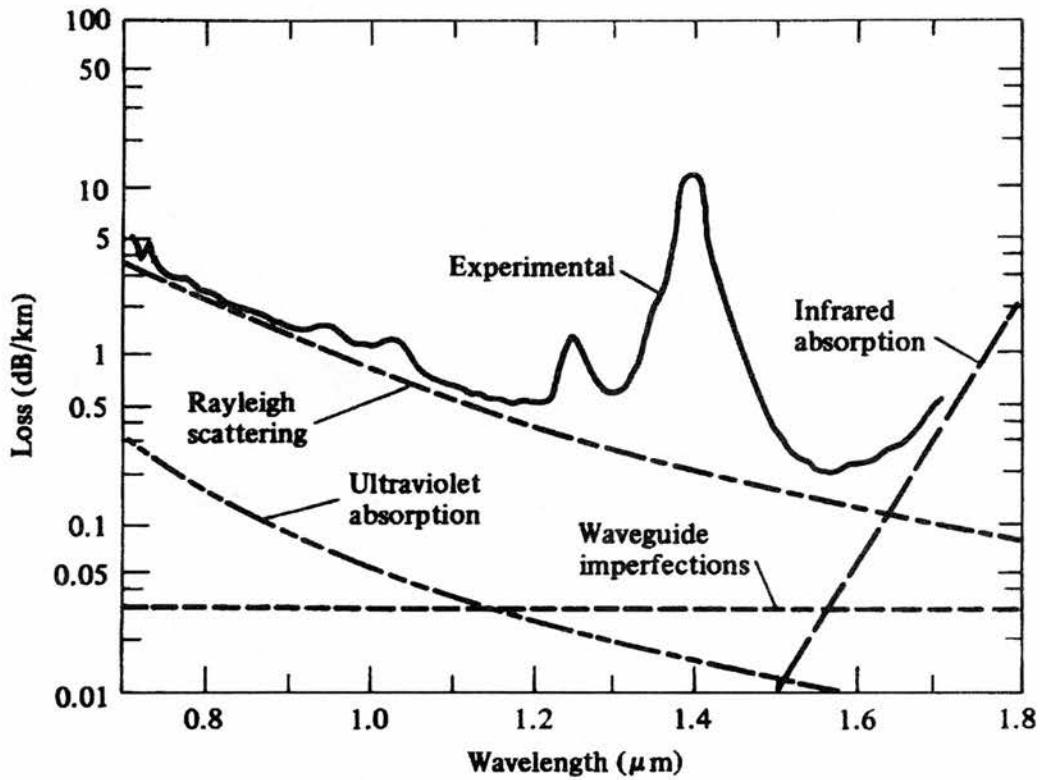


Figure 1.1 Attenuation in optical fibres as a function of wavelength. Low transmission losses occur at $1.3\mu\text{m}$ and $1.55\mu\text{m}$.

The development of ultrashort pulse lasers has allowed time-resolved pump-probe experiments to be carried out with time resolution of picoseconds and below. In a typical pump-probe experiment a sample is excited by a pump pulse and the transmission characteristics of a much less intense probe pulse, delayed in arrival time at the sample with respect to the pump pulse, are monitored as a function of the delay. Such experiments allow the dynamics of electronic processes within the quantum wells to be studied.

In this thesis a number of important parameters connected with quantum wells whose bandgap is commensurate with the preferred telecommunications transmission

wavelength around $1.5\mu\text{m}$ are optically measured. Chapter two introduces the basic physics of quantum wells and their optical properties. Chapters three and four describe the experimental techniques employed in this work and the samples under investigation, while chapter five describes the measurement of the carrier lifetime in these samples. In chapter six the mechanisms relating to exciton saturation are investigated. Chapters seven and eight explore the field of spin relaxation and its application in all-optical switching devices and chapter nine draws the results together in conclusion.

1.1 References

- 1.1 R. Dingle, W. Wiegmann and C.H. Henry "Quantum States of confined carriers in very Thin $\text{Al}_x\text{Ga}_{1-x}\text{As}-\text{GaAs}-\text{Al}_x\text{Ga}_{1-x}\text{As}$ heterostructures" *Phys. Rev. Letts.*, **33**, 827-830, (1974).
- 1.2 D.S. Chemla, D.A.B. Miller, P.W. Smith, A.C. Gossard and W. Wiegmann "Room temperature excitonic nonlinear absorption and refraction in $\text{GaAs}/\text{AlGaAs}$ multiple quantum well structures" *IEEE J. Quant. Electron.*, **QE-20**, 3, 265-272, (1984).
- 1.3 P.S. Zory "Quantum Well Lasers" Academic Press Inc., (1993).
- 1.4 P. LiKamWa, A. Miller, M. Ogawa and R.M. Park "All-optical bistable switching in an active InGaAs quantum-well waveguide" *IEEE Phot. Tech. Lett.*, **3**, 6, 507-509, (1991)
- 1.5 D.A.B. Miller "Quantum-well self-electro-optic effect devices" *Opt. Quant. Electrons.*, **22**, S61-S98, (1990).
- 1.6 D.A.B. Miller, D.S. Chemla, T.C. Damen, A.C. Gossard, W. Wiegmann, T.H. Wood and C.A. Burrus, "Band-edge electroabsorption in quantum well structures: the quantum-confined Stark effect", *Phys. Rev. Letts.*, **53**, 22, 2173-2176, (1984).
- 1.7 D.A.B. Miller, "Quantum-well self-electro-optic effect devices", *Opt. Quant. Electrons.*, **22**, s61-s98, (1990).

Chapter 2 Properties of quantum wells

2.1 Summary

In this chapter the optical properties of semiconductors and the effects of quantum confinement will be discussed. The increased effect of excitons on the absorption properties of quantum wells is also described. The relevance of optical selection rules and bandgap resonant non-linearities to the experiments described in future chapters are introduced.

2.2 Growth considerations

When growing semiconductors for use as optical devices, it is not only essential that the composition produces the bandgap energy required, it is also usual to ensure that the lattice constant remains the same throughout the whole structure, although strained layer structures have also been developed. Early crystal growers were fortunate that the ternary compound AlGaAs has the same lattice constant as GaAs over a wide range of compositions. However, no ternary compound has the right combination of bandgap energy and lattice constant for making devices for operation at $1.3\mu\text{m}$ or $1.55\mu\text{m}$. Figure 2.1 shows the nature of the problem by plotting bandgap energy against lattice constant for selected III-V compounds. Binary compounds occupy single points because their composition uniquely determines both bandgap energy and lattice constant. Lines connecting points represent ternary compounds, most of which span a range of lattice

constants and bandgaps. AlGaAs is a special case because both gallium and aluminium ions are about the same size, so moving along the AlGaAs line from GaAs to AlAs changes the lattice constant very little. There are no such equal sized pairs available for use at infra-red wavelengths, so it is necessary to use the quaternary compound InGaAsP, varying both the In/Ga and As/P ratios to make active layers lattice matched to InP with the desired bandgap energy.

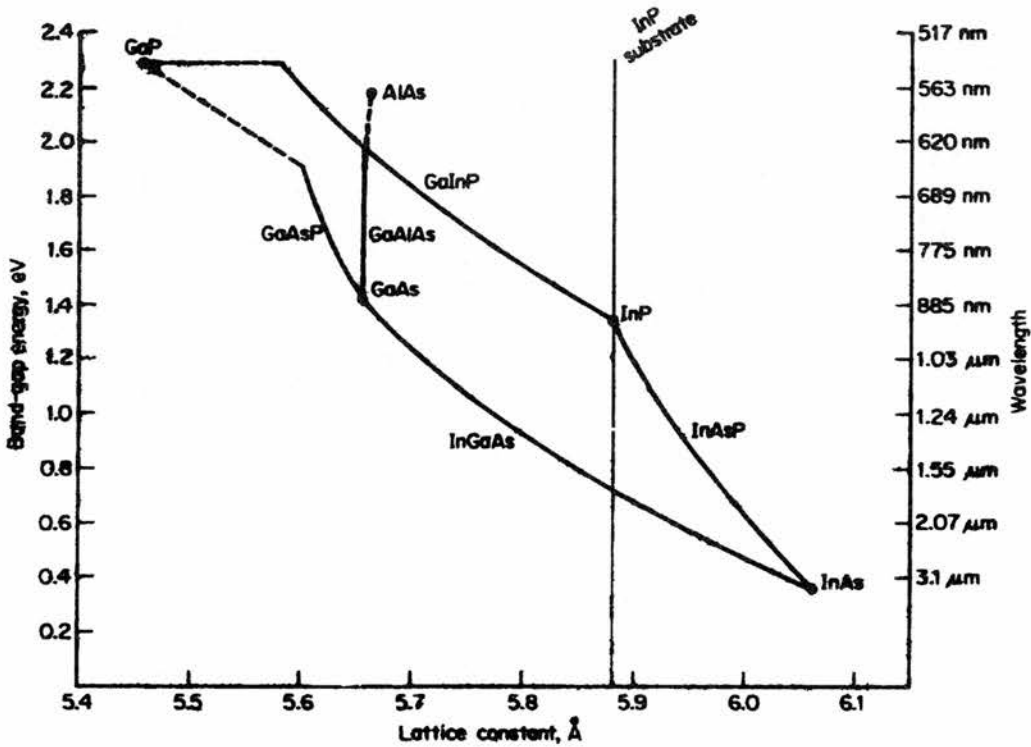


Figure 2.1 Lattice constants and bandgaps of semiconductors at room temperature.

The vertical line shows the quaternary compound InGaAsP.

2.3 Bulk III-V semiconductors

For the results presented in the following chapters the semiconductors of interest are $\text{In}_{1-x}\text{Ga}_x\text{As}_y\text{P}_{1-y}$ and $\text{In}_{1-x}\text{Ga}_x\text{As}$. Both are III-V semiconductors with a zinc blende

structure. The proportions of each constituent of the compounds, denoted by x and y are varied appropriately to achieve lattice matching to substrates, in this case InP. The band structure, when lattice matched to InP, is similar to that of InP or GaAs [2.1] with a direct gap at the Γ point in k -space. The electronic energy band structures of GaAs and InP are shown in figure 2.2. The region of interest is the Γ point at the centre of the Brillouin zone. The conduction band is two fold degenerate and the highest valence band is four fold degenerate at the zone centre. The degeneracy is partly lifted away from the zone centre where the band splits into a light and a heavy band, each being two fold degenerate. There is also a lower valence band separated from the highest valence band, due to the effects of spin-orbit coupling, by $0.011+0.31y-0.09y^2$ eV. The bandgap is the difference in energy between the lowest conduction and highest valence bands at the zone centre.

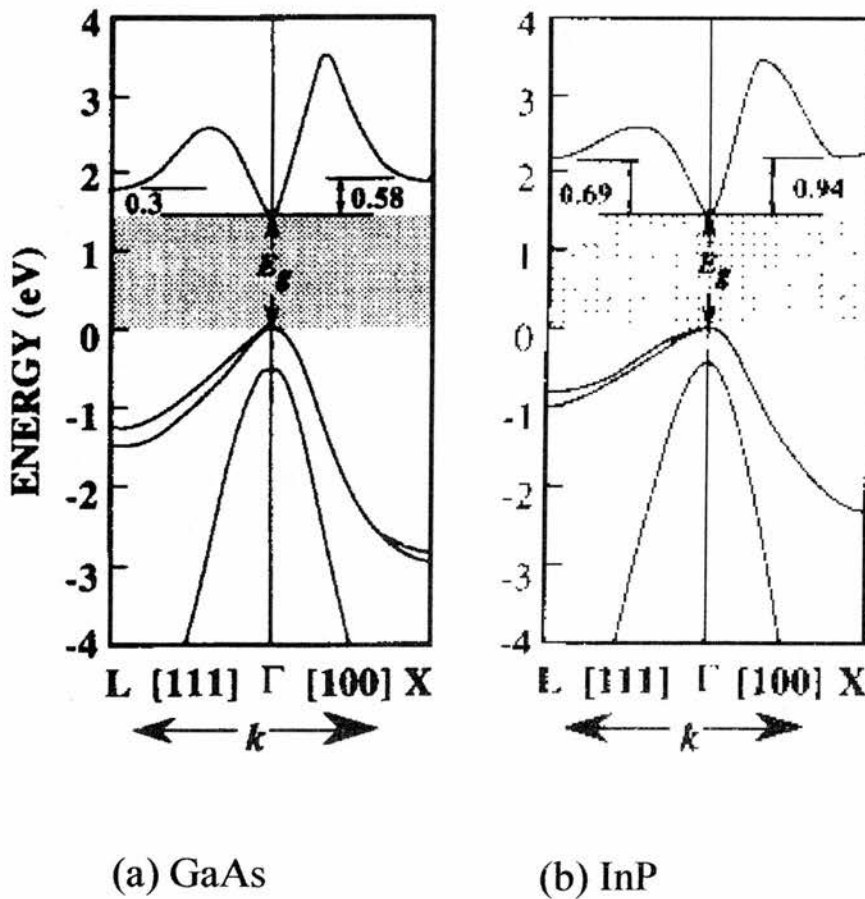


Figure 2.2 Bandstructure of, a, GaAs, $E_g=1.43$ eV at 300 K and b, InP, $E_g=1.34$ eV at 300 K, around the Γ point.

2.4 Multiple quantum wells

Multiple quantum wells (MQW's) can be one of either two different types. In type I quantum wells the electrons and holes are both confined in the same semiconductor material. In type II quantum wells the electrons and holes reside in different semiconductor materials. These two situations are shown in figure 2.3.

InGaAs(P)/InGaAsP multiple quantum wells are type I structures. The potential wells for both the electrons and holes are either $\text{In}_{0.73}\text{Ga}_{0.27}\text{As}_{0.58}\text{P}_{0.42}$ for operation at 1.3 μm or $\text{In}_{0.58}\text{Ga}_{0.48}\text{As}_{0.9}\text{P}_{0.1}$ for operation at 1.55 μm and the InGaAsP barriers are grown to have a larger band-gap. $\text{In}_{1-x}\text{Ga}_x\text{As}_y(\text{P}_{1-y})$ has a direct bandgap over the full range of lattice matched compounds and the size of the band gap is controlled with the mole fraction y , using the following expression [2.2].

$$E_g = 1.35 - 0.72y + 0.12y^2 \quad (2.1)$$

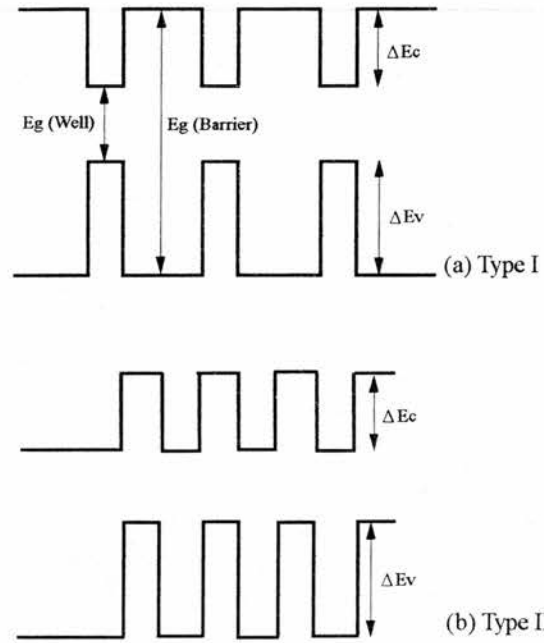


Figure 2.3 Band structure for (a) type I and (b) type II multiple quantum wells.

The mole fraction x is determined using the following relation to ensure lattice matching to InP substrates.

$$x = \frac{0.4526y}{(1 - 0.031)y} \quad (2.2)$$

The difference in the band-gap of the well and barrier material is denoted ΔE_g . The distribution of ΔE_g between the conduction band and valence band defines the depth of the respective potential wells. The relative size of each quantum well is denoted the band offset ratio $a:b$, where the depth of the conduction band well $\Delta E_c = a\Delta E_g$ and the depth of the valence band well $\Delta E_v = b\Delta E_g$. Martin et al [2.3] evaluated the offset ratio for unstrained InGaAsP/InGaAsP as 40:60.

2.5 Quantisation of energy levels

The main effect that confinement has on the properties of electrons and holes is to quantise the energy levels available to them. The simplest potential well to treat theoretically is a one dimensional well of width L with zero potential in the confined region and infinitely high potential outside the region. The energy levels and wavefunctions for the system are given by the solution of the Schrödinger equation,

$$H\psi_n(z) = E_n\psi_n(z) \quad (2.3)$$

$$H = \left(\frac{-\hbar^2}{2m^*} \right) \frac{\delta^2}{\delta z^2} + V_c(z) \quad (2.4)$$

which has the well-known solution for an infinite potential well,

$$E_n = \frac{\hbar^2}{2m^*} \left(\frac{n\pi}{L} \right)^2 \quad (2.5)$$

$$\psi_n(z) = \sqrt{\frac{2}{L}} \sin\left(\frac{n\pi z}{L}\right) \quad (2.6)$$

Real semiconductor quantum wells have finite barriers, however, and are said to be finite potential wells. Electrons are unaffected by quantum confinement in the plane of the layers, and hence are free to move. The band structure for this plane (the x,y plane) is the same as for bulk material and can be approximated by a parabola near $k=0$.

$$E_{xy} = \frac{\hbar^2(k_x^2 + k_y^2)}{2m_a^*} \quad (2.7)$$

Energy levels for motion perpendicular to the layers are quantised. For a conduction band potential well of height V_0 the solution of the Schrödinger equation is found by applying continuity conditions to the wavefunction and its first derivative at the well boundaries. This leads to the transcendental equations,

$$\frac{k}{m_a^*} \tan\left(\frac{kL}{2}\right) = \frac{K}{m_b^*} \quad (2.8)$$

$$\frac{k}{m_a^*} \cot\left(\frac{kL}{2}\right) = -\frac{K}{m_b^*} \quad (2.9)$$

where m_a^* and m_b^* are the electron effective masses in the well and barrier regions respectively, and

$$k^2 = \frac{2m_a^*}{\hbar^2} (E_n - V_0) \quad (2.10)$$

$$K^2 = \frac{2m_b^*}{\hbar^2} E_n \quad (2.11)$$

The transcendental equations cannot be solved analytically, so a numerical or graphical method is usually used.

The hole energies for motion in the growth direction are also quantised and can be found in an identical way to that described above. The dispersion relation in the x,y plane is more complicated for holes, however, due to the degeneracy of the valence bands at $k=0$, and the non-parabolicity of the hole bands. It is usual to treat the holes by solving the band structure for bulk material, treating the potential well as a perturbation. The most successful way of describing the valence band structure near $k=0$ is the Luttinger Hamiltonian [2.4]. This describes the valence band curvature in terms of the hole effective masses, expressed in terms of the Luttinger parameters γ_1 , γ_2 and γ_3 .

In bulk III-V compounds the valence band consists of two $J=3/2$ upper bands, which are degenerate at $k=0$, and a $J=1/2$ spin-orbit split-off band. Quantum wells are usually grown with the normal to the layers, z , parallel to the (001) crystallographic direction. This results in the two $J=3/2$ valence bands having different effective masses of

$(\gamma_1 \pm 2\gamma_2)/m_0$. Hence a consequence of quantum confinement is the lifting of the valence band degeneracy at $k=0$ due to the mass dependence in the quantisation energy.

Unlike electrons in the conduction band, the dispersion relations for holes in the valence band, parallel to the layers, are affected by quantum confinement. The dispersion relations for the two $J=3/2$ valence bands perpendicular to the growth direction become,

$$E = \frac{\hbar^2 k_{\perp}^2}{2 \left(m_h / [\gamma_1 + \gamma_2] \right)} \quad (2.12)$$

for $J_z = \pm 3/2\hbar$ and

$$E = \frac{\hbar^2 k_{\perp}^2}{2 \left(m_h / [\gamma_1 - \gamma_2] \right)} \quad (2.13)$$

for $J_z = \pm 1/2\hbar$. The $J_z = \pm 3/2\hbar$ band is the heavy hole band in the bulk material. However, in the x,y plane of the quantum well it now has a light effective mass of $m_h / (\gamma_1 + \gamma_2)$ whereas the $J_z = \pm 1/2\hbar$ band, the light hole band in bulk material has the heavier effective mass of $m_h / (\gamma_1 - \gamma_2)$ once confined. In bulk material the heavy hole band lies higher than the light hole band, suggesting the bands will cross around $k = \pi\sqrt{2}/L_z$ in confined material, which is unphysical. Inclusion of higher order k.p perturbation terms or the potential discontinuities in the full Luttinger Hamiltonian eliminates this problem by introducing anti-crossing behaviour, demonstrated in figure 2.4.

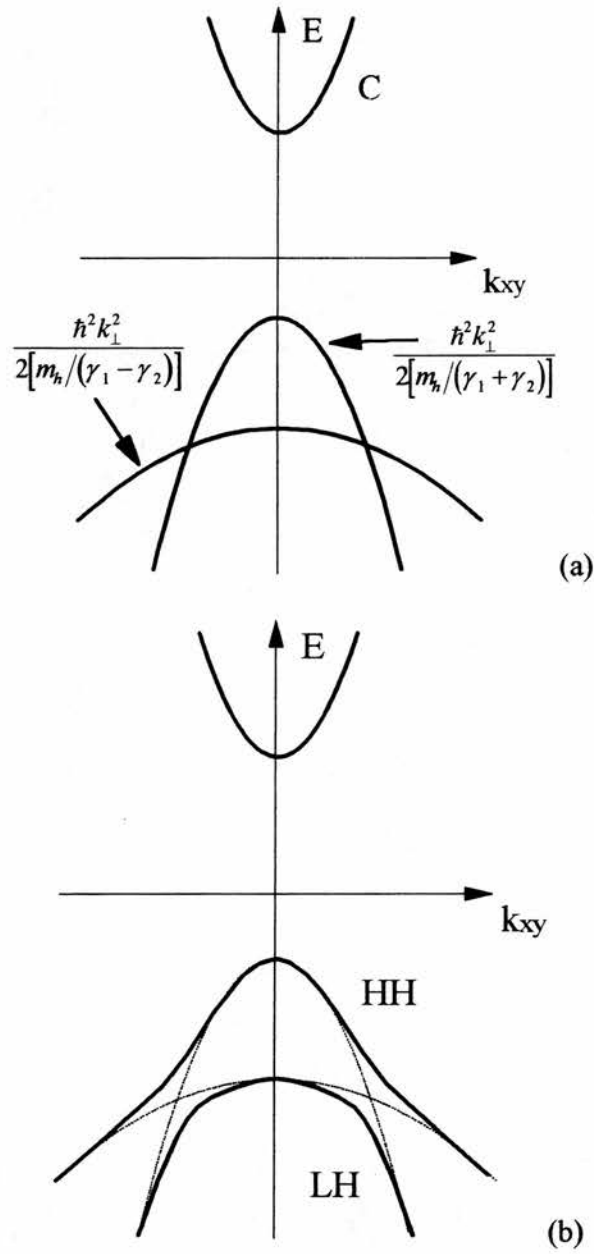


Figure 2.4 Representation of (a) the band crossing predicted by the solutions to the Luttinger Hamiltonian in a quantum well and (b) the anticrossing produced by higher order perturbation terms.

2.6 Density of states

Optical absorption is governed by the density of states. In a bulk semiconductor, assuming parabolic bands, the density of states is given by the following

$$D_{3D}(E) = \frac{1}{2\pi^2} \left(\frac{2m^*}{\hbar^2} \right)^{3/2} E^{1/2} \quad (2.14)$$

where E is the energy and m^* is the carrier effective mass. In a quantum well the energy levels are quantised and the density of states is modified as follows

$$D_{2D} = \frac{nm^*}{\pi\hbar^2} \frac{1}{a} \quad (2.15)$$

where n is the quantum number $n = 1, 2, 3, \dots$. The 2D density of states therefore has a “step-like” appearance and remains finite for low energies. Note also that the absorption edge is shifted to a higher energy in 2D compared to bulk. The 2D and 3D density of states functions are shown graphically in figure 2.5. The density of states function is proportional to the optical absorption in a semiconductor and a typical room temperature absorption spectrum for an InGaAs(P) multiple quantum well is shown in figure 2.6. The “step-like” nature of the optical absorption can be clearly seen along with sharp resonance features, which correspond to excitons.

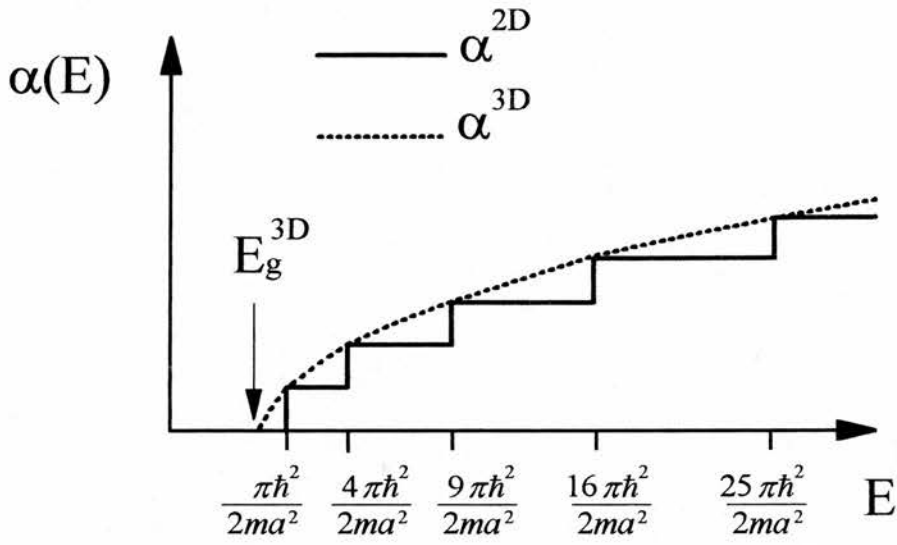


Figure 2.5 Comparison of the 2D and 3D density of states functions.

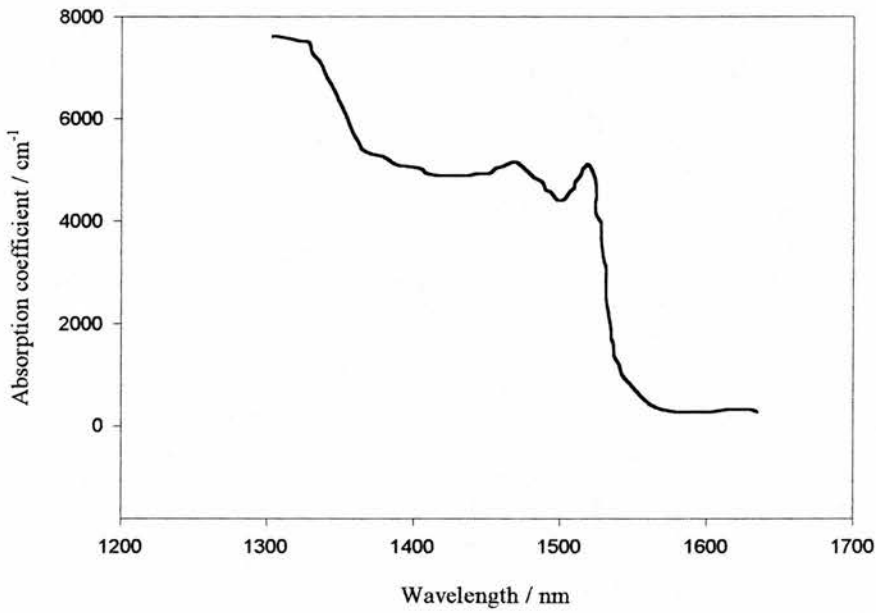


Figure 2.6 The linear absorption spectrum of an $\text{In}_{0.53}\text{Ga}_{0.47}\text{As}_{0.95}\text{P}_{0.05}$ / $\text{In}_{0.53}\text{Ga}_{0.47}\text{As}_{0.34}\text{P}_{0.66}$ quantum well.

2.7 Excitons

The Coulomb interaction between excited electrons and their associated holes can result in the formation of bound electron-hole pairs known as excitons. Excitons are analogous to hydrogen atoms in that the electron can be considered to orbit the hole, due to the greater mass of the hole, and the quasi-particle is electrically neutral. There are two distinct types of exciton, depending on the properties of the material in which they are created. Frenkel excitons are highly localised and tightly bound to impurities or defects. They have a small orbital and are created in ionic solids and wide-gap semiconductors. The second type of exciton is known as a Wannier exciton. Wannier excitons are weakly bound and are created when the exciton Bohr radius is large compared to the length of the crystal unit cell. This condition is met in III-V semiconductors such as InGaAs(P) where the excitons have a Bohr radius of several hundred angstroms, compared to a lattice constant for InP of 5.85 angstroms. These excitons are of interest in this study.

In bulk material, the exciton is three dimensional, but as the quantum confinement becomes of the order of the exciton Bohr radius the exciton tends towards two dimensions. The 3D exciton energy levels and wave functions can be found using the same method used for the hydrogen atom, being given by

$$E_n^{3D} = E_n - \frac{R_0}{n^2} \quad (2.16)$$

$$\psi_{1s}^{3D} = \frac{1}{\sqrt{\pi a_0^3}} \exp\left(-\frac{r}{a_0}\right) \quad (2.17)$$

where the 3D Rydberg and Bohr radius are given by

$$R_0 = \frac{e^4 \mu}{2\epsilon^2 \hbar^2} \quad (2.18)$$

and

$$a_0 = \frac{\epsilon \hbar^2}{\mu e^2} \quad (2.19)$$

respectively and ϵ is the dielectric constant and μ is the effective mass. In an ideal 2D system the energy levels and wavefunctions of the excitons are modified, and given by

$$E_n^{2D} = E_n - \frac{R_0}{\left(n - \frac{1}{2}\right)^2} \quad (2.20)$$

$$\psi_{1s}^{2D} = \sqrt{\frac{2}{\pi}} \frac{2}{a_0} \exp\left(-\frac{2r}{a_0}\right) \quad (2.21)$$

It can be seen that in two dimensions the Bohr radius of the wavefunction is half that of the 3D value causing a fourfold increase in the ground state binding energy. A real quantum well is not an ideal 2D system, however, since the finite height of the barriers allows penetration of the wavefunctions of the excitons into the barriers. A real system can be described as being somewhere between 2D and 3D and is usually referred to as quasi-2D. Consequently, the actual increase in the ground state binding energy is somewhat less than that for the ideal 2D case.

2.8 Optical excitation

In semiconductors, illumination with a photon of suitable energy results in the excitation of an electron into the conduction band and the creation of a hole in the valence band. The selection rules governing these transitions are obtained by calculating the dipole matrix elements for the relevant interband transitions. For a bulk semiconductor, the selection rules and transition probabilities are shown in figure 2.7.

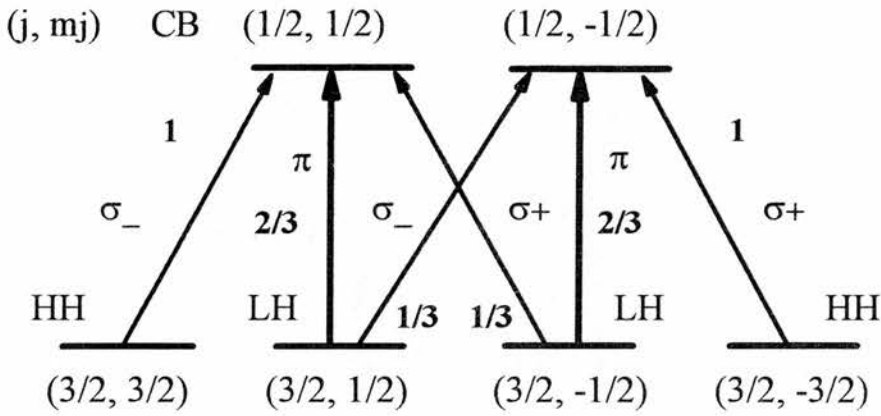


Figure 2.7 Selection rules in bulk InGaAsP.

In a quantum well the lifting of the degeneracy between the light and heavy holes at band centre modifies these transitions as shown in figure 2.8. The allowed transitions can be summarised as follows:

$$\Delta J = \pm 1$$

$$\Delta J_z = -(+) \hbar \quad \text{for right (left) hand circularly polarised light, labelled } \sigma^- (\sigma^+).$$

$$\Delta J_z = 0 \quad \text{for linear polarised light, labelled } \pi.$$

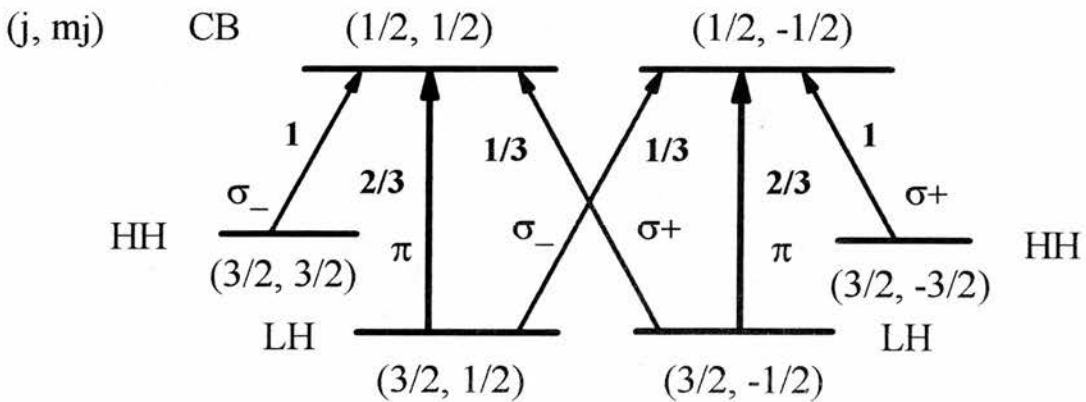


Figure 2.8 Selection rules in InGaAsP multiple quantum wells.

When a bulk semiconductor is excited with left or right circularly polarised light, populations of both $J_z = +\frac{1}{2}\hbar$ and $J_z = -\frac{1}{2}\hbar$ electrons are generated, along with correspondingly polarised holes. The electrons are generated in the ratio 3:1 which limits the polarisation of the electrons to only 50%. The polarisation of the electrons can be defined as

$$P = \frac{N_{\uparrow} - N_{\downarrow}}{N_{\uparrow} + N_{\downarrow}} \quad (2.22)$$

where $N_{\uparrow(\downarrow)}$ is the number of electrons polarised with spin up (down).

In a quantum well however, due to the lifting of the degeneracy between the light and heavy hole bands, it is possible to generate electrons with 100% spin polarisation using circularly polarised light resonant with the heavy hole (or associated exciton) transition. The effect of light on the spin angular momentum of carriers is known as optical orientation and will be discussed further in chapter 7.

2.9 Resonant optical nonlinearities

The optical excitation of carriers in a semiconductor can produce a number of non-linear effects namely Coulomb screening, band filling, phase space filling, bandgap renormalisation and lineshape broadening. These effects will now be discussed.

2.9.1 Coulomb screening

Generation of an electron-hole plasma can lead to the screening of the Coulomb potential between charges. After excitation, carriers occupy states in the valence and conduction bands of a semiconductor. These carriers can screen the Coulomb interaction

between carriers in the same band and between carriers in other bands. Screening is the term used to denote a decrease in the Coulomb potential of a charge in the presence of other charges. If a plasma of electrons is considered, the addition of a test charge results in a redistribution of the plasma due to the repulsive Coulomb interaction. This reduces the overall energy of the system, decreasing the effective energy of the test charge and reducing the attractive force between the electron and hole that form an exciton. Coulomb screening therefore has the effect of reducing the exciton binding energy. When a large number of electron-hole pairs are created the Coulomb screening becomes sufficiently large to cause the excitons to ionise. This means that the excitons no longer exist as a bound state and the exciton absorption feature is said to be saturated. A secondary consequence of the Coulomb screening is a red shift of the band edge due to the reduction of the single particle energies, otherwise known as bandgap renormalisation.

2.9.2 *Band and phase space filling*

Electrons and holes are fermions and as such are governed by the Pauli exclusion principle. Therefore, for each k-state that exists in a semiconductor there are two possible states available corresponding to either a spin-up or a spin-down carrier. As a filled state is no longer available as a final state in a band to band absorption process, the corresponding transition is bleached. Due to the principle of energy minimisation, carriers in quasi-equilibrium occupy the available states from the bottom of the band so that the energetically lowest states are occupied first, with the thermal equilibrium probability of occupancy for a state of energy E given by

$$f(E) = \frac{1}{1 + \exp\left(\frac{E - \phi}{kT}\right)} \quad (2.23)$$

where ϕ is the 50 % occupancy level and T is the temperature.

This results in the filling of states near the bottom of the conduction band and near the top of the valence band. Band filling is a consequence of the filling of the lowest energy states. For a transition to occur the corresponding valence band state must be filled by an electron and the conduction band state must be empty. If this is not the case then further transitions involving these states are not available and the absorption is bleached, resulting in a shift of the absorption edge to higher energies.

The presence of excited electrons and holes also prevents the formation of excitons derived from the states that they occupy. This mechanism is called phase space filling. Therefore, it is common to refer to band filling when discussing electrons and holes and to phase space filling when referring to excitons.

2.9.3 Lineshape broadening

At low temperature, the linewidth of an exciton can be attributed to broadening caused by interaction impurities and acoustic phonons. These mechanisms result in homogeneous broadening only. In a quantum well, scattering caused by fluctuations in well width [2.5] or alloy concentration results in either homogeneous or inhomogeneous broadening depending on the magnitude of the fluctuations. Irregularities of radius greater than the exciton Bohr radius cause inhomogeneous broadening whereas irregularities of radius less than the exciton Bohr radius cause homogeneous broadening.

As the temperature is increased, thermal broadening occurs due to the increased probability of collision with an LO-phonon. The contribution to the exciton linewidth by thermal broadening can be written as

$$\Gamma(T) = \Gamma(0) + \frac{\Gamma_{ph}}{\left[\exp\left(\frac{-\hbar\Omega_{LO}}{kT}\right) - 1 \right]} \quad (2.24)$$

where $\Gamma(0)$ is the temperature independent linewidth, Γ_{ph} is a parameter describing the effect of the LO-phonons, $\hbar\Omega_{LO}$ is the phonon energy and T is the temperature [2.6]. As the LO-phonon energy is large compared to the exciton binding energy, any collision results in complete ionisation of the exciton.

The homogeneous exciton linewidth is also influenced by the effect of collisions with other excitons or free carriers. At room temperature collisional broadening is mainly caused by interactions with free carriers, hence the presence of optically generated free carriers increases the exciton linewidth. The density dependence of the linewidth at low densities is given by

$$\Gamma(N) = \Gamma(0) + \gamma\alpha_B^2 E_B N \quad (2.25)$$

where $\Gamma(0)$ is the density independent linewidth, γ is a parameter describing the efficiency of the exciton-free carrier interaction, α_B is the exciton Bohr radius, E_B is the exciton binding energy and N is the density of the free carriers [2.7].

2.10 References

- 2.1 G. P. Agrawal, N. K. Dutta, "Semiconductor Lasers", Van Nostrand Reinhold, (1993)
- 2.2 N. K. Dutta, "Calculated absorption, emission and gain in $\text{In}_{0.72}\text{Ga}_{0.28}\text{As}_{0.6}\text{P}_{0.4}$ ", J. Appl. Phys., **51**, 12, 6095-6100, (1980).
- 2.3 R. W. Martin, S. L. Wong, R. J. Nicholas, A. Smith, M. A. Gibbon, E. J. Thrush, J. P. Stagg, "Band offsets in strained InGaAsP/InGaAsP quantum well optical modulator structures", Journal De Physique IV, **C5**, 3, 327-330, (1993).
- 2.4 J. M. Luttinger, "Quantum theory of cyclotron resonance in semiconductors: general theory", Phys. Rev., **102**, 1030-1041, (1956).
- 2.5 C. Weisbuch, R. Dingle, A. C. Gossard, W. Wiegmann, "Optical characterisation of interface disorder in GaAs-Ga_{1-x}Al_xAs multi-quantum well structures", Solid. State. Comms., **38**, 709-712, (1981).
- 2.6 D. S. Chemla, D. A. B. Miller, "Room temperature excitonic non-linear optical effects in semiconductor quantum well structures", J. Opt. Soc. Am. B, **2**, 7, 1155-1173, (1985).
- 2.7 A. Honold, L. Schultheis, J. Kuhl, C. W. Tu, "Collisional broadening of two dimensional excitons in a GaAs single quantum well", Phys. Rev. B, **40**, 9, 6442-6445, (1989).

Chapter 3 Experimental techniques

3.1 Summary

In the following chapter the basic experimental techniques used to study the optical properties of multiple quantum wells are introduced.

3.2 Introduction

In a multiple quantum well, or any semiconductor, free electrons and holes can be created via the absorption of radiation of photon energy above the bandgap energy. The radiation can take the form of a standard white light source or of coherent radiation emitted from a laser. Experiments of interest are ones that allow measurement of linear absorption spectra, providing important information on the band structure and position of exciton resonances, and those that allow the dynamical properties of excited carriers to be monitored. In the following sections the experimental techniques used to make such measurements will be discussed.

3.3 Linear absorption

The standard technique for determining the linear absorption of a semiconductor sample involves measuring the absorption of light passing through the semiconductor sample whilst scanning the wavelength of the incident light. The light source can be either

a white light source, where wavelength selection is made via a monochromator or a tuneable laser where the laser wavelength is scanned. Care must be taken to ensure that the incident light induces no saturation, as this clearly will not allow the measurement of linear absorption. It is also important that the data is calibrated for any spectral variation in the power of the light source as the wavelength is scanned.

The experimental arrangement for the measurement of the linear absorption using a white light source is shown in figure 3.1.

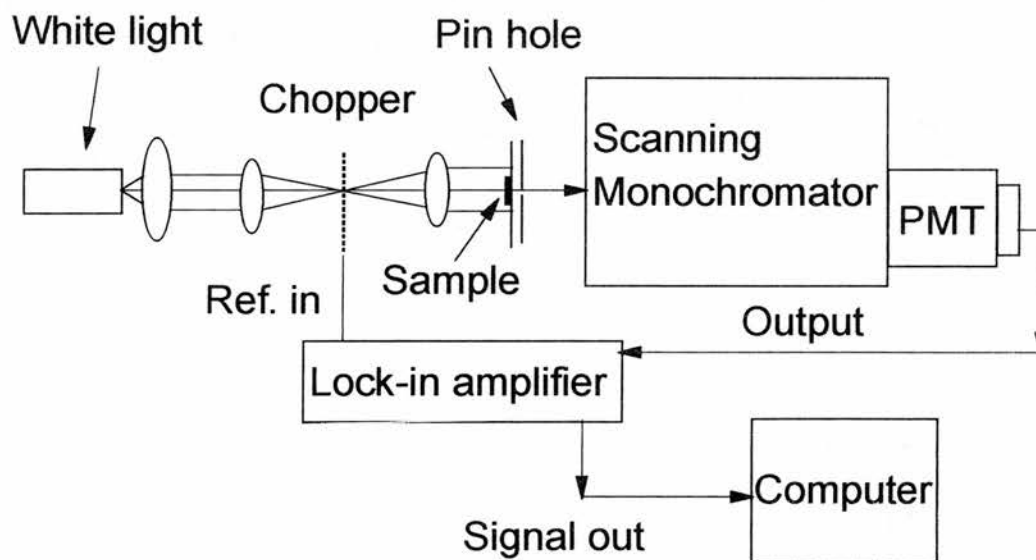


Figure 3.1 Experimental set-up for the measurement of the linear absorption using a white light source.

The light from the source is passed through the blades of a chopper and collimated before being made incident on the sample, which is positioned directly in front of an aperture. The chopper is used to allow phase sensitive detection via the lock-in amplifier. A scanning monochromator in conjunction with a photomultiplier and lock-in amplifier are

used to measure the absorption of the sample as the wavelength is scanned. Data is recorded at incremental steps of the wavelength scan by the computer. Once the experiment is completed the data is corrected for the spectral response of the light source using a control run, carried out with no sample present.

Measurements of the linear absorption can provide no detail on the temporal dynamics of processes that occur within quantum wells. For such measurements the technique known as degenerate time-resolved pump-probe is used.

3.4 Degenerate time-resolved pump-probe

The most commonly used technique to study the time dependent optical properties of quantum wells is that of degenerate time-resolved pump-probe. This technique measures the change in the transmission of a sample as the relative time delay between the arrival of a strong pump pulse and a weaker probe pulse on the sample is varied. By detecting the probe transmission as the delay time is scanned it is possible to interpret the signals in terms of electron dynamics and time resolve a number of mechanisms. The sources used in this work are a coupled cavity mode-locked $\text{KCl:Tl}^0(1)$ colour-centre laser and a Titanium:sapphire pumped optical parametric oscillator (OPO) based on periodically poled lithium niobate (PPLN).

3.4.1 Coupled cavity mode-locked $\text{KCl:Tl}^0(1)$ colour-centre laser

The mode-locked laser used in the following experiments is a home built $\text{KCl:Tl}^0(1)$ colour-centre laser. Colour-centres in $\text{KCl:Tl}^0(1)$ crystals are associated with neutral thallium atoms perturbed by adjacent anion vacancies. Colour-centre gain media

are homogeneously broadened and through their large gain bandwidth, can be mode-locked to produce pulses of sub-picosecond duration [3.1]

A $\text{KCl:Tl}^0(1)$ laser was used to generate pulses of the order of either 500 fs or 100 fs duration, which were used in the experiments described in this thesis. The absorption band of the colour-centre in $\text{KCl:Tl}^0(1)$ is centred at $1.06 \mu\text{m}$ and the laser is tuneable from $1.4 - 1.63 \mu\text{m}$ [3.2]. The laser was pumped optically using 2 W of $1.06 \mu\text{m}$ light from a Nd:YAG laser and typically yielded an output power of around 10 mW.

To obtain laser action from $\text{KCl:Tl}^0(1)$ crystals it is necessary to maintain them at cryogenic temperatures. The laser cryostat used to keep the crystals at low temperatures was developed at St. Andrews University. The resonator cavity configuration used was based on one originally used for dye lasers and is shown in figure 3.2. The length of the cavity was matched to the length of the cavity of the Nd:YAG pump laser (183 cm).

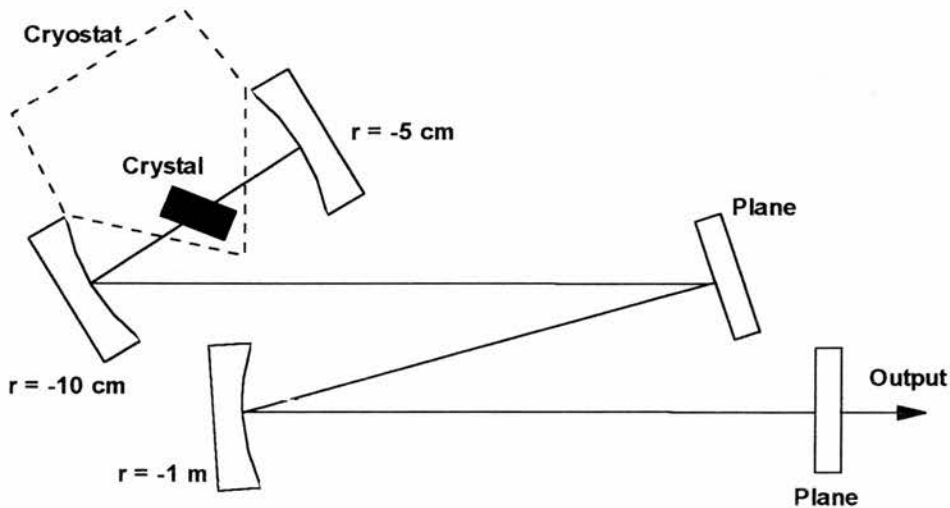


Figure 3.2 Schematic of the resonator configuration used for the $\text{KCl:Tl}^0(1)$ colour-centre laser.

To produce the mode-locked pulses a technique known as coupled-cavity mode-locking was used. With this technique, the laser cavity was constructed as an interferometer and a non-linear element introduced into one of the arms of the interferometer [3.2]. In the experiments described in this thesis, a Fabry-Perot configuration was used, as shown in figure 3.3.

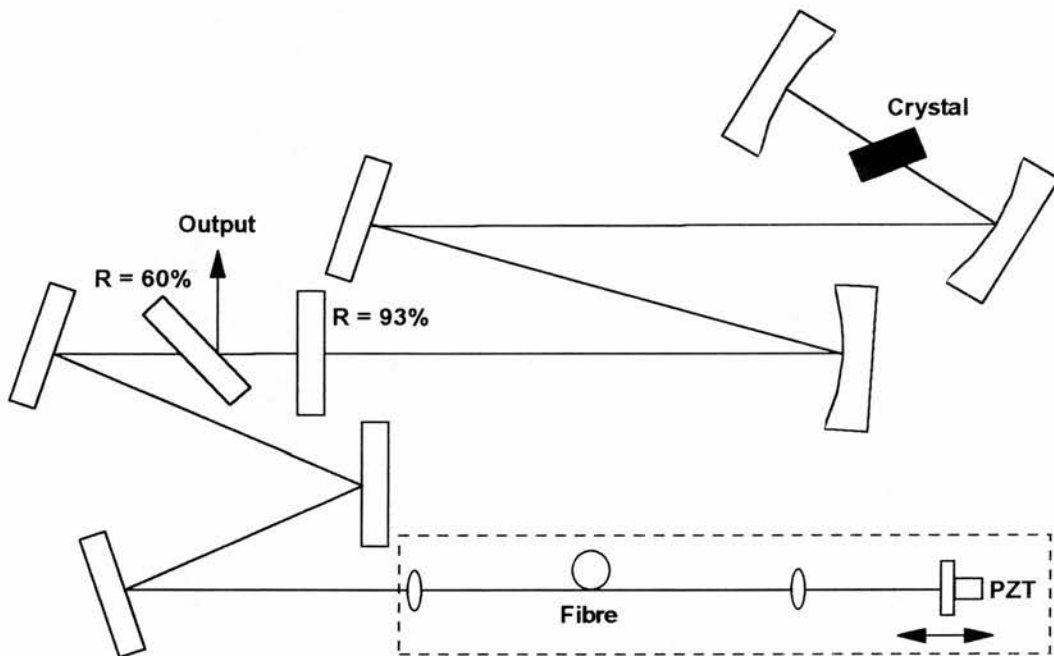


Figure 3.3 Schematic of the $KCl:Ti^3(1)$ colour-centre laser in a non-linear Fabry-Perot configuration.

An intense pulse propagating through the non-linear element included in the non-linear arm of the interferometer experiences a phase shift proportional to the intensity across its profile. By arranging a suitable phase difference between the arms of the interferometer it is possible to add pulses in the main cavity to pulses returning from the non-linear arm such that there is constructive interference in the centre of the pulses and

destructive interference in the wings. This has the effect of reducing the duration of the pulses in the main cavity. The non-linear element used for this work was an erbium doped optical fibre. The length of the fibre is matched to provide sufficient non-linearity for the pulse duration required, longer pulses requiring a longer length of fibre due to their smaller peak power. Modelocked pulses in the range 150 fs to 650 fs could be achieved.

3.4.2 *Titanium:sapphire pumped PPLN OPO*

Optical parametric oscillators (OPOs) have been developed considerably over the past decade in an attempt to extend the tuning ranges available from conventional pump sources. An optical parametric oscillator consists of a non-linear crystal placed within a resonator in a similar manner to a conventional laser. A high power wave of frequency ω_p is passed through the non-linear material resulting in the generation of two output waves at frequencies ω_s and ω_i , given by

$$\omega_p = \omega_s + \omega_i \quad [3.1]$$

The high power wave ω_p is conventionally known as the pump, with the higher frequency generated wave known as the signal and the lower frequency field known as the idler. Gain will be experienced at the frequencies ω_s and ω_i through a difference frequency mixing process, provided that the phase-matching condition shown below is satisfied,

$$k_p = k_s + k_i \quad (3.2)$$

where k represents the wavevector in the non-linear material.

When both the above conditions are satisfied, an input pump frequency will result in the generation of a pair of signal and idler frequencies. The magnitude of these frequencies depends on the value of the pump frequency and the dispersion of the non-

linear medium. The signal and idler frequencies can be changed by a number of methods, all of which involve the variation of the refractive indices of the medium in the direction of propagation. Changing the pump frequency results in a change in the generated signal and idler values due to the wavelength dependence of the refractive indices. When a fixed wavelength pump source is used then tuning can be achieved by either varying the non-linear crystal angle with respect to the pump beam or by changing the crystal temperature.

The OPO was pumped by a Spectra Physics Tsunami self mode-locked Titanium:sapphire laser, pumped by a Spectra Physics 2060 Beamlok argon ion laser. The Tsunami produced 2 ps pulses, which could be tuned over the range 770-920 nm with the current mirror set. The laser operated in pulsed mode with a repetition frequency of 82 MHz.

The non-linear crystal used in the OPO was PPLN [3.3]. Lithium Niobate is attractive for use in OPOs because of its large transparency range, from 0.35 to >4 μm . Where non-critical phase matching geometries are used there is no walk off, but in normal Lithium Niobate the coherence length limits the maximum wavelength conversion that can be achieved. Periodic poling flips the optical axis of the crystal periodically, with a period determined by the coherence length, allowing the non-linear interaction to occur over several coherence lengths and reducing the threshold.

The OPO was singly resonant, resonating the signal beam, and the cavity configuration is shown in figure 3.4.

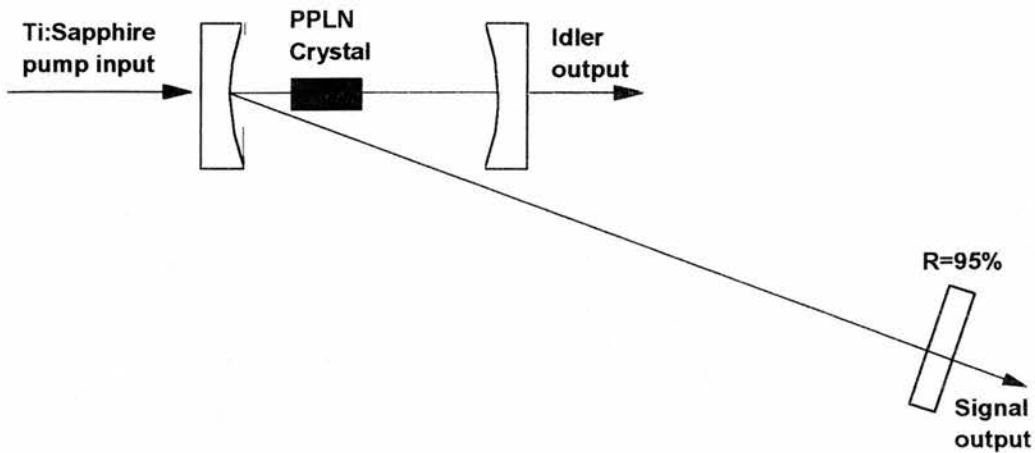


Figure 3.4 PPLN OPO cavity configuration.

The two curved mirrors were coated to be anti-reflective at the pump wavelength and highly reflective at the signal wavelengths. The cavity length was matched to the Ti:sapphire cavity length, to synchronously pump the OPO. The signal wavelength was temperature tuned from 120 to 170 °C and produced 2 ps pulses tuneable from 1.3 to 1.6 μm with an output power of around 100 mW, when pumped at 840 nm.

For specific temperature settings the output wavelength varied when the length of the cavity was adjusted across the synchronous range of the OPO. Longer cavity lengths resulted in a shift in the signal wavelength to shorter wavelengths. This was due to slower group velocities being associated with longer wavelengths in the anomalous dispersion region and this method of altering the signal wavelength has proved to be very useful in fine tuning the OPO output.

3.4.3 Diagnostics

Scanning-autocorrelators were used to monitor the pulses produced from the modelocked sources. The autocorrelators utilised second harmonic generation from type I

phase matching of two input beams in a BBO crystal. An incident beam was split into two beams of equal intensity, reflecting one from a static retroreflector and reflecting the other from a retroreflector mounted on a loudspeaker before recombining the two beams and passing them through a frequency doubling crystal. Second harmonic light generated in the doubling crystal by the incident beams was detected with a photo-multiplier tube. The arrangement of the autocorrelator can be seen in figure 3.5. The loudspeaker was modulated with a rounded sawtooth waveform, causing a variation of the temporal overlap of the two beams of pulses. When the pulses were temporally overlapped in the doubling crystal a signal was detected with the photo-multiplier tube with a pulse to background ratio of 3:1.

The width of the detected second harmonic signal gives the laser pulse width, assuming the pulse was a given shape (Gaussian for actively mode-locked lasers and sech^2 for passively mode-locked lasers). The measured autocorrelation pulse width must be divided by an appropriate constant to give the actual pulse width. An example of intensity autocorrelations of a 650 fs pulse from the KCL:Ti⁰(1) colour-centre laser and of a 2 ps pulse from the PPLN OPO are shown in figure 3.6.

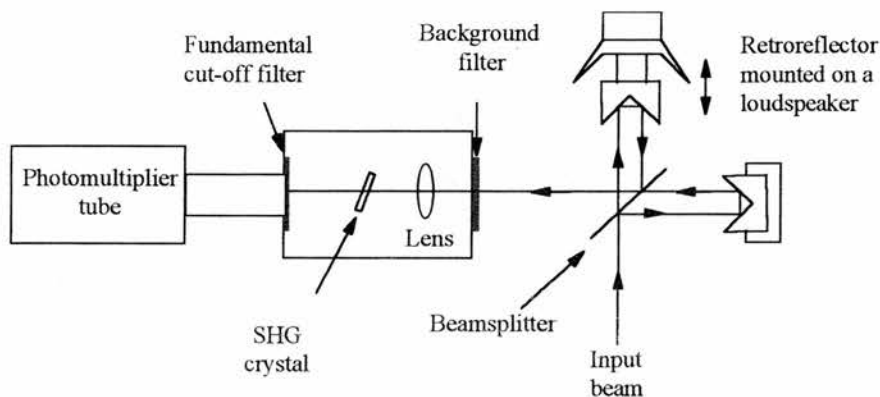


Figure 3.5 Autocorrelator set-up for measuring mode-locked pulses.

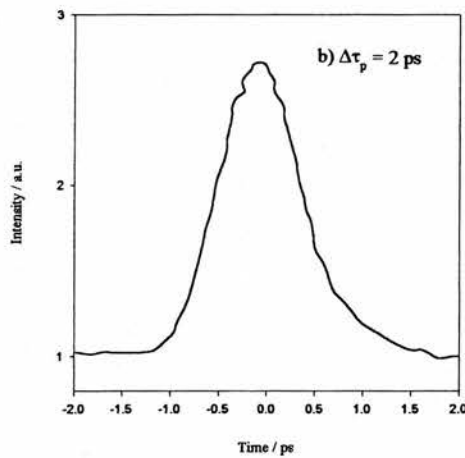
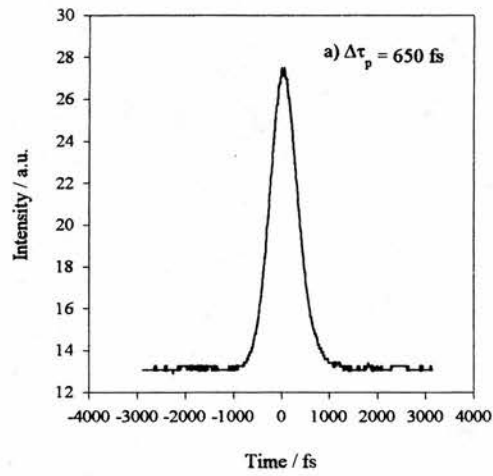


Figure 3.6 Intensity autocorrelation of a, a 650 fs colour-centre laser pulse and b, a 2 ps OPO pulse (FWHM).

3.4.4 *Pump-probe experimental set-up*

The standard experimental set-up is shown in figure 3.7. The laser output is steered into the pump-probe set-up and split in two by the beamsplitter. The pump pulses pass straight through the beamsplitter and are focused onto the sample by a 10 cm lens. The probe pulses reflected from the beamsplitter are delayed in an optical delay line to create the temporal variation between the arrival times of the pump and probe pulses on the sample.

The optical delay line consists of an aluminium retroreflector mounted on a stepper motor driven translation stage. The stage is computer controlled via an IEEE interface. The pulses are bounced off the retroreflector and then onto a plane mirror before being reflected back along their original path. The use of the plane mirror ensures probe beam pointing stability as the delay line is scanned. As there are four passes of the probe beam along the delay line the pulses see 4 mm of path change for every 1 mm that the stage is scanned. The probe pulses are then focused through the lens used to focus the pump pulses onto the sample and both pump and probe spots are overlapped at the focal point. Typically the probe is made much weaker in intensity than the pump pulse (1:20) using neutral density filters. The total path seen by the pump pulses is matched to that of the probe to give the zero delay point.

The pump beam was chopped with an optical chopper to allow phase sensitive detection. The modulation of the pump beam is transferred to the probe beam, which was measured using a large area germanium photodiode. Chopping the pump allows direct measurement of the change in transmission of the probe, which is the signal of interest. The motion of the delay stage and the collection of the data from the lock-in amplifier were under computer control.

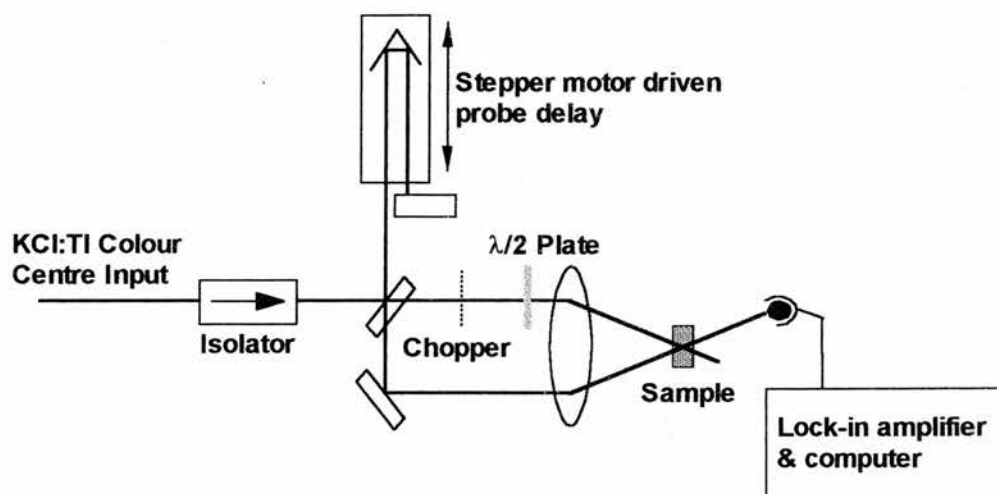


Figure 3.7 Experimental set-up for degenerate time-resolved pump-probe measurements

3.4.5 Spin relaxation studies

The experimental set-up for the investigation of spin relaxation is essentially the same as that previously described for degenerate pump-probe studies. The difference is the addition of $\lambda/4$ plates in the pump and probe arms to produce circularly polarised light, as shown in figure 3.8. The generation of circularly polarised light is verified by placing an analyser after the $\lambda/4$ plate and checking that the emerging signal is of equal intensity when the analyser is oriented parallel and perpendicular to the initially linearly polarised light.

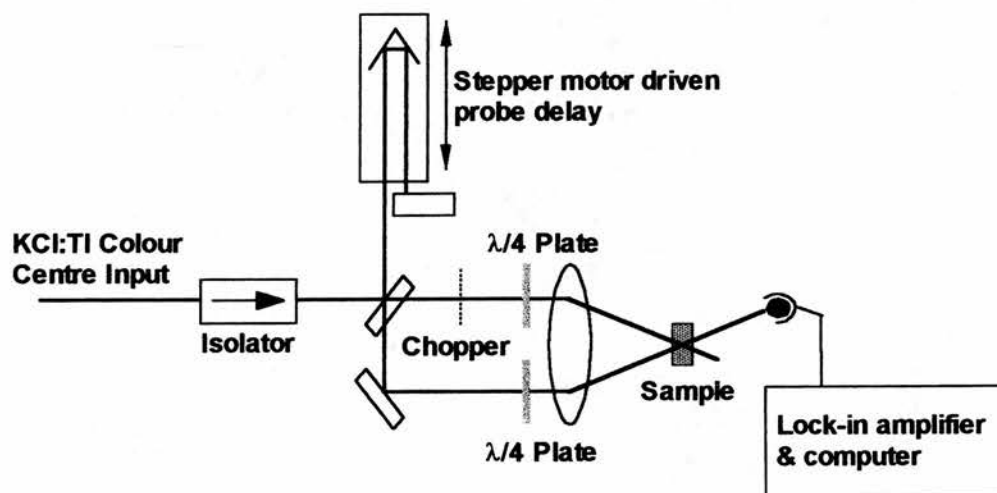


Figure 3.8 *Experimental set-up for spin relaxation studies*

3.5 References

- 3.1 L.F. Mollenauer, R.H. Stolen. "The soliton laser", *Opt. Letts.*, **9**, 1, 13-15. (1984).
- 3.2 G.T. Kennedy. "Ph.D. Thesis", University of St. Andrews, (1993).
- 3.3 S.D. Butterworth, P.G.R. Smith, D.C. Hanna. "Picosecond Ti:Sapphire pumped optical parametric oscillator based on periodically poled LiNbO₃", *Opt. Letts.*, **22**, 9, 618-620. (1997).

Chapter 4 Sample description and optical properties

4.1 Summary

This chapter introduces the samples that will be used in the following chapters and describes their basic optical properties.

4.2 Introduction

In this chapter the samples investigated will be described. The structure of each sample is outlined from the point of view of composition, quantum well width and doping levels. The linear absorption curves for the samples, measured using the experimental set-up shown in figure 3.1, are shown and the positions of the exciton resonances noted. A simple single beam saturation measurement was carried out on each sample to examine the intensity dependent saturation of the exciton resonance.

The results obtained from the above experiments are compared to the theoretical prediction of the optical properties, using simple models. The carrier densities are calculated for the power levels used in the experiments.

The samples are described in order of their serial numbers, beginning with MR535 (well width 9.0 nm), MR610 (well width 6.5 nm), MR611 (well width 5.5 nm) and MR850 (well width 9.5 nm). All the samples were grown at the EPSRC central facility for III-V semiconductors at the University of Sheffield by C. C. Button. All samples were grown by metalorganic vapour phase epitaxy (MOVPE).

The samples used were acquired from both University College London and Oxford University. They are all p-i-n structures, originally grown for use as quantum confined stark effect modulators, but in the work carried out in this thesis they are used to examine some fundamental physical properties of multiple quantum wells. It would have been preferable to use bulk quantum well material, where there is no built in field due to the p-i-n structure, and samples with a consistent quantum well material, either ternary or quaternary, to allow easier comparison of results. However, such material was unavailable at the commencement of this work.

4.3 Sample MR535

The structure of sample MR535 consists of 60 periods of 9.0nm $\text{In}_{0.53}\text{Ga}_{0.47}\text{As}_{0.95}\text{P}_{0.05}$ quantum wells separated by 7.5nm $\text{In}_{0.53}\text{Ga}_{0.47}\text{As}_{0.34}\text{P}_{0.66}$ barriers, grown lattice matched to an InP substrate in a p-i-n structure. Both the p and n regions were doped with acceptor and donor concentrations of about $3 \times 10^{18}/\text{cm}^3$. The sample was antireflection coated at Heriot-Watt University. The linear absorption curve for MR535 is shown in figure 4.1. The position of the heavy hole resonance is clearly resolved around 0.82eV.

The energy levels in the quantum wells of MR535 were calculated using graphical solutions to the equations for a finite potential well as described in chapter 2, assuming effective masses of 0.043m, 0.433m and 0.056m for the electrons and heavy and light holes respectively, where m is the electron rest mass. The bandgap of the quantum well material is 0.781 eV and the first energy level for the electron, E_e , the heavy hole, E_{hh} , and the light hole, E_{lh} , are given in the table below. These give the position of the band edge to be at approximately 0.871 eV and the heavy hole exciton resonance at 0.862 eV (assuming

an exciton binding energy of ~ 9 meV), corresponding to wavelengths of 1.42 μm and 1.44 μm respectively. It is probable that the difference between the calculated and observed values is due to fluctuations in the quaternary compositions during the growth process, as there is good agreement between the calculated heavy and light hole exciton separation of 0.033 eV and the observed separation of 0.028 eV.

| | E_e (eV) | E_{hh} (eV) | E_{lh} (eV) |
|-----------------|------------|---------------|---------------|
| 1 st | 0.082 | 0.008 | 0.041 |

Table 4.1 Energy levels in sample MR535.

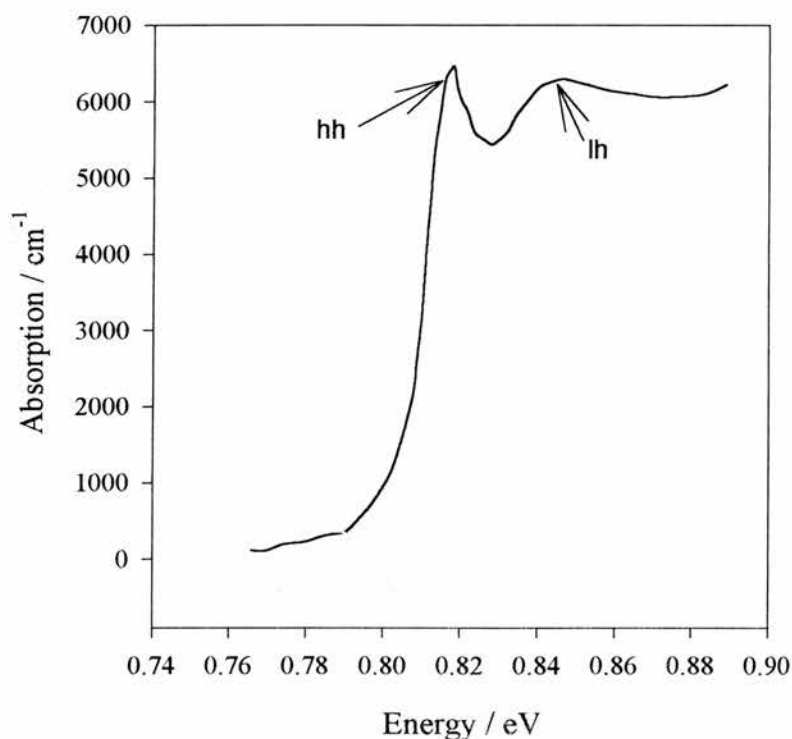


Figure 4.1 Linear absorption as a function of photon energy for sample MR535.

4.4 Sample MR610

The structure of sample MR610 consists of a 300 nm Zn doped p-layer, followed by a 200 nm intrinsic InP layer above 60 periods of 6.5nm $\text{In}_{0.53}\text{Ga}_{0.47}\text{As}$ quantum wells with 10.0nm $\text{In}_{0.53}\text{Ga}_{0.47}\text{As}_{0.34}\text{P}_{0.66}$ barriers and a 500 nm Si doped InP buffer layer. The acceptor concentration is $1 \times 10^{17}/\text{cm}^3$ and the donor concentration is $2 \times 10^{18}/\text{cm}^3$. The whole structure was grown lattice matched to an InP substrate and was antireflection coated at Heriot-Watt University. The linear absorption curve for MR610 is shown in figure 4.2. The position of the heavy hole resonance is clearly resolved at around 0.80eV.

The energy levels in the quantum wells of MR610 were calculated using graphical solutions to the equations for a finite potential well as described in chapter 2, assuming effective masses of 0.041m, 0.4235m and 0.05232m for the electrons and heavy and light holes respectively, where m is the electron rest mass. The bandgap of the quantum well material is 0.749 eV and the first energy level for the electron, E_e , the heavy hole, E_{hh} , and the light hole, E_{lh} , are given in the table below. These give the position of the band edge to be at approximately 0.916 eV and the heavy hole exciton resonance at 0.907 eV (assuming an exciton binding energy of ~ 9 meV), corresponding to wavelengths of 1.35 μm and 1.37 μm respectively. It is probable that the difference between the calculated and observed values is due to fluctuations in the quaternary compositions during the growth process, as there is reasonable agreement between the calculated heavy and light hole exciton separation of 0.053 eV and the observed separation of 0.032 eV. As this sample has InGaAs wells rather than InGaAsP, it is also possible that there is some strain in this sample.

| | E_e (eV) | E_{hh} (eV) | E_{lh} (eV) |
|-----------------|------------|---------------|---------------|
| 1 st | 0.152 | 0.015 | 0.068 |

Table 4.2 Energy levels in sample MR610.

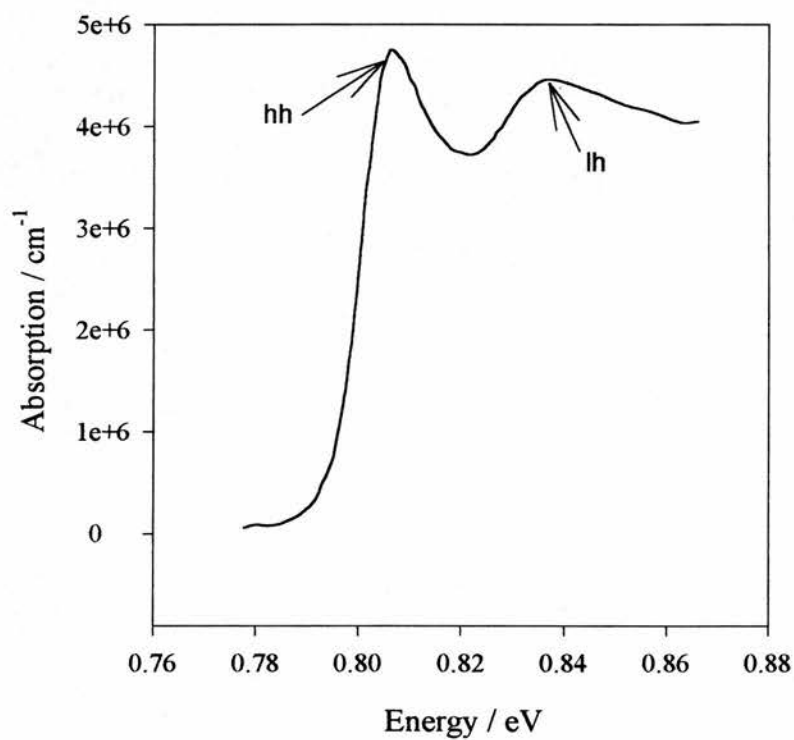


Figure 4.2 Linear absorption as a function of photon energy for sample MR610.

4.5 Sample MR611

Sample MR611 consists of 300 nm of Zn doped InP forming the p-layer, followed by a 200 nm intrinsic InP spacer, continuing with 60 periods of 5.5nm $\text{In}_{0.53}\text{Ga}_{0.47}\text{As}$ wells with 10.0nm $\text{In}_{0.53}\text{Ga}_{0.47}\text{As}_{0.34}\text{P}_{0.66}$ barriers and an Si doped 500 nm buffer layer. The acceptor concentration is $7 \times 10^{17}/\text{cm}^3$ and the donor concentration is $2 \times 10^{18}/\text{cm}^3$. The structure was grown lattice matched to an InP substrate and was antireflection coated at Heriot-Watt University. The linear absorption curve for MR611 is shown in figure 4.3. The position of the heavy hole resonance can be clearly resolved around 0.82eV.

The energy levels in the quantum wells of MR611 were calculated using graphical solutions to the equations for a finite potential well as described in chapter 2, assuming effective masses of 0.041m, 0.4235m and 0.05232m for the electrons and heavy and light holes respectively, where m is the electron rest mass. The bandgap of the quantum well material is 0.75eV and the first energy level for the electron, E_e , the heavy hole, E_{hh} , and the light hole, E_{lh} , are given in the table below. These give the position of the band edge to be at approximately 0.969 eV and the heavy hole exciton resonance at 0.960 eV (assuming an exciton binding energy of ~ 9 meV), corresponding to wavelengths of 1.28 μm and 1.30 μm respectively. It is probable that the difference between the calculated and observed values is due to fluctuations in the quaternary compositions during the growth process, as there is reasonable agreement between the calculated heavy and light hole exciton separation of 0.063 eV and the observed separation of 0.046 eV. As this sample has InGaAs wells rather than InGaAsP, it is also possible that there is some strain in this sample.

| | E_e (eV) | E_{hh} (eV) | E_{lh} (eV) |
|-----------------|------------|---------------|---------------|
| 1 st | 0.2 | 0.019 | 0.082 |

Table 4.3 Energy levels in sample MR611.

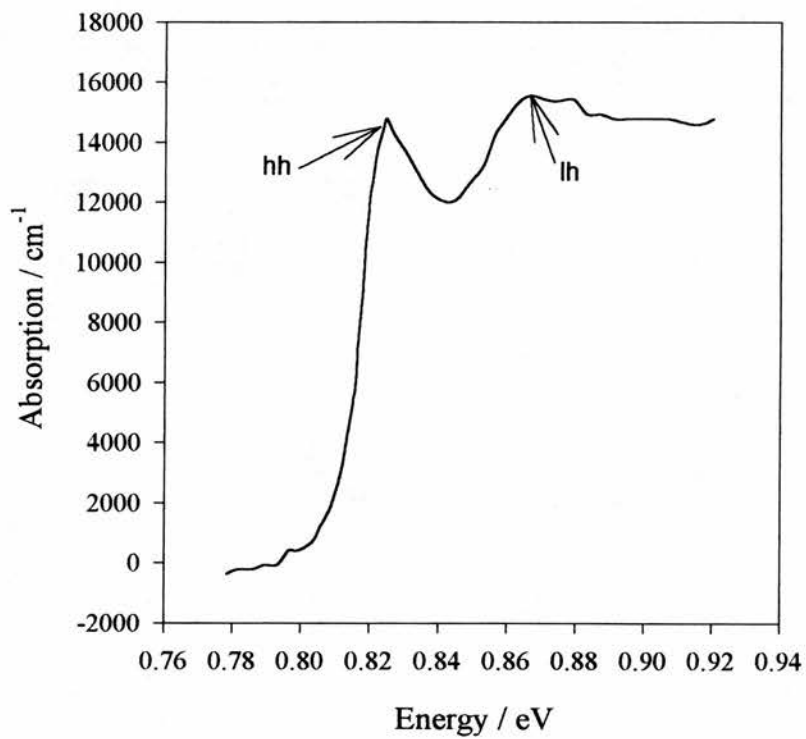


Figure 4.3 Linear absorption as a function of photon energy for sample MR611.

4.6 Sample MR850

Sample MR850 consists of 7 periods of 122.3 nm Zn doped InP and 114.2nm Zn doped $\text{In}_{0.53}\text{Ga}_{0.47}\text{As}_{0.73}\text{P}_{0.27}$ forming an antireflection quarter wave stack, followed by a 300 nm Zn doped InP p-layer and a 200 nm intrinsic InP buffer. Then come 60 periods of 9.5nm $\text{In}_{0.53}\text{Ga}_{0.47}\text{As}_{0.73}\text{P}_{0.27}$ quantum wells with 7.5nm $\text{In}_{0.53}\text{Ga}_{0.47}\text{As}_{0.34}\text{P}_{0.66}$ barriers, followed by a 2 μm Si doped InP buffer layer. The acceptor concentration is $3 \times 10^{18} \text{cm}^{-3}$ and the donor concentration is $3 \times 10^{18} \text{cm}^{-3}$. The whole structure was grown lattice matched on an InP substrate. The linear absorption curve for MR850 is shown in figure 4.4. The position of the heavy hole exciton can be resolved around 0.82eV. The light hole exciton resonance cannot be resolved in this sample.

The energy levels in the quantum wells of MR850 were calculated using graphical solutions to the equations for a finite potential well as described in chapter 2, assuming effective masses of 0.05114m, 0.4716m and 0.0722m for the electrons and heavy and light holes respectively, where m is the electron rest mass. The bandgap of the quantum well material is 0.885 eV and the first energy level for the electron, E_e , the heavy hole, E_{hh} , and the light hole, E_{lh} , are given in the table below. These give the position of the band edge to be at approximately 0.953 eV and the heavy hole exciton resonance at 0.944 eV (assuming an exciton binding energy of ~ 9 meV), corresponding to wavelengths of 1.30 μm and 1.32 μm respectively. It is probable that the difference between the calculated and observed values is due to fluctuations in the quaternary compositions during the growth process.

| | E_e (eV) | E_{hh} (eV) | E_{lh} (eV) |
|-----------------|------------|---------------|---------------|
| 1 st | 0.061 | 0.007 | 0.029 |

Table 4.4 Energy levels in sample MR850.

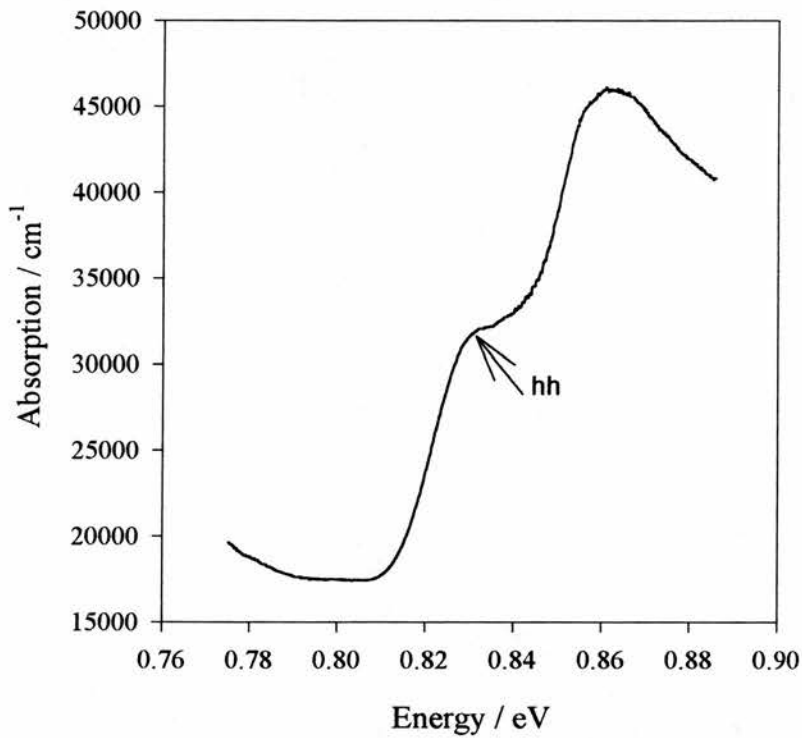


Figure 4.4 Linear absorption as a function of photon energy for sample MR850.

4.7 Single beam saturation measurements

Single beam saturation measurements were carried out on each sample. The laser was tuned to the heavy hole exciton resonance and the absorption of the beam was measured as a function of the laser intensity. The measure of absorption, αd , is defined in the Beer-Lamberts law (assuming no other losses) as

$$I = I_0 e^{-\alpha d} \quad (4.1)$$

where I is the transmitted intensity, I_0 the incident intensity, α the absorption coefficient and d the thickness of the sample. The values of αd obtained, assuming a constant absorption depth, are plotted against average incident intensity in figures 4.5 to 4.8 for samples MR535, MR610, MR611 and MR850 respectively. Given αd and a description of the laser it is relatively straightforward to calculate an approximate number of carriers excited by each pulse.

The colour centre laser has a repetition rate of 82 MHz. Assuming an average power of 1 mW gives a pulse energy of ~ 10 pJ. The peak power of the pulse can be calculated if the pulse width is known. For this work pulse widths of 150 fs and 500 fs are used. In the case of the 150 fs pulses the peak power is ~ 65 W, while for 500 fs pulses the peak power is ~ 20 W. The PPLN OPO also has a pulse energy of ~ 10 pJ at an average power of 1 mW, giving a peak power of 5 W for the 2 ps pulses produced. The spot size after the focusing lens was measured with a beam profiler to be of radius 40 μm . Using this, the peak intensity of the pulses is found to be $\sim 1 \times 10^6$ Wcm^{-2} for the 150 fs case, $\sim 4 \times 10^5$ Wcm^{-2} for the 500 fs case and 1×10^5 Wcm^{-2} for the 2 ps case.

The number of photons absorbed is given by

$$N_{\text{photons}} = \frac{E_{\text{pulse}} (1 - e^{-\alpha d})}{\hbar \omega} \quad 4.2$$

Where E_{pulse} is the pulse energy and $\hbar\omega$ is the photon energy. If the internal quantum efficiency is assumed to be 100%, then every absorbed photon creates a free electron-hole pair. The carrier densities generated in each sample are summarised in table 4.5.

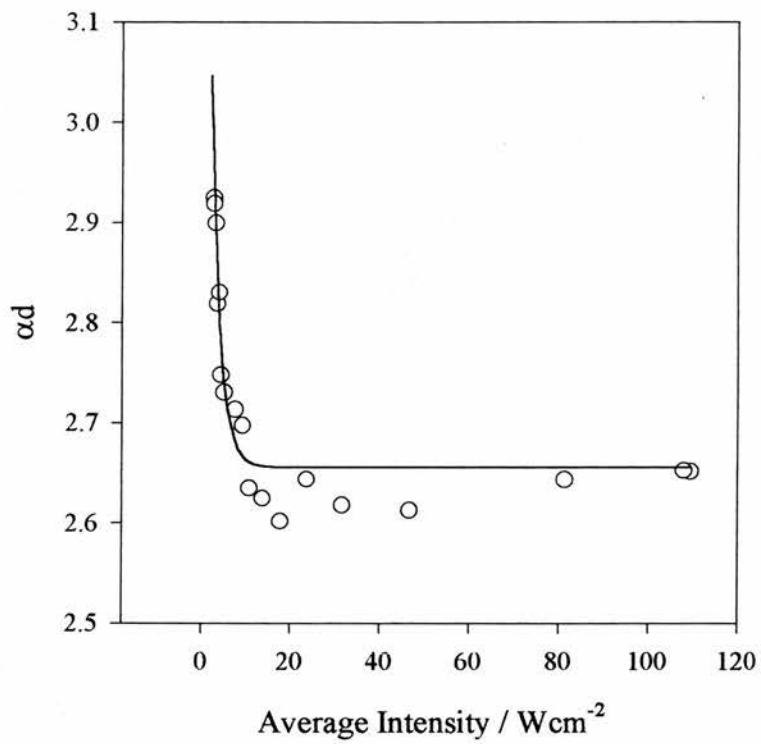


Figure 4.5 Change in absorption of a single beam for sample MR535 at the heavy hole exciton resonance with a spot size of $40 \mu\text{m}$.

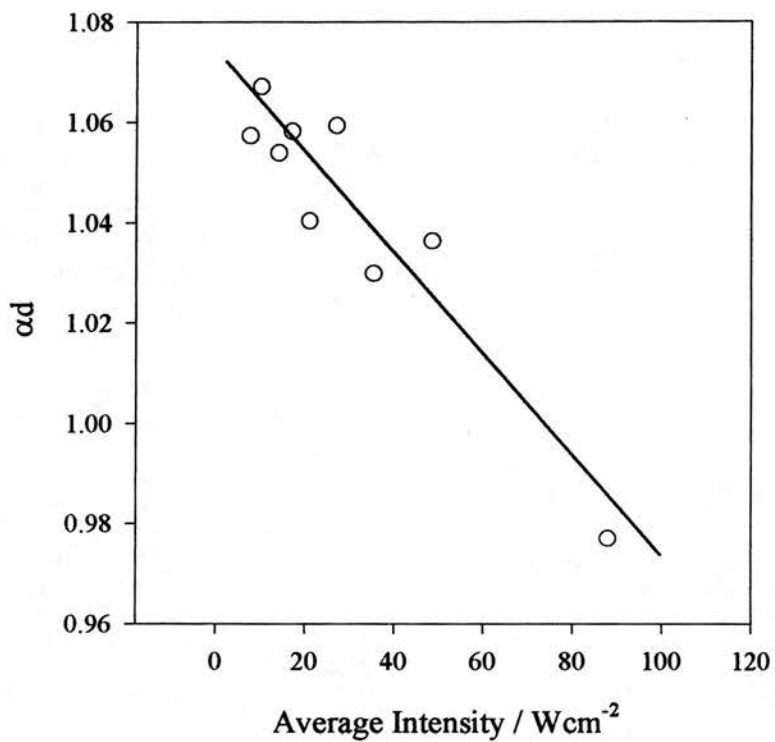


Figure 4.6 Change in absorption of a single beam for sample MR610 at the heavy hole exciton resonance with a spot size of 40 μm .

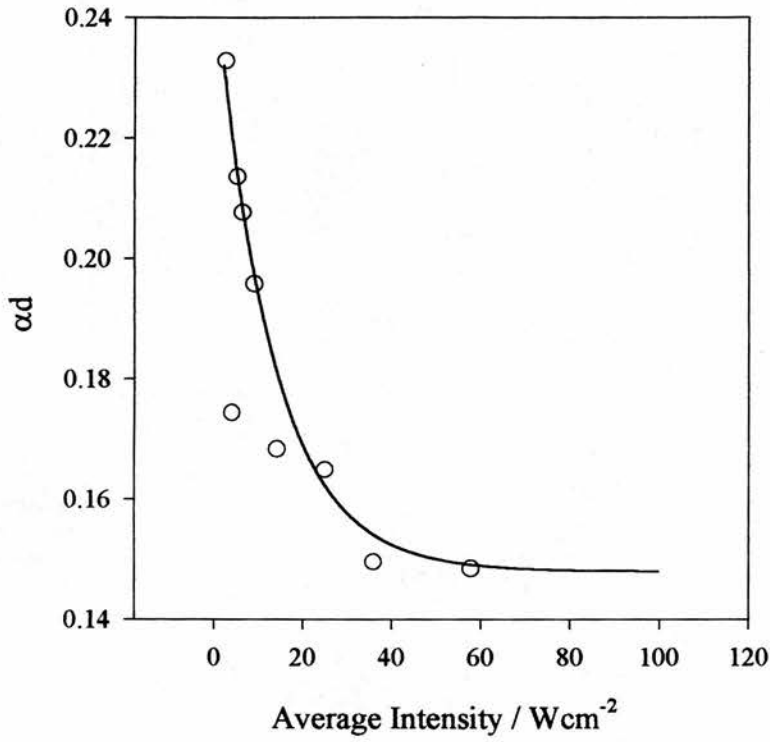


Figure 4.7 Change in absorption of a single beam for sample MR611 at the heavy hole exciton resonance with a spot size of $40 \mu\text{m}$.

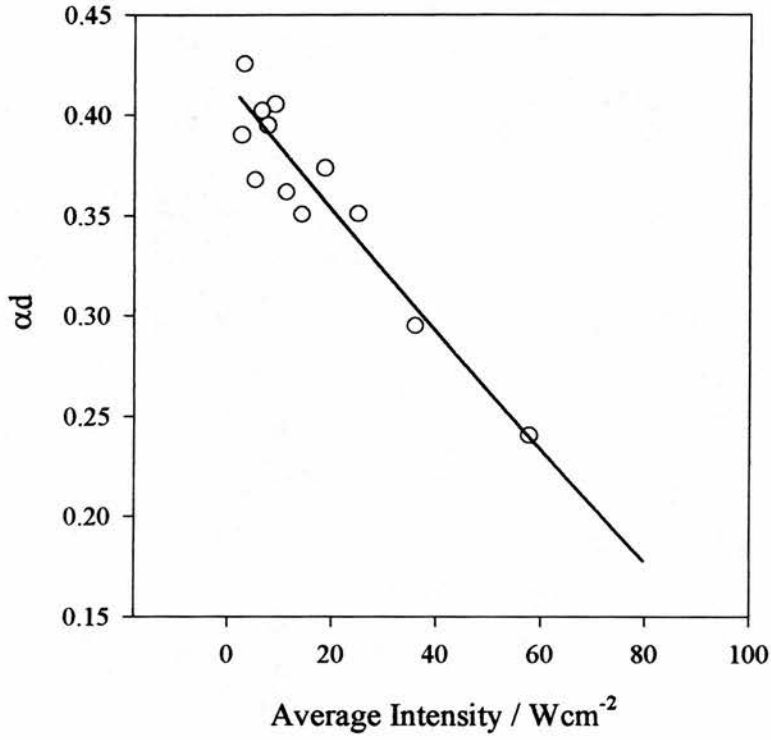


Figure 4.8 Change in absorption of a single beam for sample MR850 at the heavy hole exciton resonance with a spot size of $40 \mu\text{m}$.

| <i>Sample</i> | <i>Number of electron hole pairs created / cm^{-2}</i> |
|---------------|---|
| MR535 | 0.7×10^8 |
| MR610 | 0.5×10^8 |
| MR611 | 0.1×10^8 |
| MR850 | 0.2×10^8 |

Table 4.5 *Excited carrier densities for 1 mW of average pump power.*

4.8 Discussion

It is clear from the results of the saturation measurements, shown in figures 4.5 to 4.8, that in every sample the absorption begins to saturate below the minimum power at which it was possible to measure the transmission by straightforward means. Hence for the results presented in the rest of this thesis experiments are always carried out in the regime where the absorption is at least partially saturated. It can also be seen that αd shows a linear dependence on input power for both MR610 and MR850, suggesting that in the power range studied, the absorption in both these samples is a long way from being fully saturated, in contrast to samples MR535 and MR611, where the absorption can be seen to fully saturate for input powers of around 0.5 mW and 3 mW respectively.

Chapter 5 Carrier lifetime measurements

5.1 Summary

In this chapter carrier lifetime in multiple quantum wells is investigated. The carrier lifetimes in a number of quantum well samples of varying well widths are measured and the mechanisms leading to carrier escape are discussed.

5.2 Introduction

In most bandgap resonant devices the speed of response depends strongly on how quickly photogenerated carriers leave the quantum wells. Excitons created by optical excitation at the heavy-hole exciton resonance ionise into free carriers within hundreds of femtoseconds [5.1]. In the absence of any external bias, these free carriers can be removed from the wells through three mechanisms: electron-hole recombination, tunnelling and thermionic emission. Each of the three processes will lead to an exponential decay in the carrier density as a function of time with characteristic decay times of τ_r , τ_{tu} and τ_{te} for recombination, tunnelling and thermionic emission respectively. Assuming that the three processes are independent, the charge density and consequently the change in transmission of the sample will be proportional to the product of the three decaying exponentials. The overall time constant is given by

$$\frac{1}{\tau} = \frac{1}{\tau_r} + \frac{1}{\tau_{tu}} + \frac{1}{\tau_{te}} \quad (5.1)$$

For thermionic emission to occur, carriers must absorb thermal energy from the lattice and acquire a distribution of energies. Some fraction of the carriers can then have energies greater than the height of the well and escape. Different physical parameters for electrons and holes lead to different emission rates for the two carrier types. The time constant for thermionic emission was derived by Schneider and Von Klitzing assuming instantaneous thermalisation of the carriers and a Boltzmann distribution for the carriers near the top of the well [5.2]. The escape time is given by

$$\tau_{te_{e,h}} = \left(\frac{2\pi m_{e,h} L^2}{k_B T} \right)^{1/2} \exp \left(\frac{V_{e,h} - E_{e,h} - eF \cdot \frac{L}{2}}{k_B T} \right) \quad (5.2)$$

where m is the carrier mass, V is the barrier height, E is the energy level in the well, F is the electric field across the well, L is the well width, T is the temperature, k_B is the Boltzmann constant and the subscripts e and h denote electrons and holes respectively.

For zero field the time constant is a strong function of the term $V_{e,h} - E_{e,h}$, which is the effective height of the barrier over which the carriers must escape. Any applied field serves to reduce the effective barrier height. Table 5.1 gives the room temperature escape times for electrons and heavy holes in the $n=1$ level predicted by equation 5.2 for the samples studied.

In samples of high purity, the electron hole recombination rate is proportional to the overlap between the electron and hole densities in the quantum well [5.3] and is generally of the order of a few nanoseconds.

| <i>Sample</i> | <i>Depth of cb well (eV)</i> | <i>Electron τ_{th} (ps)</i> | <i>Depth of vb well (eV)</i> | <i>Hole τ_{th} (ps)</i> |
|---------------|----------------------------------|---|----------------------------------|---|
| MR535 | 0.14 | 0.65 | 0.21 | 550 |
| MR610 | 0.151 | 1.3 | 0.226 | 560 |
| MR611 | 0.151 | 0.75 | 0.226 | 410 |
| MR850 | 0.096 | 0.31 | 0.145 | 50 |

Table 5.1 *Calculated thermionic emission times.*

The third process through which carriers can escape from the well is tunnelling.

The tunnelling time is given by

$$\tau_{tu_{e,h}} = k \exp\left(-\frac{4}{3\hbar F} \sqrt{2m_{e,h}} \left[(V_{e,h} - E_{e,h} - Fb)^{1/2} - (V_{e,h} - E_{e,h})^{1/2} \right]\right) \quad (5.3)$$

where b is the barrier thickness and k is a constant [5.4]. Electric field dependent studies of escape time have shown that carrier escape does not follow the functional form for tunnelling given in equation 5.3, suggesting that tunnelling is a small effect compared to thermionic emission and recombination [5.5], although this depends strongly on both sample structure and voltage conditions. It should be noted that because the samples under investigation are all p-i-n structures there is a small built-in voltage of around 0.5 V which will sweep out any thermally excited carriers.

5.3 Experimental details

Studies of the carrier lifetime in InGaAs(P)/InGaAsP multiple quantum wells were carried out at room temperature using the experimental set-up shown in figure 3.7. The

samples were excited at the heavy hole resonance and both pump and probe pulses were linearly polarised and orthogonally oriented. Great care was needed when lining up the delay stage to ensure that there was no walk-off of the pump and probe beams as the delay was scanned, because of the long scans involved in these measurements.

5.4 Results

Experiments were carried out on four different samples of varying well width. The samples used were MR535, MR610, MR611 and MR850. The variation of the probe transmission as a function of delay is plotted for each sample in figures 5.1 to 5.4 and the measured carrier lifetimes are shown in table 5.2.

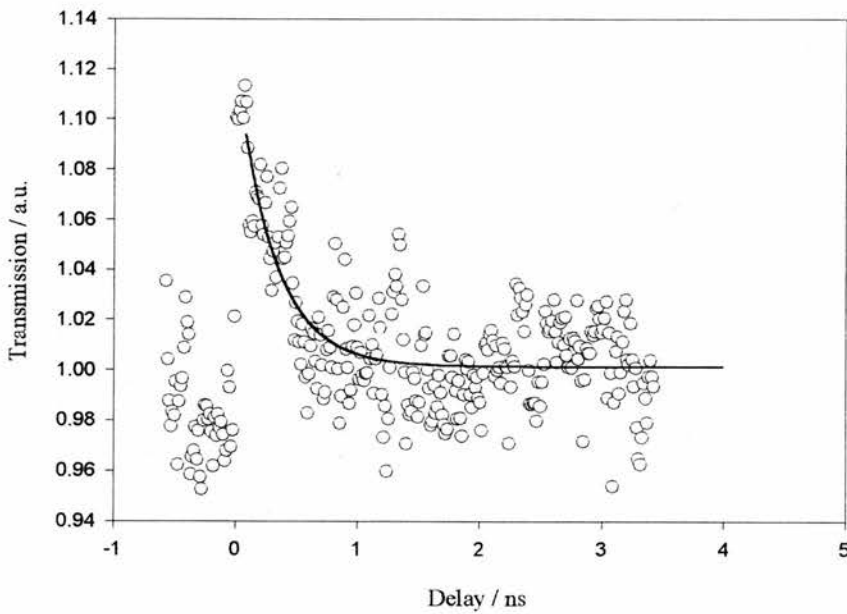


Figure 5.1 Change in transmission of sample MR535 at the heavy hole exciton as a function of probe pulse delay time. The line shows the fitted curve.

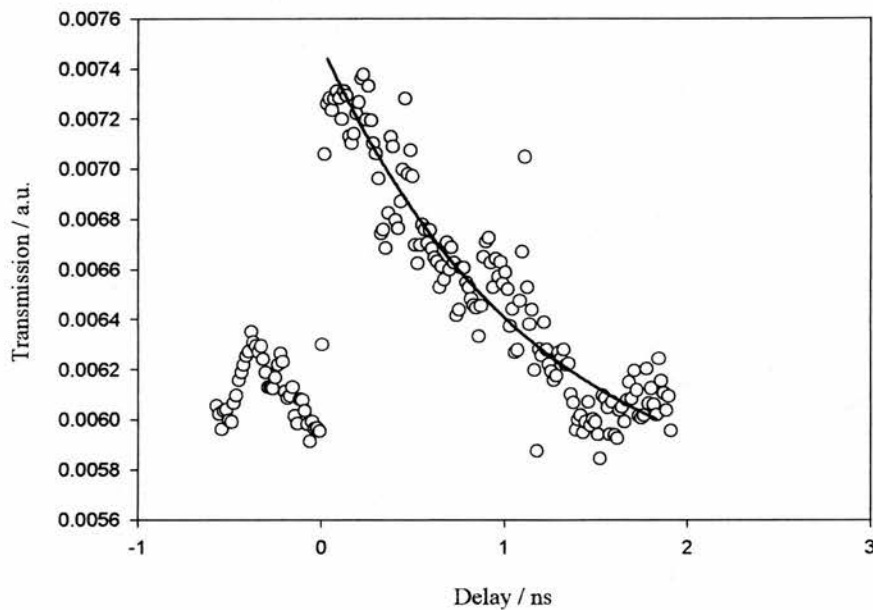


Figure 5.2 Change in transmission of sample MR610 at the heavy hole exciton as a function of probe pulse delay time. The line shows the fitted curve.

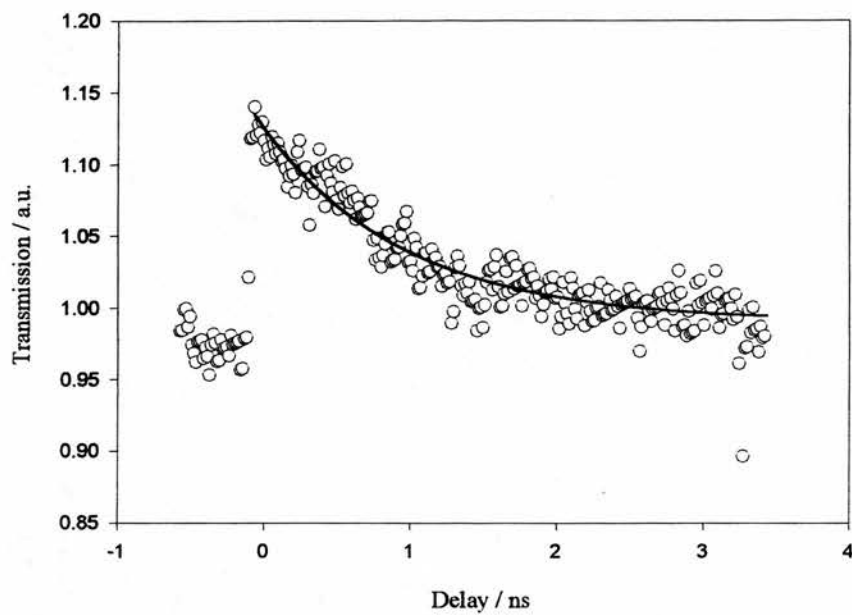


Figure 5.3 *Change in transmission of sample MR611 at the heavy hole exciton as a function of probe pulse delay time. The line shows the fitted curve.*

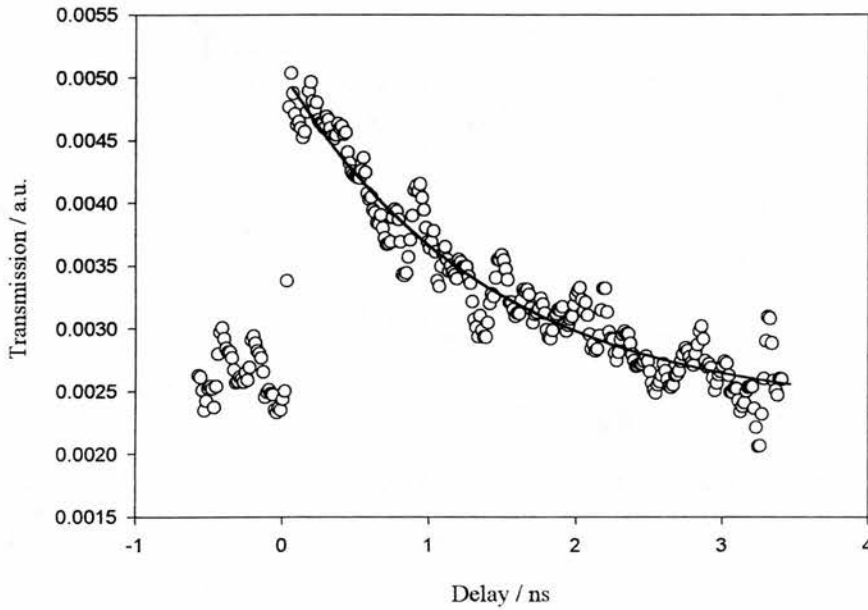


Figure 5.4 Change in transmission of sample MR850 at the heavy hole exciton as a function of probe pulse delay time. The line shows the fitted curve.

| <i>Sample</i> | <i>Well width (nm)</i> | <i>Carrier lifetime (ns)</i> |
|---------------|------------------------|------------------------------|
| MR535 | 9.0 | 0.31 ± 0.14 |
| MR610 | 6.5 | 1.2 ± 0.29 |
| MR611 | 5.5 | 0.98 ± 0.23 |
| MR850 | 9.5 | 1.5 ± 0.24 |

Table 5.2 Measured carrier lifetimes

5.5 Discussion

The measured carrier lifetimes in samples MR610, MR611 and MR850 show no definite well width dependence. They are all considerably longer than the calculated thermionic emission times for the electrons. The small built in field will sweep any escaping carriers towards the p and n regions, but it is probable that carriers emitted from one quantum well into the continuum will be recaptured by other wells, which has the effect of increasing the effective carrier escape time. Experiments and modelling of GaAs MQW's indicate capture times into the wells of about 0.5 ps [5.6]. Also, the slow emission rate of holes will reduce the sweep-out of electrons because of the created fields that would ensue. It seems reasonable to suppose, therefore, that the carrier lifetime in these samples is dominated by recombination.

In sample MR535, however, the measured carrier lifetime is of the order of the heavy hole emission time, but considerable longer than the electron emission time. As the fastest effect would be expected to dominate the carrier lifetime, it seems reasonable to presume in this case that the lifetime is again dominated by recombination. The electron thermionic emission can be followed by recapture if the electrons are not swept out, but the carriers may recombine before the holes have been thermally excited from the wells.

For the experiments described in the rest of this thesis it is important to know the carrier lifetime so that its effect can be accounted for whilst measuring effects on shorter timescales.

5.6 References

- 5.1 W.H. Knox, R.L. Fork, M.C. Downer, D.A.B. Miller, D.S. Chemla, C.V. Shank, "Femtosecond dynamics of resonantly excited excitons in room temperature GaAs quantum wells", *Phys. Rev. Lett.*, **54**, 1306-1309, (1985).

- 5.2 H. Schneider, K. Von Klitzing, "Thermionic emission and Gaussian transport of holes in a GaAs/Al_xGa_{1-x}As multiple quantum well structure", *Phys. Rev. B.*, **38**, 9, 6160-6165, (1988).
- 5.3 G. Lasher, F. Stern, "Spontaneous and stimulated recombination radiation in semiconductors", *Phys. Rev.*, **133**, 2A, A553-563, (1964).
- 5.4 T.B. Norris, X.J. Song, W.J. Schaff, L.F. Eastman, G. Wicks, G.A. Mourou, "Tunnelling escape time of electrons from a quantum well under the influence of an electric field", *Appl. Phys. Lett.*, **54**, 1, 60-62, (1989).
- 5.5 J.A. Cavailles, D.A.B. Miller, J.E. Cunningham, P. LiKamWa, A. Miller, "Simultaneous measurements of electron and hole sweep out from quantum wells and modelling of photoinduced field screening dynamics", *IEEE J. Quant. Electr.*, **28**, 10, 2486-2497, (1992).
- 5.6 H. Wang, "Ph.D. Thesis", University of Central Florida, (1995).

Chapter 6 Screening, broadening and phase space filling

6.1 Summary

The relative contributions of screening, broadening and phase space filling to exciton saturation in multiple quantum wells are investigated. The effects arising from phase space filling are distinguished from those due to screening and broadening using the spin dependent contribution made by phase space filling. The contributions of broadening and screening are separated with the use of two different optical pulse widths to distinguish between effects causing broadening of the exciton linewidth and those causing a reduction of the oscillator strength. The results obtained for samples of varying well width are presented and discussed.

6.2 Introduction

The effects of screening, broadening and phase space filling are important parameters for the measurement of optical non-linearities and monitoring carrier dynamics. These effects can also limit the performance of a number of device applications at high optical intensities where high densities of optically excited carriers are created. This chapter describes experiments that have been carried out to investigate the relative strengths of the screening, broadening and phase space filling contributions to exciton saturation in a number of multiple quantum well samples of varying well widths.

Saturation of the exciton absorption can result from both exclusion effects and Coulombic effects such as screening and / or broadening. These effects have been described in chapter 2 and so will only be briefly described here. Effects arising from the

Pauli exclusion principle can be described as phase space filling (PSF). This arises as carrier densities increase, occupying low lying k -states, thus blocking transitions arising from these states. Excitons are derived from these low-lying states, so the filling of the band states rules out the possibility of creating their associated excitons.

Exciton saturation is also caused by the screening properties of large densities of free carriers. The presence of free carriers modifies the dielectric constant of the semiconductor, increasing the size of the exciton orbit. This leads to a reduction of the absorption strength. At high carrier densities, exchange effects for particles of equal spin further modify the screened Coulomb potential and Coulomb associated effects for all particles. The exchange effects arise due to Pauli exclusion which further separates the electrons, again increasing the size of the exciton. This phenomenon is known as exchange-screening. In addition, equally charged fermions with different quantum numbers will also avoid each other due to Coulomb repulsion. This effect is known as Coulomb-hole and will also reduce the overall energy of the system. These effects are very short-ranged when compared to the long-range Coulomb interactions that give rise to classical screening. Long range electrostatic screening is known to be of less importance in 2D than in 3D [6.1]. This reduction in the effect of screening can be considered to be due to the reduced number of dimensions that the carriers are free to move in.

Broadening of the exciton resonance will lead to reduced absorption at the peak of the exciton, while increasing the exciton linewidth to maintain the overall oscillator strength. Broadening can be either inhomogeneous or homogeneous. Inhomogeneous broadening is due to local potential fluctuations, which arise due to imperfections in the semiconductor structure. The main sources of inhomogeneous broadening are interface roughness, alloy potential fluctuations or well to well width fluctuations in MQWs. In the GaAs system, the well material is a binary compound, so there is no alloy scattering. In

high quality GaAs MQWs, an exciton absorption linewidth of 3 to 4 meV is achievable. In InGaAs or InGaAsP MQWs however, alloy scattering effects can cause broadening of the exciton linewidth of the order of 3 to 5 meV.

Homogeneous broadening is caused by acoustic and optical phonon scattering, carrier-carrier scattering and any other mechanisms affecting the exciton lifetime, such as tunnelling or recombination. In high quality MQWs the exciton linewidth is usually determined by phonon scattering at room temperature. However, if the carrier density is increased by optical excitation, then collisions between free carriers becomes the dominant scattering mechanism that leads to broadening.

Schmitt-Rink et. al. [6.2] separated the free carrier Coulomb screening into the long-range classical term and the exchange contribution. They predicted that the long range Coulomb effect would be negligible in quantum wells but that the PSF and exchange contributions would be comparable. To separate PSF and Coulomb effects experimentally, non-equilibrium carrier distributions have been employed [6.1]. Exciting into continuum states allowed the long range screening term to be isolated and confirmed that it was negligible. This approach could not distinguish the exchange effects and PSF, however, because these are both dependent on the plasma energy.

An alternative method of creating a non-equilibrium carrier distribution is to use circularly polarised light to excite spin polarised populations of carriers. The selection rules discussed in chapter 2 dictate that 100% spin polarised carriers can be created by circularly polarised light resonant with the heavy hole transition. At room temperature, hole spins are randomised on femtosecond timescales due to scattering into the mixed-spin light hole band while electron spin polarisation is typically maintained for several picoseconds after exciton ionisation. Circular polarisations have been employed

previously in both low temperature [6.3, 6.4] and room temperature [6.5] studies in GaAs MQWs.

In the following experiment, the spin dependent nature of PSF is utilised to separate the relative contributions of screening, broadening and PSF to exciton saturation. The time resolved pump-probe technique used to resolve the circular dichroism of the exciton saturation is shown schematically in figure 6.1.

When a linearly polarised pump pulse is made resonant with the heavy hole exciton transition in a quantum well, equal populations of spin up and spin down carriers are created. This process is shown in figure 6.1(a). The conduction band of the semiconductor is drawn with two halves (labelled \uparrow and \downarrow). These correspond to the two possible spin states of electrons in the conduction band. A probe pulse of orthogonal linear polarisation (OLP) arriving after the pump pulse will see an increase in the transmission of the sample due to the effects of screening, broadening and PSF.

If the pump pulse consists of circularly polarised light, however, then only one spin state of the conduction band is populated as shown in figure 6.1(b) and (c). A probe pulse of the same circular polarisation will then examine the population of this spin state and see a reduced absorption due to PSF when compared to the OLP case (figure 6.1(b)). In the case of a probe pulse with opposite circular polarisation as shown in figure 6.1(c) the probe pulse examines the empty spin states, so in this case there is no contribution to the exciton saturation from PSF. The populations of the two spin states equalise over time due to spin relaxation, which will be discussed in the following chapter.

Since the exciton ionisation time due to phonon scattering is of the order of a few hundred femtoseconds at room temperature, exciton-exciton interactions are only significant on femtosecond timescales whereas free carrier interactions will dominate over picosecond and longer timescales

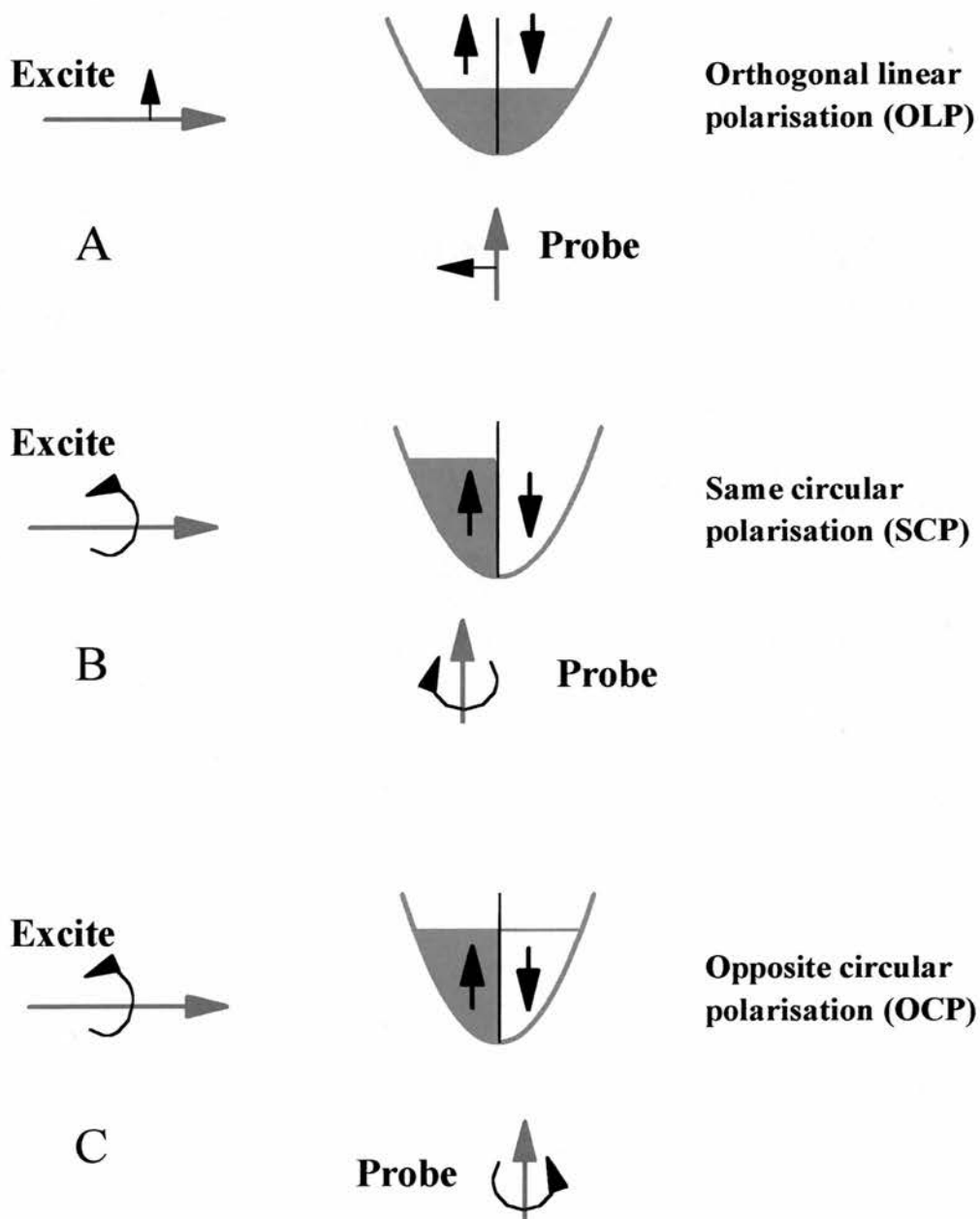


Figure 6.1 Illustration of the spin state populations examined with, (a) orthogonal linear polarisation, (b) same circular polarisation and (c) opposite circular polarisation.

Snelling et. al. [6.5] separated the contributions of PSF and Coulomb effects in AlGaAs / GaAs quantum wells using this technique. However, the study could not quantitatively separate the contributions of Coulomb screening and broadening. Later

studies in GaAs [6.6, 6.7] have made use of the bandwidth of modelocked laser pulses to separate the contributions of Coulomb screening and broadening. The studies used both pulses of 1ps duration with a bandwidth of approximately 1nm [6.6] and shorter pulses of 100fs duration and a bandwidth of 10nm [6.7] to separate effects due to a broadening of the exciton linewidth and effects due to a reduction of the oscillator strength. The transmission change a 1ps pulse experiences is due to the combined effects of screening, broadening and PSF. The 100fs pulses, however, had a bandwidth greater than the heavy hole exciton absorption linewidth. Consequently, the probe in this case measured the integrated absorption change, rather than the change at line centre, thus ‘seeing’ no change due to broadening.

6.3 Experimental details

Exciton saturation in InGaAs(P) / InGaAsP multiple quantum wells, at room temperature, was investigated using the degenerate pump-probe technique described in figure 3.8. Pulses of both 150fs and 650fs duration were used.

6.4 Results

The experiment was carried out in three quantum well samples of varying well width in order to contrast the effects. The samples used were MR535 (9.0nm well widths), MR610 (6.5nm well widths) and MR611 (5.5nm well widths). Each sample was excited resonant with the heavy hole exciton and the time evolution of the exciton saturation recovery monitored with a time delayed probe pulse. The transmission changes were measured for pump and probe pulses with OLP, SCP and OCP polarisation configurations as described previously. The production of circular polarisation was

achieved by inserting a $\lambda/4$ plate in both the pump and probe arms. Figure 6.2 compares the linewidth of the heavy hole resonance with the bandwidths of the 150fs and 560fs pulses.

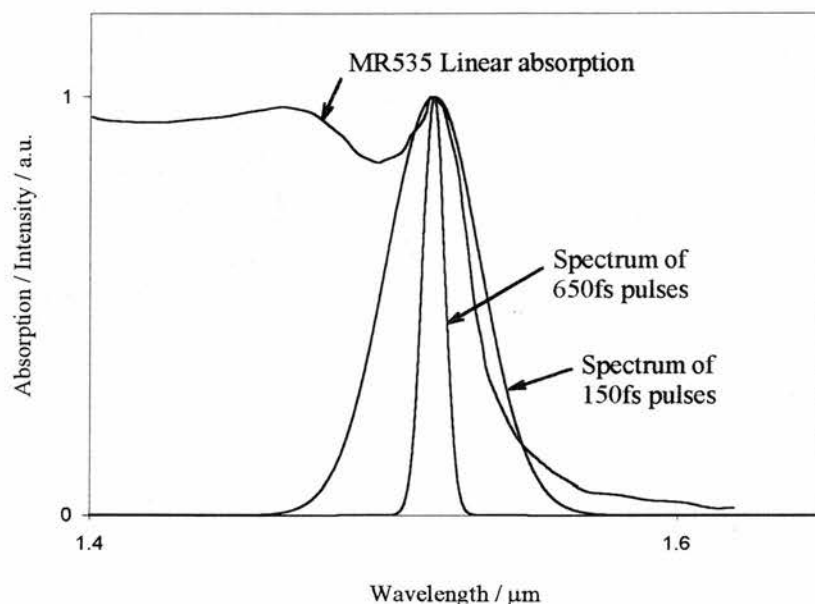


Figure 6.2 Comparison of the bandwidths of transform limited 150fs and 650fs pulses with the heavy hole linewidth of sample MR535.

Figure 6.3 shows a typical result for excitation of sample MR535 with both 150fs pulses and 650fs pulses. The experiment was repeated for varying pump powers with the 650fs pulses, allowing the carrier density dependence of the initial transmission change to be measured. Figures 6.4, 6.5 and 6.6 show the initial change in transmission as a function of estimated carrier density, assuming an internal quantum efficiency of one, and an average αd of 2.6 for sample MR535, 1 for sample MR610 and 0.15 for sample

MR611 respectively. The spot radius was $40\mu\text{m}$. The curve labelled Coulomb is a measure of the initial transmission change when the pump and probe pulses are set for OCP. The PSF curve shows the initial difference in transmission change between the OCP and SCP configurations.

Figure 6.7 shows a typical set of 'long' and 'short' range traces for sample MR535. The long range traces were measured using $50\mu\text{m}$ steps, corresponding to a change in delay of 320fs / step, while the short range traces used $10\mu\text{m}$ steps, corresponding to a change in delay of 66fs / step.

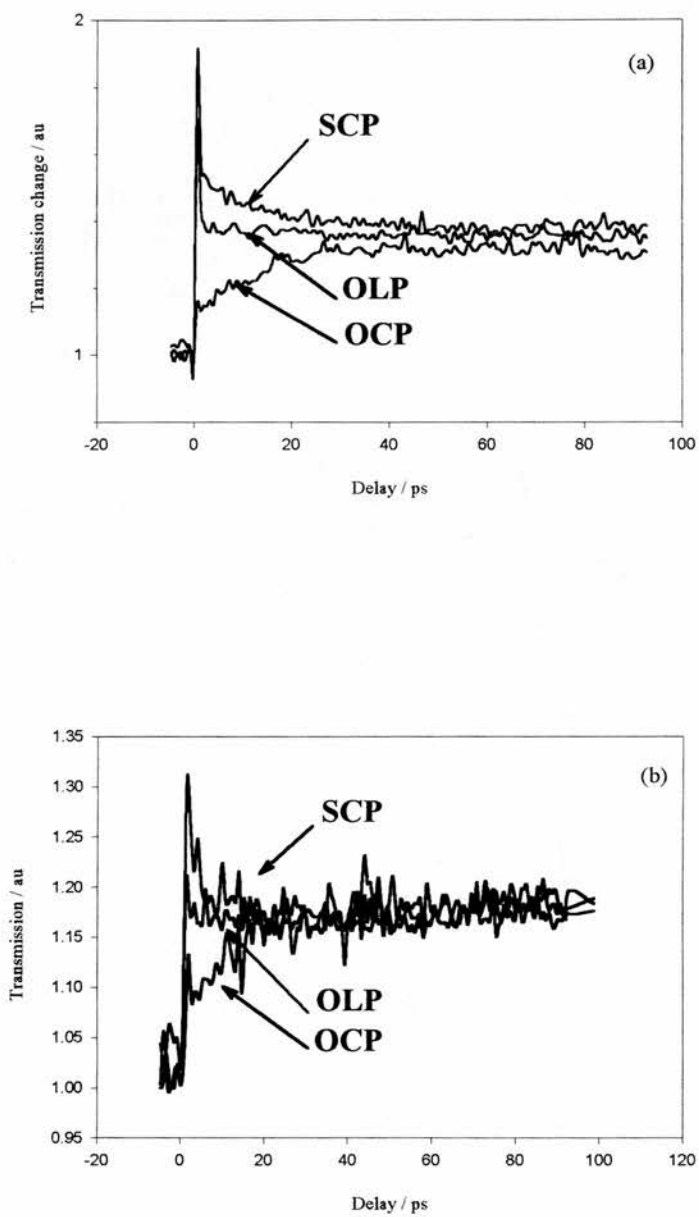


Figure 6.3 Typical pump-probe traces for the sample MR535 using (a) 150fs pulse and (b) 650fs pulses in the three polarisation configurations OLP, SCP and OCP.

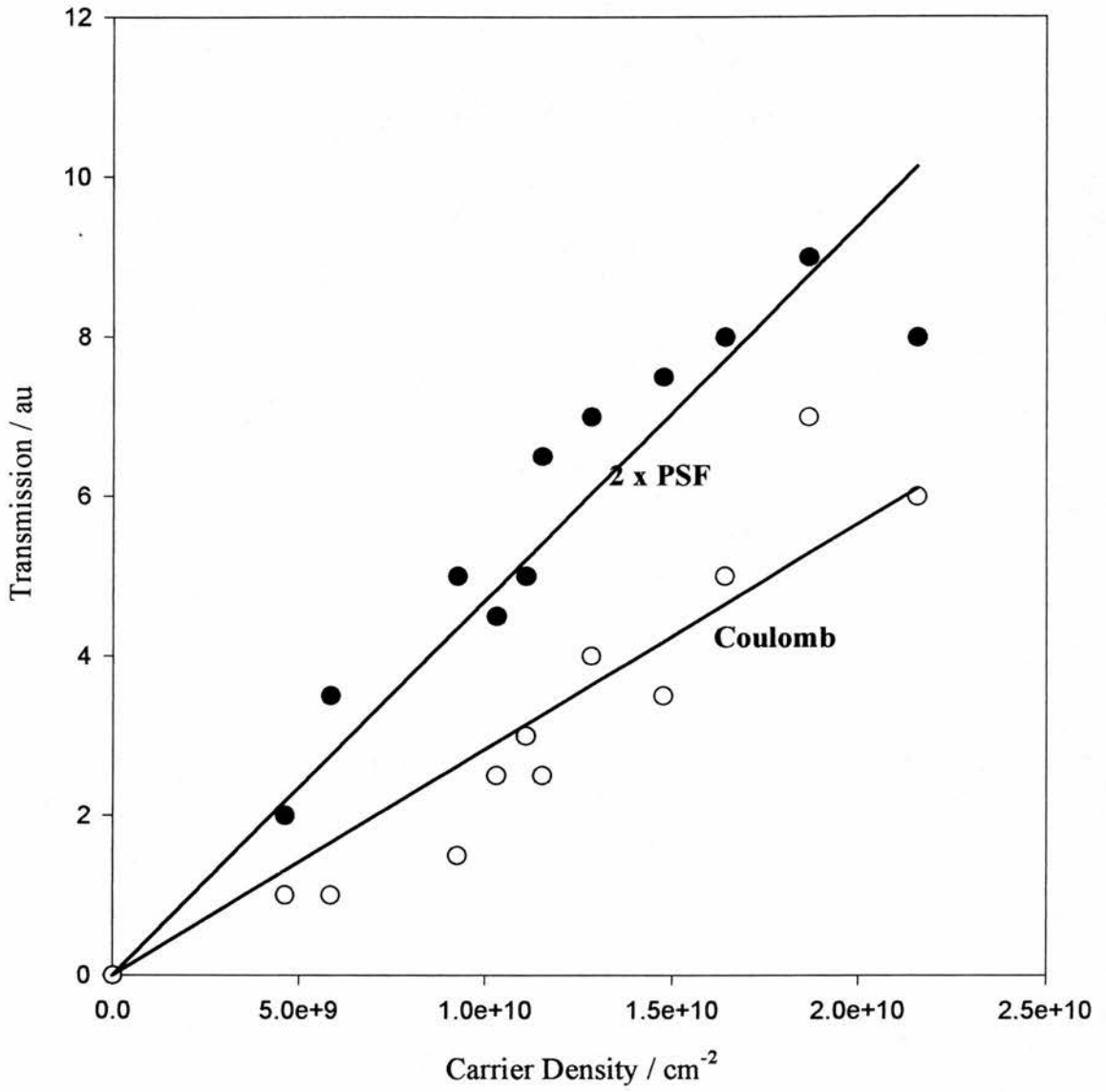


Figure 6.4 Initial change in transmission at the heavy hole exciton resonance as a function of carrier density for sample MR535.

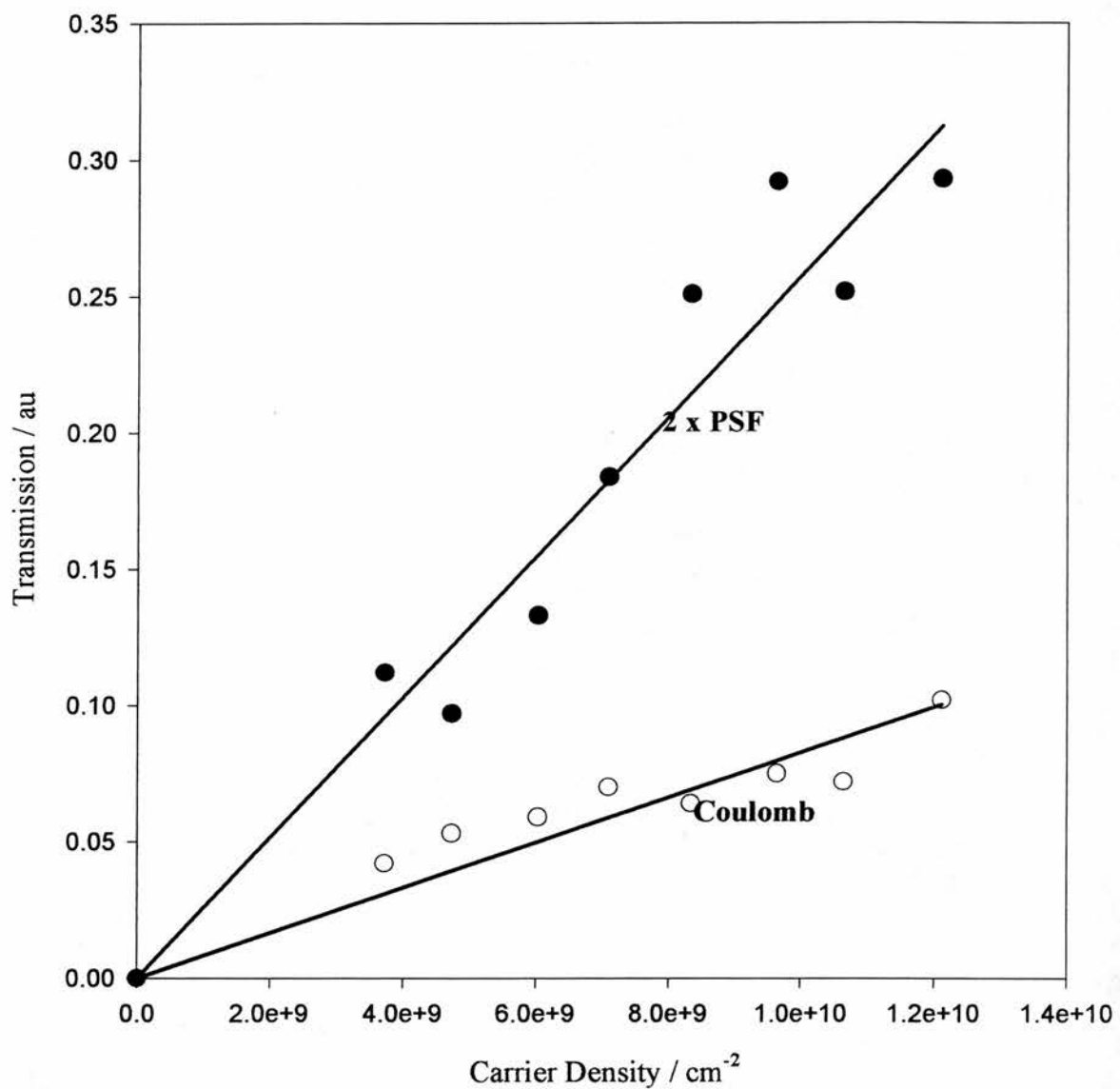


Figure 6.5 Initial change in transmission at the heavy hole exciton resonance as a function of carrier density for sample MR610.

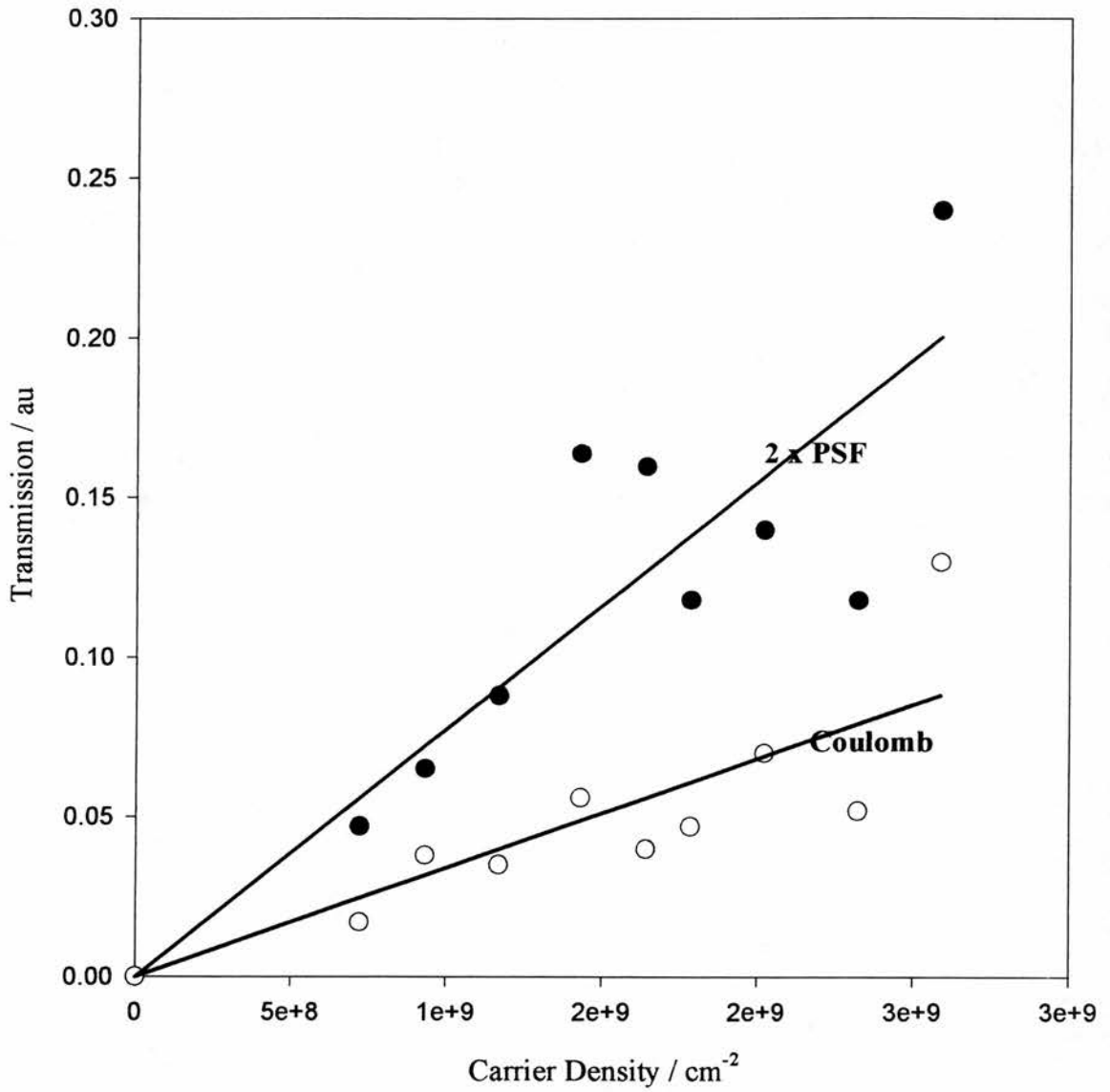


Figure 6.6 Initial change in transmission at the heavy hole exciton resonance as a function of carrier density for sample MR611.

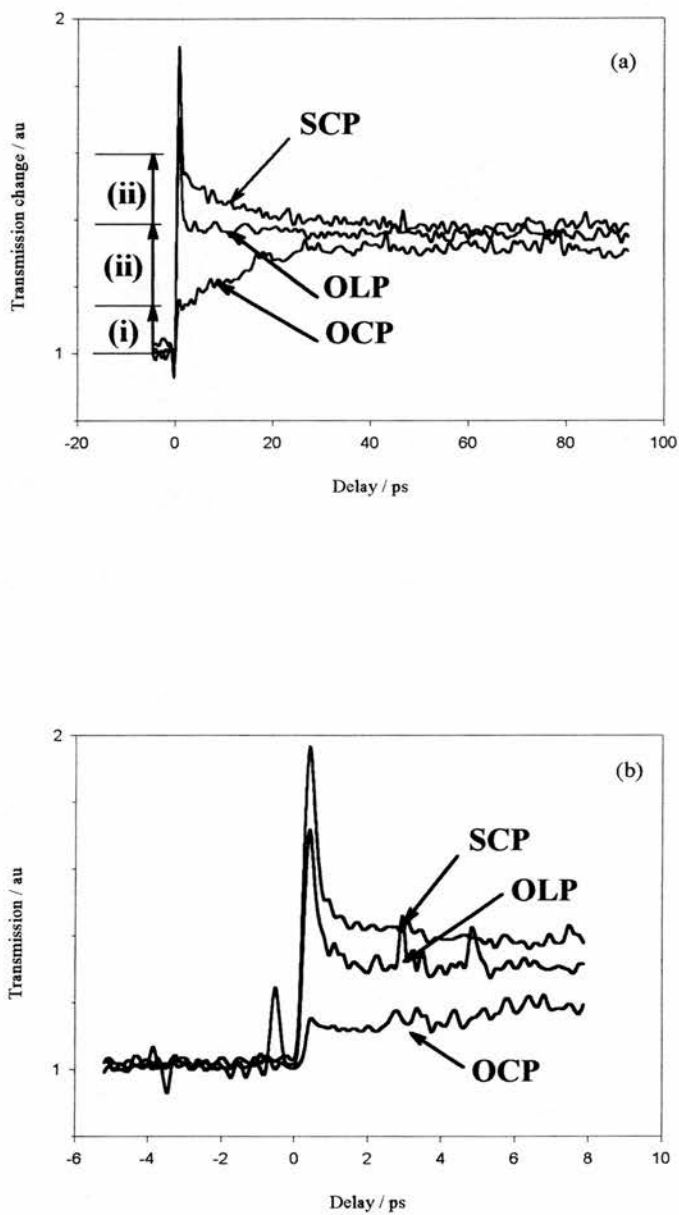


Figure 6.7 Typical (a) long and (b) short range pump-probe traces for the sample MR535 showing the effect of (i) Coulomb effects and (ii) phase space filling.

6.5 Data Analysis

The first thing that is apparent from figure 6.3 is that there is very little absorption change in the absence of PSF, as observed from the initial steps in the OCP traces. For these results, the step size in the delay is too large for exciton-exciton effects to be resolved, because the exciton ionises within 250 fs. The transmission change in each trace can therefore be attributed to the electron-hole plasma created from the ionisation of excitons. In the OCP case, the initial small increase in the transmission occurs solely due to the Coulombic effects of screening and lineshape broadening. In the SCP case there is a further increase in transmission, which is solely due to the spin dependent phase space filling. These results were mirrored in the other two samples used in this experiment.

From figures 6.4, 6.5 and 6.6 it can be seen that both the Coulomb and the PSF contributions to the exciton saturation vary linearly with pump power (carrier density). This is in contrast to the results of Cameron [6.6], who carried out a similar study in GaAs MQWs. In that study, the PSF was found to vary linearly with carrier density, but the Coulomb contribution was found to vary non-linearly in narrow well samples. This non-linear variation was attributed to collisional broadening. The linear variation of the Coulomb contribution with pump power in this experiment suggests that the probe experiences no change due to linewidth broadening in these samples and the small spin-independent contribution is due to Coulomb screening. A comparison of the traces in figure 6.2 shows that there is no significant difference in the size of the Coulomb effect whether the experiment is carried out with 150fs pulses or 650fs pulses. This is in contrast to the results of Holden [6.7]. The 650fs pulses have a spectral bandwidth much less than the heavy hole exciton linewidth and therefore the transmission change experienced by these pulses is due to the combined effects of screening, broadening and

PSF, which all reduce the absorption at line centre. However, the bandwidth of the 150fs pulses is greater than the heavy hole exciton linewidth. Consequently, in this case the probe measures the integrated absorption change, thus examining screening and PSF only. The effects of screening, broadening and PSF on a simple resonance are shown in figure 6.8. The similarity in the size of the Coulomb effect in the sets of traces measured for excitation with both 150fs and 650fs pulses supports the conclusion that collisional broadening is of little significance in these samples.

Further evidence for the absence, or not, of any broadening can be seen by examining the long wavelength side of the exciton resonance. It can be seen from figure 6.8 that broadening should cause an increase in the absorption in the wings of the exciton resonance, while Coulomb screening and PSF do not. Any broadening should therefore show up as a reduction of the transmission on the long wavelength side of the exciton resonance. It can be seen in figure 6.9 that, even though the results are rather noisy, there is no such reduction for sample MR535. The other samples all show similar results, thus confirming the insignificance of broadening to the exciton saturation in these samples at room temperature.

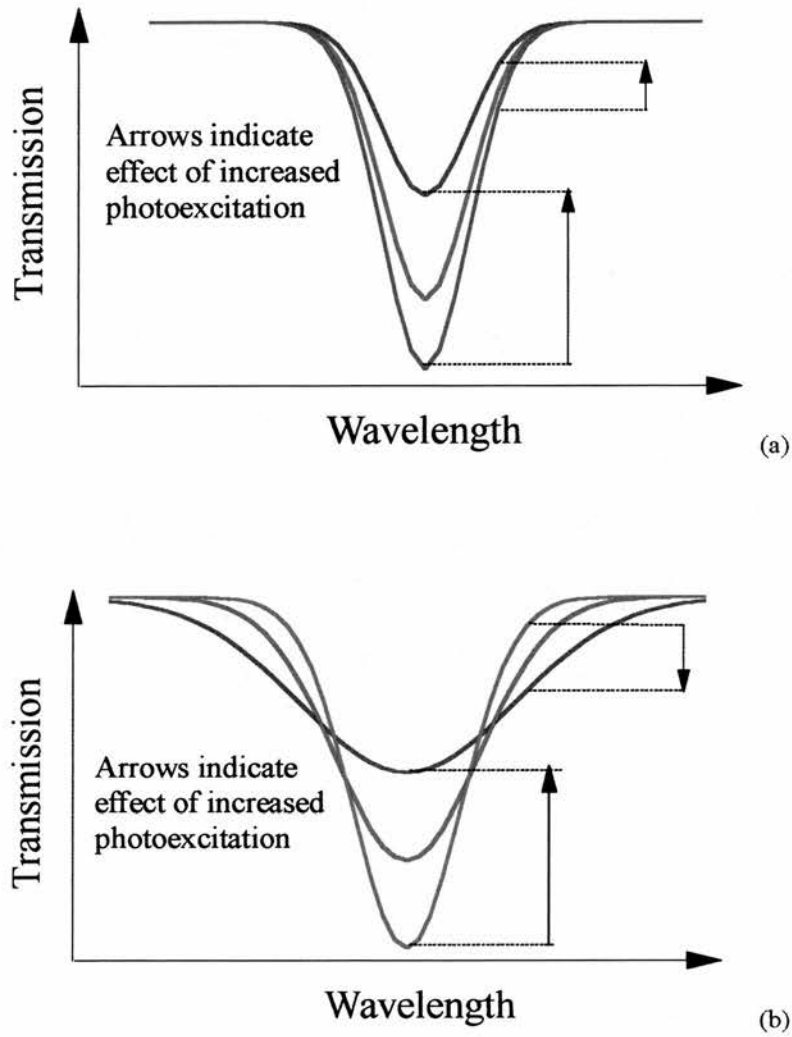


Figure 6.8 The effect of (a) screening and phase space filling and (b) broadening on a simple resonance.

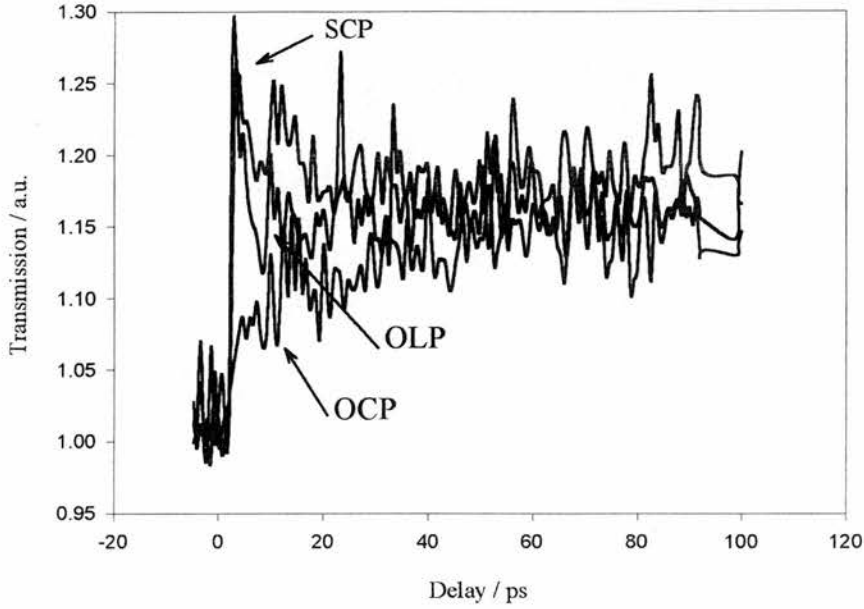


Figure 6.9 Change in transmission for sample MR535 on the long wavelength side of the heavy hole exciton ($1.53\mu\text{m}$) as a function of probe pulse delay time.

6.5.1 Exciton-exciton saturation

The high temporal resolution traces shown in figure 6.6(b) and figure 6.10 allow the observation of exciton-exciton saturation. It can be seen that while both the OLP and SCP results show an initial sharp rise in transmission that relaxes within approximately 250fs, this feature is absent from the OCP traces. This transient exciton saturation is due to exciton-exciton saturation effects and recovers with the exciton ionisation time, which is approximately 250fs at room temperature.

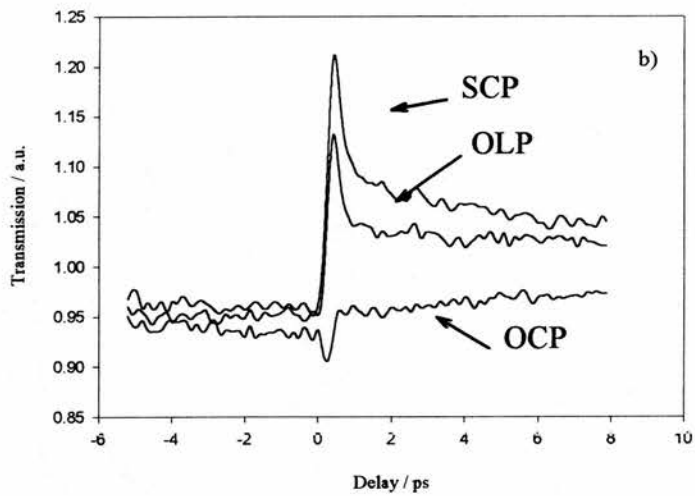
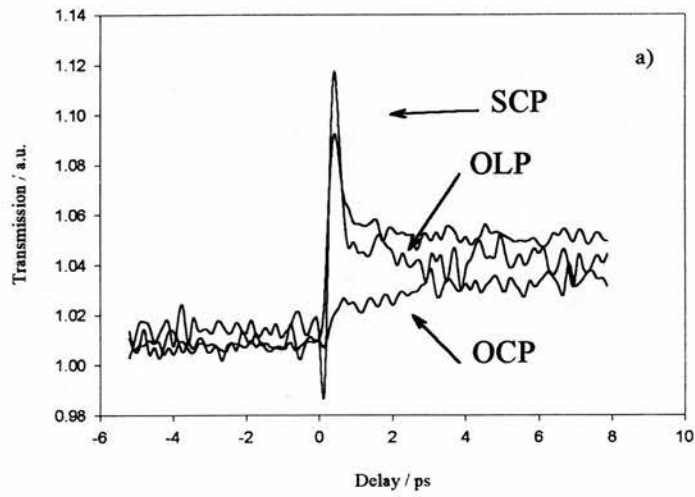


Figure 6.10 High temporal resolution pump-probe traces for the samples (a) MR610 and (b) MR611.

As there is little contribution from PSF to the initial OCP transmission change, the absence of an exciton ionisation feature suggests that the Coulomb screening effect is of similar magnitude for both excitons and free carriers.

The exciton ionisation time and excite pulse duration are comparable, meaning that some exciton ionisation will occur during excitation. Therefore the initial transmission change will include contributions from both free carriers and excitons. This must be accounted for in order to accurately resolve the exciton and free carrier contributions to the saturation. Holden and Mazilu [6.7] developed a rate equation model to describe this situation in GaAs quantum wells. This model was also used in this work to describe the evolution of the different number densities in each energy level both during and after excitation. The model was fitted to the pump-probe traces assuming that the size of each saturation contribution increased linearly with the number density of the responsible particle set. The fitting procedure will now be described in more detail.

The optical system is approximated to a five level system as shown in figure 6.11. The parameters in the figure are defined as follows, ex and FC denote exciton and free carrier energy levels, the left and right hand side are the spin up and spin down levels respectively, Γ_{s1} and Γ_{s2} are the spin relaxation coefficients for the excitons and free carriers respectively and $G^+(t)$ and $G^-(t)$ are the excitation functions for the spin up and spin down levels respectively. The transition coefficients Γ_i are defined as

$$\Gamma_i = \frac{1}{\tau_i} \quad (6.1)$$

where τ_i is the time constant for the transition. Γ_3 represents the exciton ionisation time and Γ_1 and Γ_2 represent the time constants for the electron and exciton recombination respectively.

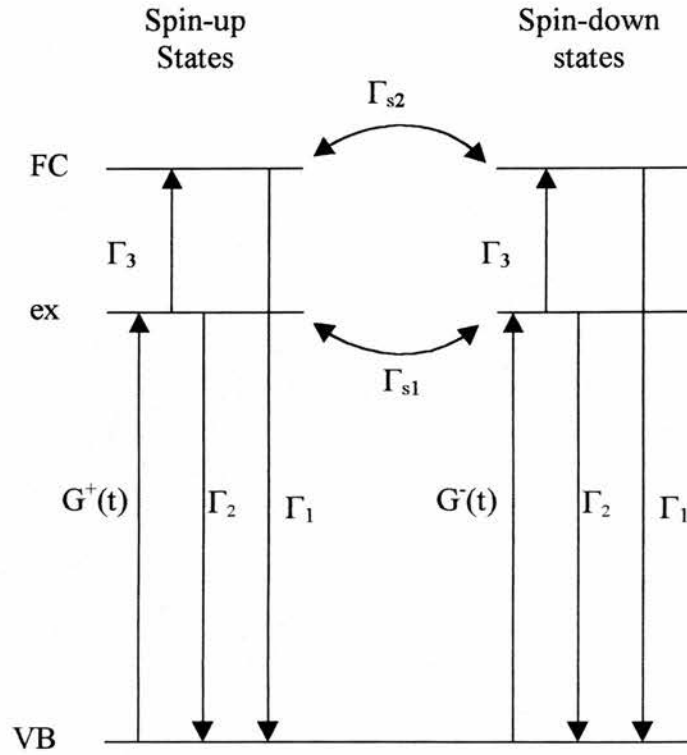


Figure 6.11 Schematic of the five level system used to fit the data.

The population evolution in each level of the system can be represented by a differential rate equation of the form

$$\frac{dn_i}{dt} = G_{ij}(t) + \sum_j \Gamma_{ij} n_j \quad (6.2)$$

where n_i is the population of the level i , j denotes all other levels and $G_{ij}(t)$ is the excitation function between two levels and is only non zero if the transition is in resonance with the excitation. The system of equations can be written in matrix form as

$$\dot{\underline{N}} = \underline{\Gamma} \underline{N} + \underline{f} \underline{G} \quad (6.3)$$

which becomes

$$\begin{pmatrix} \dot{n}_{ex}^+ \\ \dot{n}_{ex}^- \\ \dot{n}_{FC}^+ \\ \dot{n}_{FC}^- \end{pmatrix} = \begin{pmatrix} -\Gamma_2 - \Gamma_3 - \Gamma_{s1} & \Gamma_{s1} & 0 & 0 \\ \Gamma_{s1} & -\Gamma_2 - \Gamma_3 - \Gamma_{s1} & 0 & 0 \\ \Gamma_3 & 0 & -\Gamma_1 - \Gamma_{s2} & \Gamma_{s2} \\ 0 & \Gamma_3 & \Gamma_{s2} & -\Gamma_{s2} - \Gamma_1 \end{pmatrix} \begin{pmatrix} n_{ex}^+ \\ n_{ex}^- \\ n_{FC}^+ \\ n_{FC}^- \end{pmatrix} + \begin{pmatrix} G^+(t) \\ G^-(t) \\ 0 \\ 0 \end{pmatrix} \quad (6.4)$$

when written explicitly for the five level system. The fitting is simplified if the variables are changed to the sum and difference of the particles in each spin state for each energy level. Hence the variables are now

$$\begin{aligned} s_1 &= n_{ex}^+ + n_{ex}^- \\ s_2 &= n_{FC}^+ + n_{FC}^- \\ d_1 &= n_{ex}^+ - n_{ex}^- \\ d_2 &= n_{FC}^+ - n_{FC}^- \end{aligned} \quad (6.5)$$

and are found to obey their own pair of differential equations, given by

$$\dot{\underline{s}} = \begin{pmatrix} -\Gamma_2 - \Gamma_3 & 0 \\ \Gamma_3 & -\Gamma_1 \end{pmatrix} \underline{s} + \begin{pmatrix} G^+(t) + G^-(t) \\ 0 \end{pmatrix} \quad (6.6)$$

$$\dot{\underline{d}} = \begin{pmatrix} -\Gamma_2 - \Gamma_3 - 2\Gamma_{s1} & 0 \\ \Gamma_3 & -\Gamma_1 - 2\Gamma_{s2} \end{pmatrix} \underline{d} + \begin{pmatrix} G^+(t) - G^-(t) \\ 0 \end{pmatrix}. \quad (6.7)$$

Now consider a three level system such as that shown in figure 6.12.

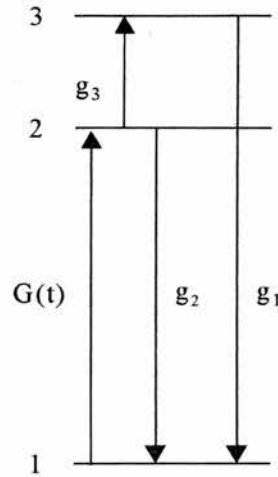


Figure 6.12 Schematic of a three level system.

The populations of the levels in this system are given by

$$\dot{\underline{n}} = \begin{pmatrix} -g_3 - g_2 & 0 \\ g_3 & -g_1 \end{pmatrix} \underline{n} + \begin{pmatrix} G(t) \\ 0 \end{pmatrix}. \quad (6.8)$$

It is evident that the s and d system of equations are equivalent to those governing a three level system. Hence, the original five level system has now been separated into two manageable three level systems. Once the evolution of the populations in each energy level is known a fit to the data can be made.

For the OLP condition there is no spin polarisation of the excited population. Therefore the change in transmission, ΔT , can be deduced from the instantaneous total population of the exciton and free carrier energy levels, s_1 and s_2 . The SCP and OCP conditions both excite the same number of carriers, so the difference between the two traces is due to the polarisations of the carriers. The values d_1 and d_2 are a measure of the polarisations of the excitons and free carriers respectively.

The linearly polarised light used in the OLP case can be treated as a combination of two opposite circularly polarised beams. Therefore $G^+(t)=G^-(t)$ and the excitation function, assuming an excite pulse with a Gaussian temporal profile, is given by

$$G^+(t) + G^-(t) = g_0 \exp\left(-\frac{t^2}{2t_0^2}\right). \quad (6.9)$$

When exciting with circularly polarised light, the total excitation function is given by

$$G^+(t) = g_0 \exp\left(-\frac{t^2}{2t_0^2}\right) \quad (6.10)$$

The solution to equation 6.2 can be obtained more readily by the use of some simplifications. Firstly, the recombination times for both excitons and free carriers are set to be equal ($\Gamma_1=\Gamma_2$). Carrier recombination times have been determined in chapter 5 and are much longer than the total delay of the curves being fitted, so their effects can be ignored. Secondly, the spin relaxation times of both the excitons and electrons are assumed equal ($\Gamma_{s1}=\Gamma_{s2}=\Gamma_s$). Assuming that the exciton spin relaxation time is longer than the ionisation time then the spin relaxation of the carriers will be dominated by free carrier spin relaxation mechanisms.

Using these simplifications and assuming an initial condition of $n_i=0$ at $t=-\infty$, the solutions of equations 6.6 and 6.7 are given by

$$\begin{aligned} s_1 &= g_0 K(\Gamma_1 + \Gamma_3) \\ s_2 &= g_0 (K\Gamma_1 - K[\Gamma_1 + \Gamma_3]) \\ d_1 &= g_0 K(\Gamma_1 + \Gamma_3 + 2\Gamma_s) \\ d_2 &= g_0 (K[\Gamma_1 + 2\Gamma_s] - K[\Gamma_1 + \Gamma_3 + 2\Gamma_s]) \end{aligned} \quad (6.11)$$

where

$$K(\Gamma, t) = \sqrt{\frac{\pi}{2}} t_0 \exp\left(-\Gamma t + \frac{\Gamma^2 t_0^2}{2}\right) \left(1 + \operatorname{erf}\left[\frac{t - \Gamma t_0^2}{\sqrt{2} t_0}\right]\right) \quad (6.12)$$

The fitting was carried out using Mathematica and allowed two curves to be fitted simultaneously, with parameters shared between the two sets of data. The long and short-range traces for each condition were combined to give one complete set of data for each polarisation trace. The OLP and SCP transmission changes were chosen for the fit and each trace was fitted to

$$\Delta T = a_1 s_1 + a_2 s_2 + a_3 d_1 + a_4 d_2 \quad (6.13)$$

The fitting program sets a_3 and a_4 to zero for the OLP fit because the excited populations are unpolarised. For the SCP case a_3 and a_4 are allowed to vary and all other fitting variables are shared between the two traces. Due to the large amount of computation involved, curves were fitted to only two samples, MR535 and MR610. These samples were chosen to allow a comparison between samples with both InGaAsP and InGaAs well material. The fit curves for each sample studied are shown in figures 6.12 and 6.13 and the fitting parameters are summarised in table 6.1.

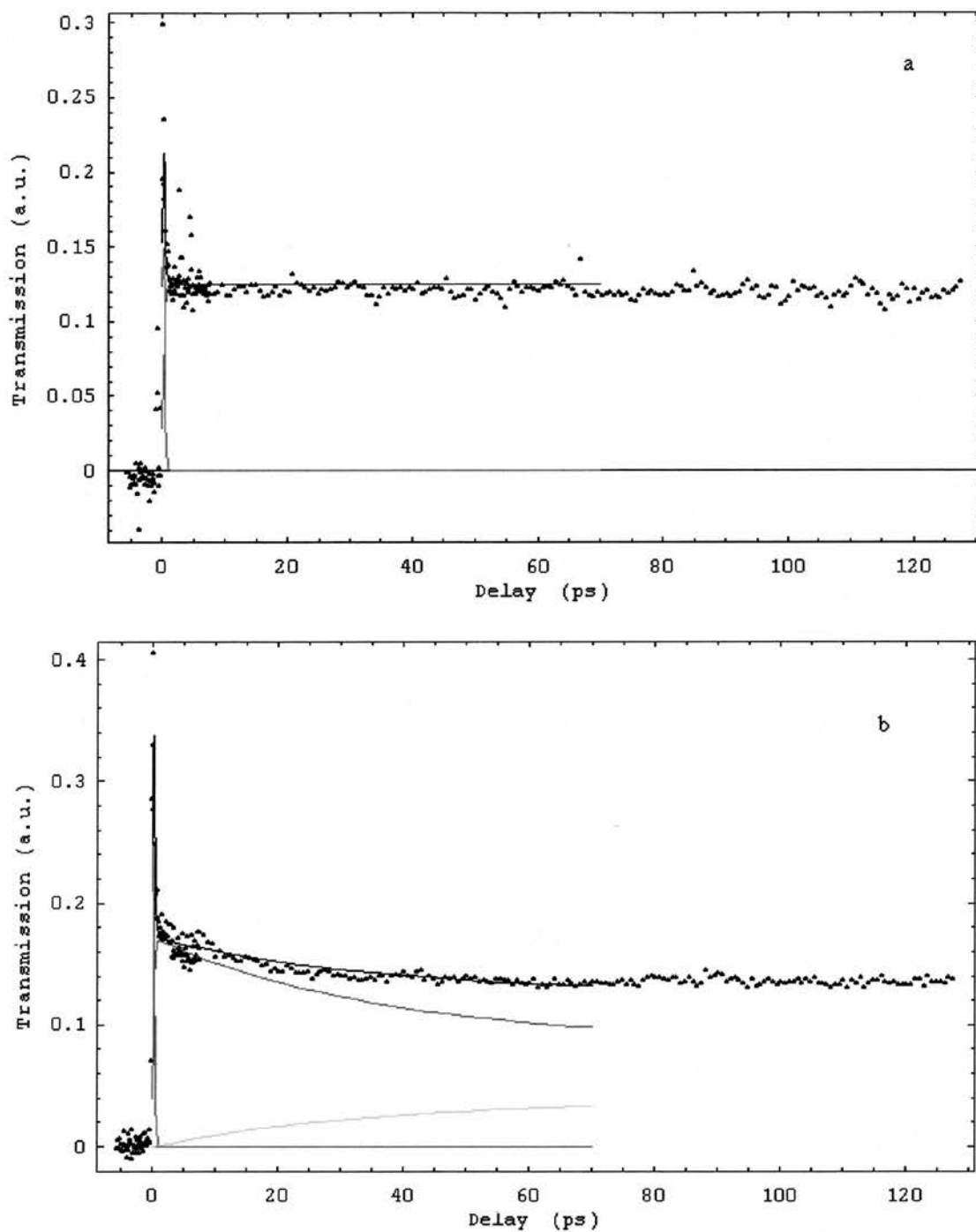


Figure 6.12 Pump-probe traces and fits for sample MR535, showing the data from a) OLP traces and b) SCP traces.

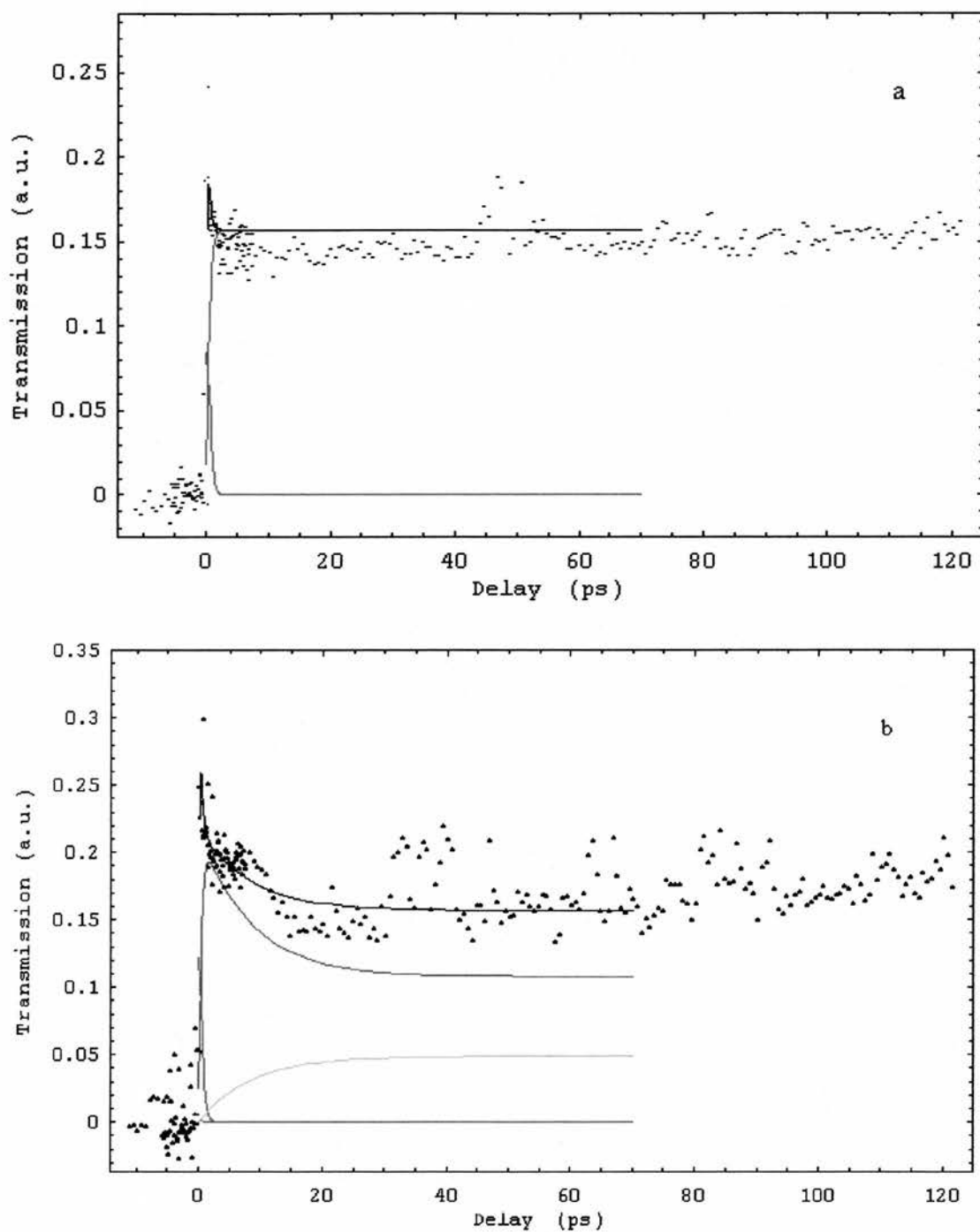


Figure 6.13 Pump-probe traces and fits for sample MR610, showing the data from a) OLP traces and b) SCP traces.

| | MR535 | MR610 |
|-------|------------------|------------------|
| a_1 | 1.53 ± 0.015 | 0.74 ± 0.007 |
| a_2 | 0.42 ± 0.004 | 0.52 ± 0.005 |
| a_3 | 1.05 ± 0.01 | 0.33 ± 0.003 |
| a_4 | 0.16 ± 0.002 | 0.20 ± 0.002 |

Table 6.1 *Fit parameters for the data from each sample.*

The relative strengths of the saturation induced by the excitons and free carriers can be deduced from the ‘a’ coefficients. Substituting the definitions of s and d back into the fit equation and collecting the coefficients for each particle set gives

$$\Delta T = (a_1 + a_3)n_{ex}^+ + (a_1 - a_3)n_{ex}^- + (a_2 + a_4)n_{FC}^+ + (a_2 - a_4)n_{FC}^- \quad (6.14)$$

The coefficients of each particle set can be taken as a measure of their respective contributions to the heavy hole exciton saturation. For conditions involving circular polarisations the ‘+’ superscript denotes particle sets of the same spin as those excited by the pump pulse, while the ‘-’ superscript denotes particles of the opposite spin. The opposite spin excitons and free carriers can only saturate the heavy hole exciton resonance through Coulomb effects. Therefore the coefficients of these particle states give a measure of the Coulomb screening only. Same spin particles exhibit not only the same screening mechanisms, but also the PSF effects. Thus, a measure of the PSF contribution to the heavy hole exciton saturation can be obtained by subtracting the coefficients of the opposite spin particles from the coefficients of the same spin particles. The contributions to

the heavy hole exciton saturation of all the effects, normalised to the effect of free carrier screening, are summarised in table 6.2.

| | MR535 | MR610 |
|--------------|-------|-------|
| FC Screening | 1 | 1 |
| FC PSF | 1.2 | 1.2 |
| Ex Screening | 1.8 | 1.2 |
| Ex PSF | 8.0 | 2.0 |

Table 6.2 *Relative contributions to the heavy hole exciton saturation in the samples studied.*

The coloured lines on the graphs in figures 6.12 and 6.13 denote the populations of the various electron states during the relaxation process. In the OLP traces, the red line denotes the exciton population, while the green line denotes the electron population. It can be seen in these traces that the population of electrons grows as the excitons ionise into free carriers. In the SCP traces, the red line denotes the spin up (down) exciton population while the green line represents the spin down (up) exciton population, clearly showing that the excitons ionise before the carrier spins begin to randomise. The blue line, however, denotes the electron spin up (down) population, which can be seen to reduce as the spin down (up) electron population denoted by the yellow line grows.

6.6 Discussion

Any collisional broadening seems to be masked by the effects of both inhomogeneous broadening and Coulomb screening in the samples studied. The previous study of broadening in GaAs by Cameron [6.6] showed little effect of broadening in all but the sample with the narrowest well width (4.4nm), which had an exciton linewidth of 6 meV. The sample with the narrowest well width in this study (MR611, 5.5nm) shows no signs of broadening, although it should be noted that this well width is larger than the narrowest well studied by Cameron, and has a significantly inhomogeneously broadened exciton linewidth of 27 meV. Cameron suggested that broadening became apparent in narrow quantum wells because the efficiency of the free carrier plasma screening was reduced in narrow wells, thus reducing the Coulomb potential and allowing the broadening to be observed as Coulomb screening became less significant. Cameron also suggested that broadening was more easily observed in high quality samples, with large exciton binding energies.

Hunsche [6.8] separated the effects of broadening from exciton saturation using a technique employing a white light continuum probe. The reduction of oscillator strength (ROS) was measured for the $n=1$ light and heavy hole excitons and the $n=2$ heavy hole exciton by integrating the absorption change over the resonances. The pump was tuned such that no carriers were excited to the $n=2$ conduction band, implying that any changes to the $n=2$ exciton were due to Coulomb effects alone. Knox et. al. [6.1] have also used the change in transmission at the $n=2$ exciton resonance as a measure of Coulomb effects in a similar experiment. In this case the effect of free carrier screening was found to be six times smaller than the effect of PSF.

In this study, the effect of broadening appears to be negligible and is excluded from the 150fs traces due to the large bandwidth of these pulses. Hence the Coulomb contribution in these traces can be attributed to screening alone, allowing comparisons of the saturation mechanisms.

The fits to the data show that the spin independent contribution to the exciton saturation from excitons is of the order of that from free carriers, supporting the hypothesis that the spin independent screening is the same for both excitons and free carriers. It can also be seen that both the screening contributions and the contribution to PSF from free carriers are of similar order. The largest overall contribution to the initial exciton saturation is PSF caused by the presence of excitons. It should be noted that in Sample MR535, which has a quaternary quantum well material, the PSF is approximately eight times as strong as the screening. In sample MR610 however, where the quantum well material is a ternary alloy, the PSF is only twice as strong as the screening contribution. The reasons for this are unclear, but it is conjectured that the difference in the size of the PSF contributions may be due to the presence of strain in sample MR610. Further studies will be necessary to resolve this issue.

Free carrier screening has been predicted to be dependent on the plasma temperature and is therefore dependent on the excitation wavelength. However, room temperature excitons are always created near $k=0$ and ionise, rather than thermalising with the lattice, hence they only contribute to screening when cold. Such different temperature dependencies of the screening efficiencies of each particle set are a powerful argument against the spin independent contributions to the exciton saturation being equal.

Experimental studies [6.8] have shown that the reduction in oscillator strength of the exciton resonance is unaffected by the cooling of free carriers, suggesting that screening is not plasma temperature dependent. Studies of temperature dependence in

both GaAs and InGaAs(P) are still required to help resolve the conflict between experiment and theory.

6.7 Conclusions

The experiments in this chapter have made use of a simple method to fully separate the effects of screening, broadening and phase space filling on exciton saturation at room temperature. Surprisingly, it was found that broadening had little significance in the samples studied, which is attributed to sample dependent inhomogeneous broadening masking any collisional broadening effects. The contributions to the Coulomb screening by both excitons and free carriers was determined, and found to be approximately equal. Further studies will be necessary to help formulate an accurate theory to describe the mechanisms of exciton saturation.

6.8 References

- 6.1 W.H. Knox, C. Hirlimann, D.A.B. Miller, J. Shah, D.S. Chemla and C.V. Shank, "Femtosecond excitation of nonthermal carrier populations in GaAs quantum wells", *Phys. Rev. Letts.*, **56**, 11, 1191-1193, (1986).
- 6.2 S. Schmitt-Rink, D.S. Chemla and D.A.B. Miller, "Theory of transient excitonic optical nonlinearities in semiconductor quantum-well structures", *Phys. Rev. B.*, **32**, 6601-6609, (1985).
- 6.3 J.B. Stark, W.H. Knox and D.S. Chemla, "Femtosecond circular dichroism study of nonthermal carrier distributions in two- and zero-dimensional semiconductors", *Phys. Rev. Letts.*, **68**, 3080-3083, (1992).
- 6.4 S. Bar-Ad, and I. Bar-Joseph, "Exciton spin dynamics in Ga As heterostructures", *Phys. Rev. Letts.*, **68**, 349-352, (1992).
- 6.5 M.J. Snelling, P. Perozzo, D.C. Hutchings, I. Galbraith and A. Miller, "Investigation of excitonic saturation by time-resolved circular dichroism in GaAs-Al_xGa_{1-x}As multiple quantum wells", *Phys. Rev. B*, **49**, 17160-17171, (1994).
- 6.6 A.R. Cameron, "Ph.D. Thesis", University of St. Andrews, (1996)
- 6.7 T.M. Holden, "Ph.D. Thesis", University of St. Andrews, (1997)
- 6.8 S. Hunsche, K. Leo, H. Kurz, K. Kohler, "Exciton absorption saturation by phase space filling: Influence of carrier temperature and density", *Phys. Rev. B*, **49**, 16565-16568, (1994).

Chapter 7 Spin relaxation

7.1 Summary

In this chapter electron spin relaxation in multiple quantum wells is investigated. The electron spin relaxation time in a number of quantum well samples of varying well widths is measured. These results are compared with those previously reported and indications for the determination of the spin relaxation mechanism at room temperature are discussed.

7.2 Introduction

In chapter 6 the spin dependent nature of phase space filling was discussed from the point of view of exciton saturation. In this chapter, the temporal dependence of the phase space filling term is discussed in relation to the time for carrier spins to randomise.

In bulk InGaAs(P) the light and heavy hole transitions are degenerate at $k=0$. In conjunction with the unequal transition probabilities discussed in chapter 2, this allows a maximum induced polarisation of 50%. In quantum wells however this degeneracy is lifted and it becomes possible to obtain 100% polarisation of the excited carriers as discussed in chapter 2. After excitation a spin polarised population of carriers will, over time, relax due to various mechanisms, producing equal numbers of carriers in both the spin up and down states. The mechanisms that cause carrier spins to relax will now be discussed, first for the case of bulk semiconductors and then for the quantum well case.

7.3 Spin relaxation in bulk semiconductors

In bulk semiconductors the hole spins randomise on very short timescales due to the degeneracy of the light and heavy hole bands at $k=0$. This time is essentially the same as the hole momentum relaxation time.

There have been a number of mechanisms proposed to describe the spin relaxation of electrons in bulk semiconductors. The most notable are those of D'Yakonov and Perel (DP), Elliot and Yafet (EY) and Bir, Aharonov and Pikus (BAP). The EY and DP mechanisms derive from band structure effects near the Γ point of the conduction band, while the BAP process is an exchange interaction between electrons and holes. It should be noted that not all the excited carriers are located at the Γ point as thermalisation produces a spread in k -space.

The EY mechanism [7.1, 7.2] is a consequence of mixing of valence band wavefunctions into conduction band states away from $k=0$. This mixing allows electrons to flip spin due to momentum scattering from optical and acoustical phonons or impurities. It has been suggested [7.3] that the EY mechanism contributes to spin relaxation at high temperatures and / or low hole concentrations.

The DP mechanism [7.4, 7.5] results from the spin-orbit splitting of the conduction band in semiconductors without a centre of inversion. In zinc-blende crystals such as InGaAs(P), the splitting is proportional to the cube of the momentum and the contribution to the spin relaxation increases rapidly with electron energy [7.6]. The spin splitting of the conduction band is equivalent to the existence of a magnetic field acting on the electron spins. Between collisions the electron spin precesses about the direction of the pseudo-field, which is defined by the momentum direction. During collisions, changes of the

momentum cause a rotation of the precession axis, allowing the spins to flip. If the time between collisions is less than the precession period then the electron spins are unable to follow the frequent changes of the precession axis, reducing the effect of the spin-orbit splitting and slowing the spin relaxation process. The DP mechanism has been shown experimentally to be dominant for low acceptor impurity concentrations and / or at high temperature [7.7, 7.8].

The BAP mechanism [7.9] is important when excited electrons are surrounded by a high concentration of holes. The increased probability of electron-hole collisions allows the electron and hole spins to interact via the exchange interaction and thus flip the electron spins. The electron spin relaxation time is inversely proportional to the hole momentum scattering time if the holes are strongly scattered by impurities or phonons. This mechanism has been shown to be dominant in heavily p-doped semiconductors and at low temperatures [7.10, 7.11].

A number of investigations have characterised the transition from the DP mechanism to the BAP mechanism in GaAs [7.12, 7.13] and shown them to be the dominant mechanisms for electron spin relaxation.

7.4 Spin relaxation in quantum wells

In spite of numerous studies, the carrier spin dynamics in quantum wells are still not well understood. Problems seem to arise from sample dependent mechanisms that make quantitative comparisons between samples unreliable. It has previously been stated that the degeneracy of the light and heavy hole valence bands at $k=0$ is lifted in a quantum well. Since the spin flip of holes arises from the admixture of light and heavy hole band states it has been suggested that this mechanism will lead to a reduced hole spin relaxation

rate in quantum wells. Several papers have presented theoretical models relating to hole spin relaxation. Ferreira et. al. [7.14] predicted a slow hole spin relaxation caused by alloy and impurity scattering. A much faster hole spin relaxation mechanism arising from scattering from phonons has been proposed by Uenoyama [7.15]. The excited hole energy is generally small compared to the optical phonon energy, thus the most important mechanism would seem to be scattering of holes from acoustic phonons through the deformation potential. It is now established that the hole spin relaxation time is of the order of the momentum relaxation time. Comparison of experimental results with the predictions of theory has proved problematic due to the different scattering processes contributing to hole spin relaxation.

Electron spin relaxation in quantum wells is also poorly understood. Damen et al [7.16] measured a low temperature electron spin relaxation time of 150 ps in a p-doped GaAs quantum well, which was four times shorter than the value obtained in the bulk material. They suggested that the increased exchange interaction that exists in quantum wells was responsible for this and proposed the BAP mechanism as the dominant mechanism at low temperature. At room temperature the DP mechanism has been proposed, as in the case for bulk material [7.17]. The well width dependence of the spin relaxation time in GaAs has been studied at low temperature by Roussignol et. al. [7.18]. Since their first measurement of the electron spin relaxation in GaAs at room temperature using a pump-probe technique [7.19], Tackeuchi et .al. have also investigated the well width dependence of the spin relaxation time at room temperature [7.20]. Both Roussignol and Tackeuchi used samples grown with quantum well widths that varied across the sample to eliminate sample dependent effects in their results. The DP mechanism in quantum wells has been investigated theoretically by D'Yakonov and Kachorovskii [7.21]. In the 2D case the projection of the electron momentum, q , along the

normal to the layer plane is much greater than the momentum, k , in this plane, leading to an increase in the spin-orbit splitting compared to the bulk case. Studies of a number of GaAs sample grown in different laboratories and consisting of a single quantum well width throughout, have recently been carried out by both Perozzo [7.22] and Cameron [7.23]. They measured electron spin relaxation times in the range 30 to 80ps in GaAs samples with well widths covering the range 4 to 9 nm. Based on these results, Cameron suggested that spin relaxation at room temperature is independent of sample quality, as the predominant scattering results from LO phonon collisions rather than impurity or interface interactions. Recently, Tackeuchi et al [7.24] have measured electron spin relaxation times in InGaAs / InP quantum wells at a wavelength of 1.55 μ m. These studies showed a faster spin relaxation time on the order of 5ps, an order of magnitude faster than the electron spin relaxation time in GaAs quantum wells. Tackeuchi takes this as evidence that the EY mechanism becomes effective in InGaAs quantum wells at room temperature [7.25].

7.5 Dynamical description of spin relaxation

When circularly polarised light resonant with the heavy hole exciton is used to excite a quantum well, a population of 100% spin polarised electrons is excited from the valence band into the conduction band. The excited electrons occupy either the spin up or the spin down state, depending on whether the incident light is left or right circularly polarised. Once excited, the electron spins relax to an equilibrium state where the conduction band is populated by equal numbers of spin up and spin down electrons. Assuming that the spins relax exponentially until equilibrium is reached, the processes involved can be described by the following rate equations.

$$\frac{dN^+}{dt} = -\frac{N^+}{r} - \frac{N^+}{s} + \frac{N^-}{s} = -\frac{N^+}{r} - \frac{N^+ - N^-}{s} \quad (7.1)$$

$$\frac{dN^-}{dt} = -\frac{N^-}{r} + \frac{N^+}{s} - \frac{N^-}{s} = -\frac{N^-}{r} + \frac{N^+ - N^-}{s} \quad (7.2)$$

where $N^{+(-)}$ is the population of spin up (down) electrons, r is the relaxation time relating to the recombination of electrons and holes and s is the spin relaxation time.

Adding equations 7.1 and 7.2 gives:

$$\frac{d(N^+ + N^-)}{dt} = -\frac{N^+ + N^-}{r} \quad (7.3)$$

This equation describes the total carrier recombination rate characterised by r . This is observed experimentally when orthogonal linear polarisations are used.

Subtracting equations 7.1 and 7.2 gives:

$$\frac{d(N^+ - N^-)}{dt} = -\left(\frac{1}{r} + \frac{2}{s}\right)(N^+ - N^-) \quad (7.4)$$

Expressions for $(N^+ + N^-)$ and $(N^+ - N^-)$ can now be obtained from equations 7.3 and 7.4. Addition of the resulting equations yields an expression for N^+ which is observed when the excite and probe pulses have the same circular polarisation. The expression for N^+ is given by:

$$N^+(t) = \frac{N_0}{2} e^{-t/\tau} \left(1 + e^{-2t/\tau}\right) \quad (7.5)$$

where N_0 is the initial excited electron population. If the carrier relaxation time r is long compared to the electron spin relaxation time s , then the time for the electron spins to randomise can be readily measured by the technique described below.

7.6 Experimental details

The experimental set-up for the investigation of spin relaxation is shown in figure 3.8. The $\lambda/4$ plates were used to provide the different polarisation configurations and the change in transmission caused by the pump pulse was monitored with a time delayed probe as described in chapter 3.

The three polarisation configurations used were opposite linear polarisation (OLP), same circular polarisation (SCP) and opposite circular polarisation (OCP), as described in chapter 6. In the OLP case, the pump excited equal numbers of spin-up and spin-down electrons. The probe interrogated both spin states and ‘saw’ a reduction in absorption due to the presence of electrons in low lying conduction band states. The population of electrons in this case contained both spin-up and spin-down electrons so no spin relaxation was observed. In the SCP case, the pump pulse selectively populated only one spin state. Therefore, the time-delayed probe ‘saw’ a larger reduction of the absorption compared to the OLP case. As discussed in chapter 6 this occurs because the electrons initially all occupied the same spin state. The absorption recovered over time to the OLP level as the electron spins became mixed between the two states. It is this time for the electron spins to randomise that is termed the spin relaxation time, τ_s . In the OCP case, again only one spin state was populated, but the probe now examined the opposite spin state. Therefore, the probe ‘saw’ an initial decrease in absorption compared to the OLP case. This reduced absorption recovered over time to the same level as the OLP case as the spins relaxed.

7.7 Results

Experiments were carried out in four different samples of varying well width. The samples used were MR535 (9.0nm well width), MR610 (6.5nm well width), MR611 (5.5nm well width) and MR850 (9.5nm well width). In each case, the experiment was carried out for the three polarisation configurations OLP, SCP and OCP, using wavelengths resonant with the heavy hole exciton. The results are shown in figures 7.1-7.4, with the OLP traces omitted for clarity. The measured spin relaxation times, τ_s , are summarised in table 7.1.

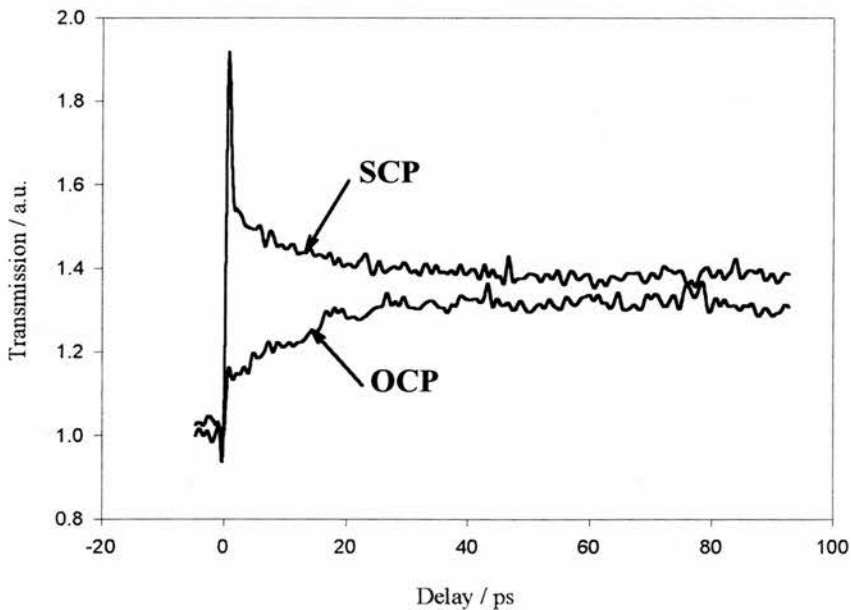


Figure 7.1 Change in transmission of sample MR535 at the heavy hole exciton as a function of probe pulse delay time. The traces correspond to the polarisation configurations used.

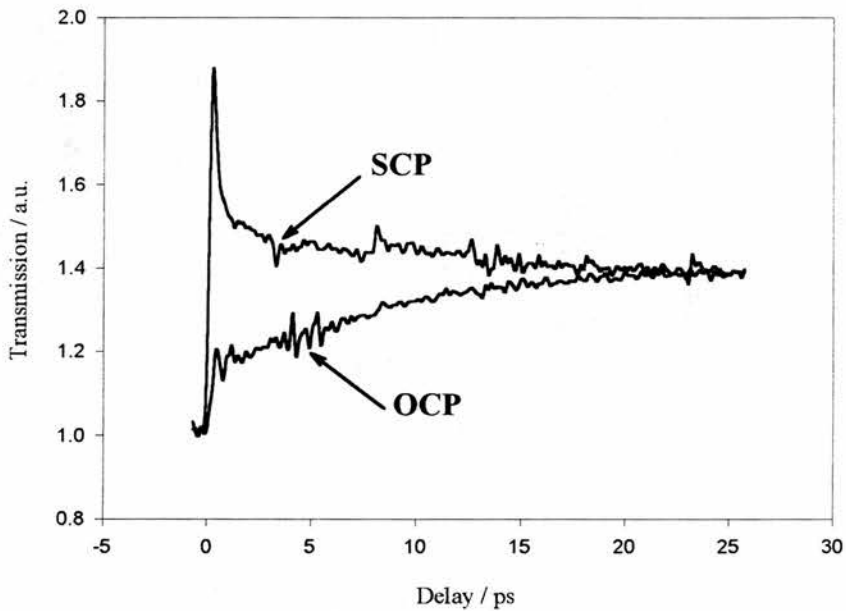


Figure 7.2 Change in transmission of sample MR610 at the heavy hole exciton as a function of probe pulse delay time. The traces correspond to the polarisation configurations used.

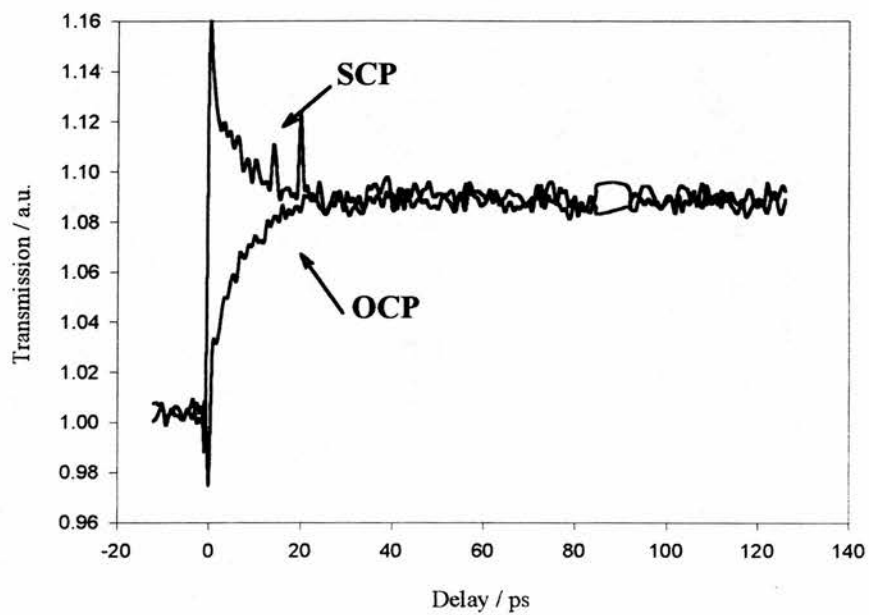


Figure 7.3 Change in transmission of sample MR611 at the heavy hole exciton as a function of probe pulse delay time. The traces correspond to the polarisation configurations used.

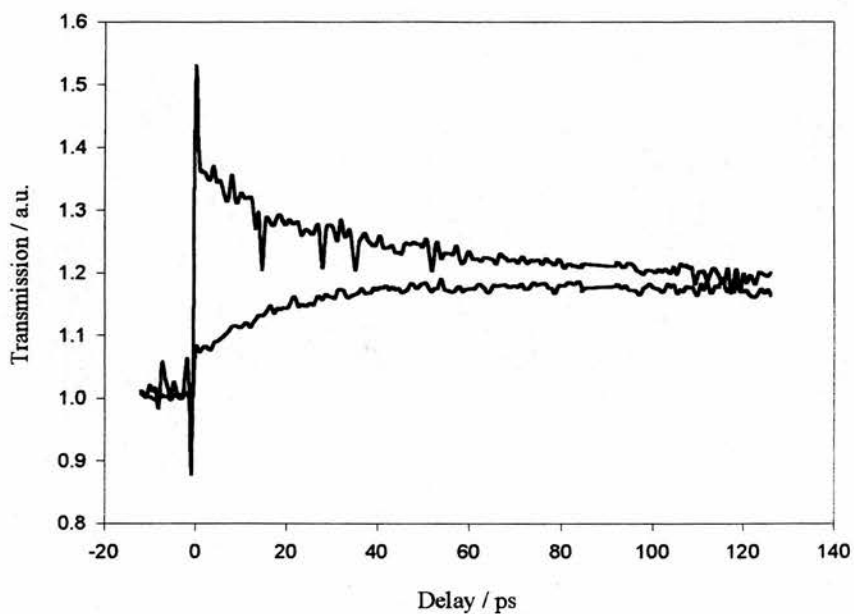


Figure 7.4 Change in transmission of sample MR850 at the heavy hole exciton as a function of probe pulse delay time. The traces correspond to the polarisation configurations used.

| <i>Sample</i> | <i>Well width (nm)</i> | <i>1st eln. confinement energy (eV)</i> | <i>τ_s (ps)</i> |
|---------------|------------------------|--|---------------------------------|
| MR611 | 5.5 | 0.20 | 5.7 |
| MR610 | 6.5 | 0.152 | 7.9 |
| MR535 | 9.0 | 0.082 | 12 |
| MR850 | 9.5 | 0.061 | 20 |

Table 7.1 *Spin relaxation times.*

7.8 Discussion

The DP and BAP mechanisms are considered to be the most important in quantum wells. The DP process is enhanced in quantum wells due to the increased spin orbit splitting of the conduction band, which produces greater local effective magnetic fields, speeding up the precession that causes the electron spin to flip. The enhancement of the BAP is due to the increased electron-hole interaction that exists in quantum wells.

The expression for the enhancement of spin relaxation rate due to the DP mechanism is given by Damen et al [7.16] as,

$$\frac{1}{\tau_{s_{2D}}} = \frac{4}{(k_f L)^4} \frac{1}{\tau_{s_{3D}}} \quad (7.6)$$

where τ_{2D} is the spin relaxation time in a quantum well, τ_{3D} is the spin relaxation time in bulk material, k_f is the Fermi wave vector for the 3D density and L is the well width.

A more complete expression for the enhancement of the DP mechanism in a quantum well is given by [7.26]

$$\frac{1}{\tau_s} = \frac{2(\alpha E_{1e} / \hbar)^2}{E_g k_B T} \int_0^\infty \varepsilon \tau_v(\varepsilon) \exp\left(\frac{-\varepsilon}{k_B T}\right) d\varepsilon \quad (7.7)$$

where α is a numerical coefficient governing the spin splitting of the conduction band. E_{1e} is the first electron confined state in the quantum well, E_g is the band gap and τ_v is the electron momentum relaxation time.

The enhancement of the BAP mechanism for the spin relaxation rate in quantum wells compared to bulk is given by [7.16]

$$\frac{1}{\tau_{s2D}} = \frac{3\pi}{2k_f L} \frac{1}{\tau_{s3D}} \quad (7.8)$$

Both equation 7.7 and 7.8 predict a decrease in the electron spin relaxation rate with decreasing well width, consistent with the experimental results given in table 7.1. For infinite wells E_{1e} is proportional to $1/L^2$, so ignoring any energy dependence of τ_v , equation 7.7 for the DP mechanism gives the approximation,

$$\frac{1}{\tau_s} \propto \frac{1}{L^4} \quad (7.9)$$

which is consistent with equation 7.6. The dependence of the first electron confinement energy on the quantum well width is plotted in figure 7.5, for the case of both finite and infinite quantum wells assuming an electron effective mass, $m^*_e = 0.043m$ and band offset ratio of 40:60 giving an electron well depth of 140 meV. This shows that the L^4 dependence is only true for wide wells where the confinement is small, since E_{1e} depends on well depth and other factors (such as alloy concentration) in addition to well width. The values of E_{1e} were calculated in chapter 4 for each sample. Therefore the variation of τ_s with E_{1e} is the preferred measure and the measured spin relaxation rates, $1/\tau_s$ are plotted versus E_{1e} in figure 7.6.

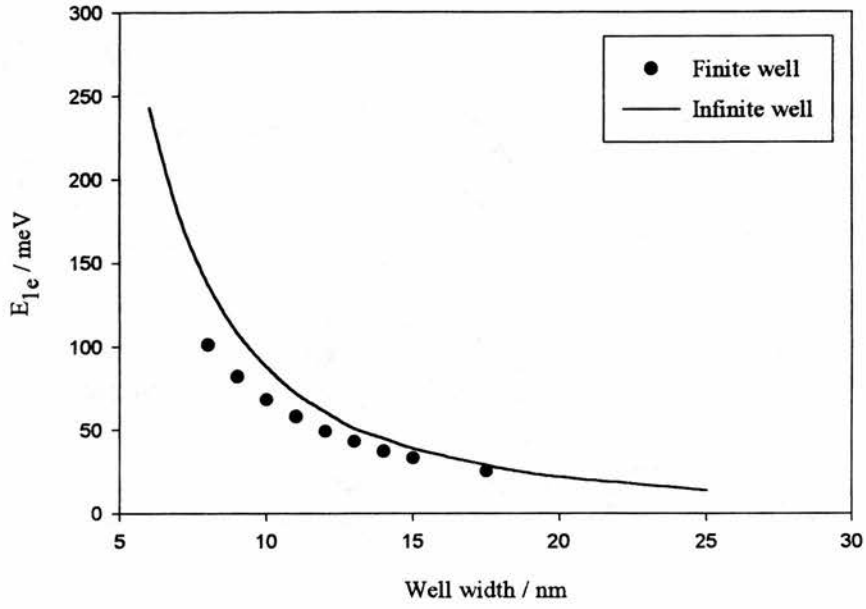


Figure 7.5 Dependence of the first electron confinement energy on well width for infinite and finite quantum well cases.

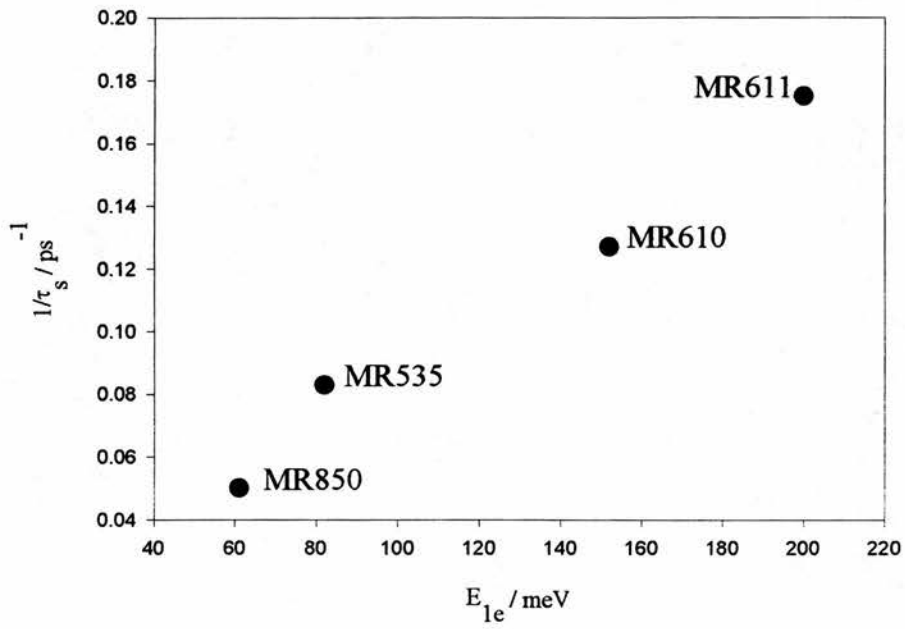


Figure 7.6 Spin relaxation rate as a function of the first electron confinement energy for samples MR535, MR610, MR611 and MR850.

The results for the samples studied in this experiment were all obtained at room temperature and relate to electron spin relaxation. Each of these samples was grown with only one quantum well width, in contrast to the GaAs samples used by Roussignol and Tackeuchi which were grown with different well widths across a single sample.

Similar studies have been carried out by Cameron and Grevatt [7.23] in GaAs. The samples used each had different well widths. They found that the dependence of $1/\tau_s$ on E_{1e} suggested that the DP mechanism was dominant in undoped GaAs quantum wells at room temperature. Given that the spin relaxation times in the InGaAs(P) quantum wells studied in this experiment have been found to depend on quantum well width at room temperature, it seems reasonable to suppose that the DP mechanism will be dominant for this material system also. Further evidence for this conclusion in favour of the DP mechanism is the reciprocal band gap energy dependence for the spin relaxation rate predicted by equation 7.7. The band gap energies of the GaAs quantum wells studied previously are approximately 1.8 times larger than the InGaAs(P) materials investigated here while the spin relaxation rates measured here are twice as fast in samples with similar electron confinement energies.

The Cameron, Grevatt and Tackeuchi results, along with those for MR535, MR610, MR611 and MR850 are shown in figure 7.7. The spin relaxation rates of MR535, MR610, MR611 and MR850 were all scaled by 1.8 to allow direct comparison with the Cameron and Tackeuchi results. Fitting to all the data points using the generic equation $y = \alpha x^b + c$, a value of 1.19 is obtained for b . This is in reasonable agreement with Cameron and Grevatt's calculation and is further evidence that the DP mechanism is the dominant spin relaxation mechanism in InGaAs(P) quantum wells at room temperature.

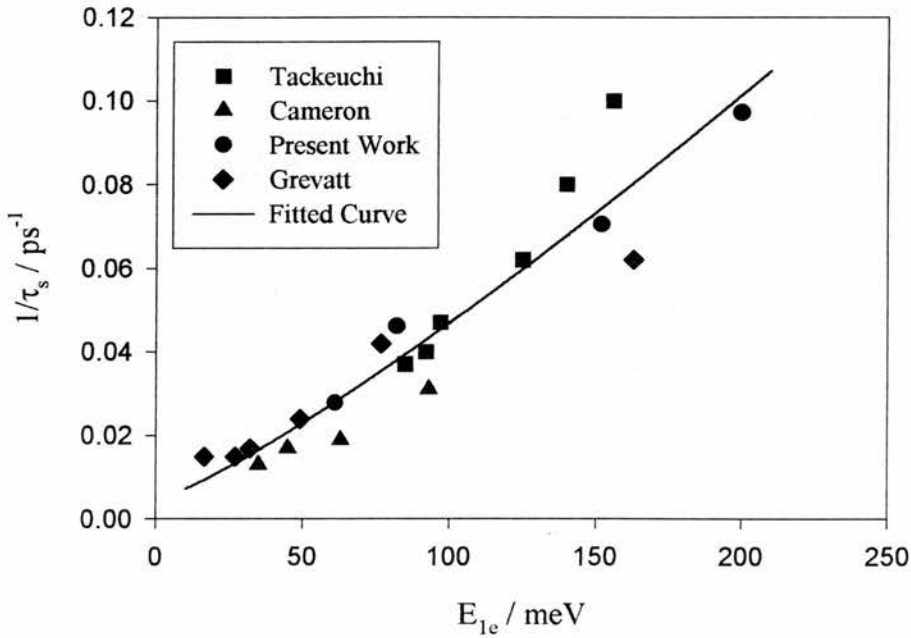


Figure 7.7 Spin relaxation rate as a function of first electron confinement energy for the results obtained by Tackeuchi, Grevatt and Cameron in GaAs MQWs and those for InGaAs(P) MQWs MR535, MR610, MR611 and MR850, scaled by 1.8. The fitted curve $y = ax^b + c$ has $b=1.19$.

7.9 Conclusion

The electron spin relaxation times in a number of InGaAs(P) MQWs have been determined. The times measured were found to be much faster in InGaAs(P) MQWs compared to those previously determined in GaAs MQWs.

The spin relaxation rate has been shown to agree with the predictions of the DP mechanism for the effect of varying quantum well width, and from a comparison of the

bandgap dependence between GaAs and InGaAs(P) MQWs. The results show a decrease in the electron spin relaxation time as the well width is reduced and are in good agreement with the results of both Tackeuchi's, Grevatt's and Cameron's studies of spin relaxation in GaAs, when scaled by the ratio of the bandgap energies. Combining all of the GaAs and InGaAs(P) data gives a 1.19 power dependence of the spin relaxation rate on the electron confinement energy which suggests that the DP mechanism is the dominant mechanism for spin relaxation in both GaAs and InGaAs(P) quantum wells at room temperature. The fact that the data from many samples, not only from different sources, but also of different materials, is all in good agreement with the DP mechanism strongly suggests that the scattering mechanism leading to electron spin relaxation in MQWs at room temperature is phonon scattering, rather than any extrinsic scattering source, such as alloy scattering or scattering from impurities.

The dependence of the spin relaxation time on well width at room temperature is important for device applications. If the dependence on well width is known then samples with specific spin relaxation times can be fabricated. Such utilisation of the spin dependent optical non-linearity is discussed further in the following chapter.

7.11 References

- 7.1 R.J. Elliott, "Theory of effect of spin-orbit coupling on magnetic resonance in some semiconductors", *Phys. Rev.*, **96**, 2, 266-279, (1954).
- 7.2 Y. Yafet, "g factors and spin-lattice relaxation of conduction electrons", *Solid. State. Phys.*, **14**, 1-98, (1963).
- 7.3 A.H. Clark, R.D. Burnham, D.J. Chadi and R.M. White, "Spin relaxation of conduction electrons in GaAs", *Solid. State. Comms.*, **20**, 385-387, (1976).
- 7.4 M.I. D'Yakonov, and V.I. Perel', "Spin orientation of electrons associated with the interband absorption of light in semiconductors", *Sov. Phys. JETP*, **33**, 5, 1053-1059, (1971).
- 7.5 M.I. D'yakonov, and V.I. Perel', "Spin relaxation of conduction electrons in noncentrosymmetric semiconductors", *Sov. Phys. Solid State*, **13**, 12, 3023-3026, (1972).
- 7.6 R.J. Seymour, M.R. Junnarkar and R.R. Alfano, "Spin relaxation of photogenerated degenerate electron distributions in GaAs", *Phys. Rev. B.*, **24**, 6, 3623-3625, (1981).
- 7.7 A.H. Clark, R.D. Burnham, D.J. Chadi and R.M. White, "Spin relaxation of conduction electrons in $\text{Al}(x)\text{Ga}(1-x)\text{As}$ ", *Phys. Rev. B.*, **12**, 12, 5758-5765, (1975).

- 7.8 V.L. Berkovits, A.I. Ekimov and V.I. Safarov, "Optical orientation in a system of electrons and lattice nuclei in semiconductors. Experiment", *Sov. Phys. JETP*, **38**, 1, 169-176, (1974).
- 7.9 G.L. Bir, A.G. Aronov and G.E. Pikus, "Spin relaxation of electrons due to scattering by holes", *Sov. Phys. JETP*, **42**, 4, 705-712, (1976).
- 7.10 G. Fishman, and G. Lampel, "Spin relaxation of photoelectrons in p-type gallium arsenide", *Phys. Rev. B.*, **16**, 2, 820-831, (1977).
- 7.11 R.J. Seymour, and R.R. Alfano, "Time-resolved measurement of the electron-spin relaxation kinetics in GaAs", *Appl. Phys. Letts.*, **37**, 2, 231-233, (1980).
- 7.12 A.G. Aronov, G.E. Pikus and A.N. Titkov, "Spin relaxation of conduction electrons in p-type III-V compounds", *Sov. Phys. JETP*, **57**, 3, 680-687, (1983).
- 7.13 K. Zerrouati, F. Fabre, G. Bacquet, J. Bandet, J. Frandon, G. Lampel and D. Paget, "Spin-lattice relaxation in p-type gallium arsenide single crystals", *Phys. Rev. B.*, **37**, 3, 1334-1341, (1988).
- 7.14 R. Ferreira, and G. Bastard, ""Spin"-flip scattering of holes in semiconductor quantum wells", *Phys. Rev. B.*, **43**, 12, 9687-9691, (1991).
- 7.15 T. Uenoyama, and L.J. Sham, "Hole relaxation and luminescence polarisation in doped and undoped quantum wells", *Phys. Rev. Letts.*, **64**, 25, 3070-3073, (1990).
- 7.16 T.C. Damen, L. Vina, J.E. Cunningham, J. Shah, "Subpicosecond spin relaxation dynamics of excitons and free carriers in GaAs quantum wells", *Phys. Rev. Letts.*, **67**, 24: 3432-3435, (1991).

- 7.17 R.C. Miller, D.A. Kleinman, W.A. Nordland and A.C. Gossard, "Luminescence studies of optically pumped quantum wells in GaAs-Al(x)Ga(1-x)As multilayer structures", *Phys. Rev. B.*, **22**, 2, 863-871, (1980).
- 7.18 P. Roussignol, P. Rolland, R. Ferreira, C. Delalande, G. Bastard, A. Vinattieri, L. Carraresi, M. Colocci. "Time-resolved spin-polarisation spectroscopy in GaAs/AlGaAs quantum wells", *Surface Science*, **267**, 360-364, (1992).
- 7.19 A. Tackeuchi, S. Muto, T. Inata, T. Fujii. "Direct observation of picosecond spin relaxation of excitons in GaAs / AlGaAs quantum wells using spin-dependent optical nonlinearity", *Appl. Phys. Letts*, **56**, 22, 2213-2215, (1990).
- 7.20 A. Tackeuchi, Y. Nishikawa, O. Wada. "Room-temperature electron spin dynamics in GaAs / AlGaAs quantum wells", *Appl. Phys. Letts*, **68**, 6, 797-799, (1996).
- 7.21 M.I. D'yakonov, and V.Y. Kachorovskii, "Spin relaxation of two-dimensional electrons in noncentrosymmetric semiconductors", *Sov. Phys. Semicond.*, **20**, 1, 110-112, (1986).
- 7.22 M.T. Perozzo, "Ph.D. Thesis", University of Central Florida, (1995).
- 7.23 R.S. Britton, T. Grevatt, A. Malinowski, R.T. Harley, P. Perozzo, A.R. Cameron, A. Miller "Room temperature spin relaxation in GaAs/AlGaAs multiple quantum wells", *Appl. Phys. Letts.*, to be published, October 10th 1998.
- 7.24 A. Tackeuchi, O. Wada, Y. Nishikawa. "Electron spin relaxation in InGaAs / InP multiple-quantum wells", *Appl. Phys. Letts*, **70**, 9, 1131-1133, (1997).

- 7.25 A. Tackeuchi, O. Wada. "Electron spin relaxation dynamics in InGaAs / InP multiple quantum wells", *Jpn. J. Appl. Phys*, **37**, 98-99, (1998).
- 7.26 G. Bastard, R. Ferreira, "Spin-flip scattering times in semiconductor quantum wells", *Surface Science*, **267**, 335-341, (1992).

Chapter 8 Optical switching

8.1 Summary

In this chapter all optical switching is examined. Experiments that demonstrate all optical polarisation switching, making use of the spin dependent refractive index optical non-linearity associated with exciton saturation, are presented. A theoretical model to determine the optimum conditions for switching is presented and discussed.

8.2 Introduction

In the previous chapters the spin dependent optical non-linearity was examined and the electron spin relaxation time in a number of samples determined. In this chapter the spin dependent non-linearity is exploited to achieve a polarisation rotation switch, controlled by optical pulses.

Future communications systems are expected to deal with bit rates in excess of several tens of Gbits/s. Soliton switches are required with recovery times on the order of 10 ps and high contrast at room temperature. Semiconductor devices exploiting bandgap resonant saturable absorption effects can achieve switch-on within 1ps, but switch-off generally exceeds 1ns, determined by the carrier lifetime. Many effects have been examined to obtain switching in the picosecond regime.

Four wave mixing in semiconductor laser amplifiers [8.1] has been investigated by many researchers. This effect utilises wavelength conversion and is intended to be used in

wavelength division multiplexing (WDM) systems. However, the wavelength conversion occurs whenever a signal is fed into the device, which could cause problems in practical applications. The optical Stark effect has also been investigated for ultrafast switching applications [8.2]. A multiple quantum well has been shown to switch within 1ps using this effect, but full switch-off at room temperature is disturbed by carrier excitation associated with two-photon absorption [8.3]. Alternatively, non-resonant half-bandgap nonlinearities can be used in switching, eliminating any thermal or carrier lifetime effects [8.4, 8.5]. Again, such devices are affected by two-photon absorption.

Sagnac [8.6], Mach-Zehnder [8.7] and Fabry-Perot interferometer configurations have also been employed together with saturable absorbers. In both Sagnac and Mach-Zehnder configurations, input pulses are split into two paths and a subtraction of the output of the two paths at the end of the configuration is taken as the output of the device. If there is a non-linear refraction, causing a phase change associated with the saturable absorption, in one path only, then the output of the device is non-zero. With a phase change in both paths however, the output of the device is zero. Hence ultrafast switching can be obtained by exciting both paths, with a time delay on the order of picoseconds, with a switch-off speed determined by the switch-on time of the saturable absorber. However, such devices are hampered by their complexity. Etalon configurations are arranged such that in the absence of any pump beam one of the Fabry-Perot transmission peaks is on the low frequency side of the exciton resonance. Any pump beam will cause a change in the refractive index of the material, shifting the transmission peak of the etalon, and reducing the transmission of a signal beam tuned to the etalon transmission peak. Migus et. al. [8.8] have performed optical logic gate operations using multiple quantum well etalons at room temperature, where the large excitonic refractive index change was utilised, although the recovery was determined by the carrier lifetime.

The use of low temperature growth [8.9] or ion implantation [8.10] can reduce the carrier lifetime to several hundreds of femtoseconds, at the expense of a weakening of the exciton absorption peak, alternatively, the carriers may be swept out in an electric field [8.11]. A different approach is to use multiple quantum well self-electrooptic devices (SEED's) [8.12-8.14]. Although the fastest SEED's can be switched in about 4ps, they need an electrical bias in addition to the control light pulses.

Another alternative method of eliminating the effect of slow carrier lifetimes is to make use of the ultrafast relaxation of the electron spin. This was first demonstrated by Nishikawa et. al. [8.15, 8.16] and will now be described in some detail.

8.3 Spin dependent refractive index change

Recent experiments on polarisation switching by several researchers [8.17, 8.18] have concentrated on waveguide structures. In waveguides, polarisation rotation is observed when light with linear polarisation is launched into a waveguide whose TE and TM axes have different refractive indices. If the light is launched at some angle relative to the axes of the waveguide, the TE and TM fields of the light will experience unequal refractive indices as they propagate through the waveguide. After propagation, one field will be retarded relative to the other, giving a combined polarisation state of the transmitted fields that is generally a rotated elliptical state. If the refractive index of such a waveguide has an intensity dependent component, the induced phase shift will also be a function of the intensity, allowing an intensity dependent switch to be achieved.

A different approach, making use of the spin-dependent non-linearity found in quantum wells, has been pioneered by Nishikawa et. al. [8.15]. They made use of a spin-dependent excitonic refractive index change that they observed in GaAs quantum wells.

Nishikawa showed that spin polarised material can give a refractive index difference between left and right circularly polarised light. Figure 8.1 shows schematically the electric fields of left and right circularly polarised components of a linearly polarised probe beam either with or without the presence of a net spin polarisation of carriers. With no net spin polarisation, the left and right circularly polarised components are the same in the y -axis at all z . With a net spin up (down) polarisation, however, the phase of the left (right) circularly polarised component changes, causing a phase difference between the two components, which grows as the light travels in the MQW along the z -axis. After travelling through the MQW the sum of the electric field components becomes a rotated elliptical polarisation as shown in figure 8.1. This polarisation change remains only when there exists a refractive index difference between the two circularly polarised components, and returns to the initial polarisation as the spins relax to equilibrium. Hence, when an analyser is inserted, set perpendicular to the initial probe polarisation, a signal will be obtained while the spin polarisation exists. This approach allows optical polarisation switching to be achieved without either the need to fabricate semiconductor material into waveguides or any of the associated coupling difficulties. A switch of this type with a time constant of 7ps has been demonstrated in a GaAs multiple quantum well etalon by Nishikawa et. al.

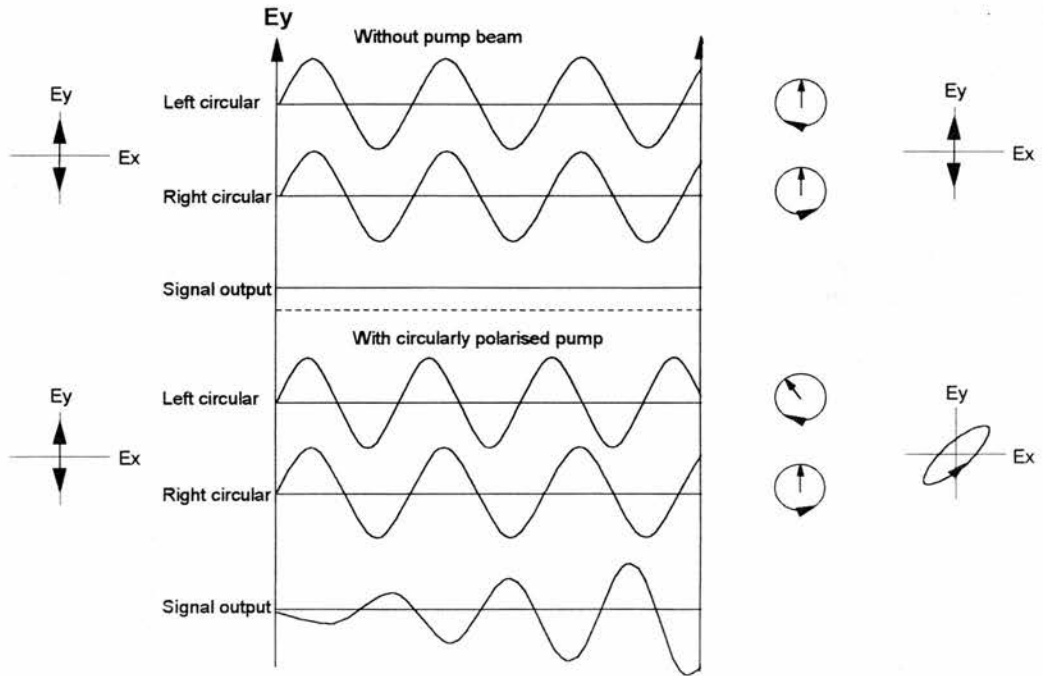


Figure 8.1 Schematic electric field components of light in the y -axis propagating through a MQW. Sine curves show the phases of the left and right circularly polarised components of a probe beam both with and without a circularly polarised pump beam.

8.4 Experimental details

Studies of all optical polarisation switching in InGaAs(P)/InGaAsP multiple quantum wells were carried out at room temperature using the experimental set-up shown in figure 3.8, with the modifications shown in figure 8.2.

The probe pulses were linearly polarised, while the pump pulses remained circularly polarised. An analyser, configured to transmit light polarised orthogonally to the linearly polarised probe pulses, was inserted after the samples, to discriminate between the “on” and “off” states.

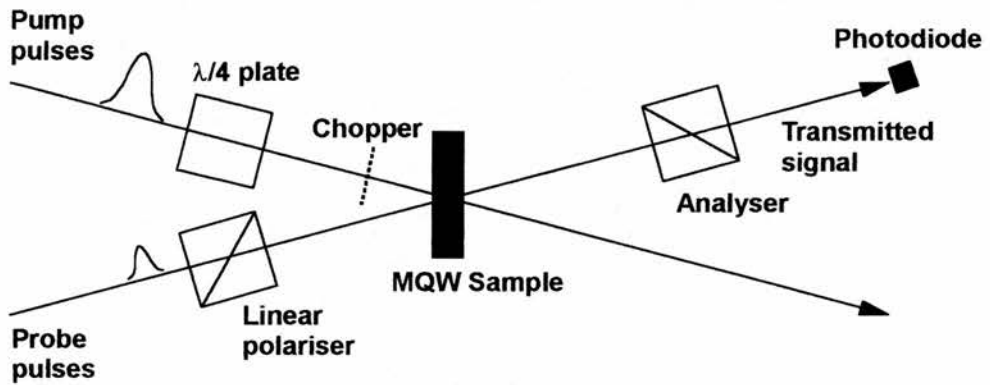


Figure 8.2 Modifications to experimental set-up of figure 3.8 to investigate all optical polarisation switching.

8.5 Results

The experiment was carried out in the two samples previously determined to have the slowest and fastest spin relaxation rates. They were MR850 (spin relaxation time of 20ps) and MR611 (spin relaxation time of 5.7ps) respectively. The time evolution of the switched probe signal, obtained by monitoring the transmission through the analyser as a function of probe delay, and the switching time window, measured at the FWHM of the transient transmission, was measured and is shown for each sample in figures 8.3 and 8.4. The results are summarised in the table 8.1.

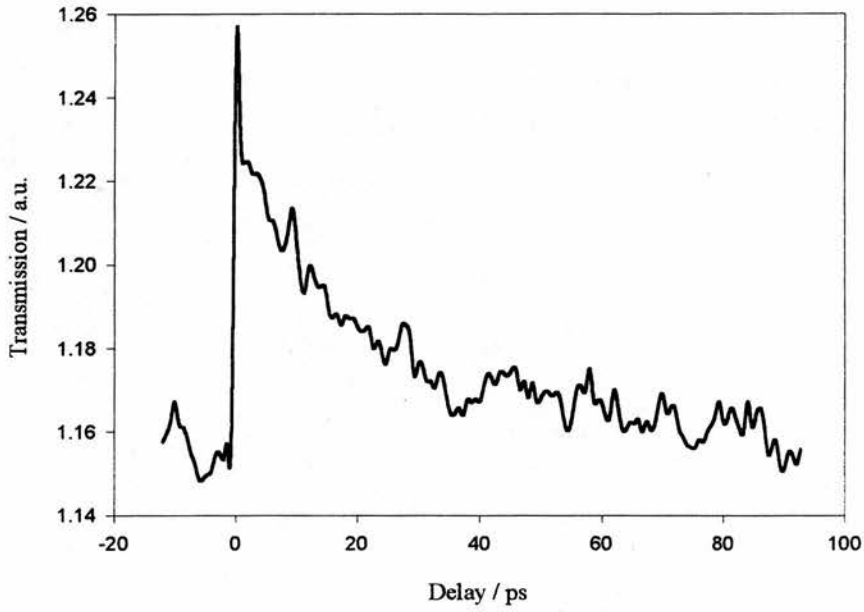


Figure 8.3 Switching signal of polarisation switch using sample MR850 with an average probe power of 1.5mW.

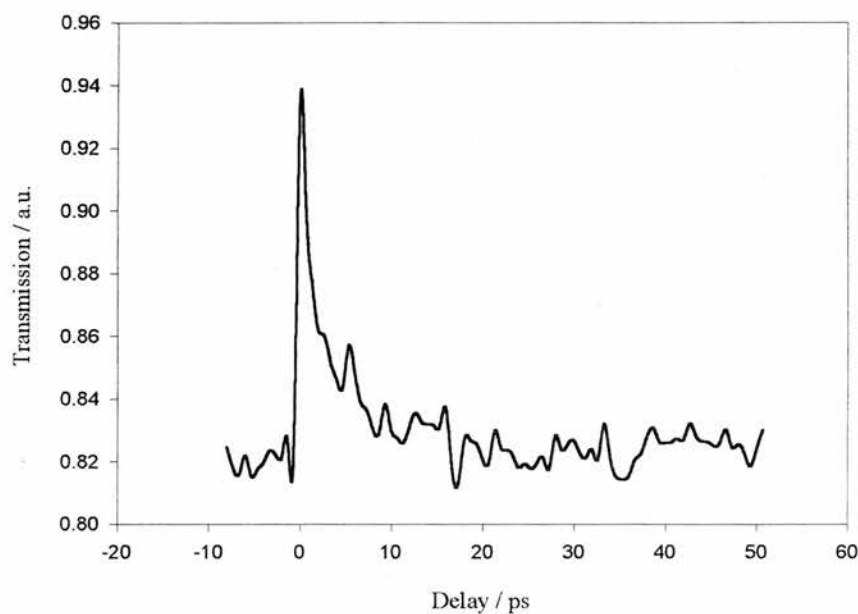


Figure 8.4 Switching signal of polarisation switch using sample MR611 with an average probe power of 1.5mW.

| Sample | Well width (nm) | Spin relaxation time (ps) | Switching time window (ps) | Switching time (ps) |
|---------------|------------------------|----------------------------------|-----------------------------------|----------------------------|
| MR850 | 9.5 | 20 | 8 | 20 |
| MR611 | 5.5 | 5.7 | 1.8 | 4.8 |

Table 8.1 Switching times and switching time window duration.

The power dependence of the induced polarisation change was examined by measuring the power output through the analyser as it was rotated through 360°, giving a

measure of the polarisation rotation of the signal output as a function of pump power. The polarisation rotation is plotted as a function of excited carrier density, assuming an internal quantum efficiency of one, for samples MR850 and MR611 in figures 8.5 and 8.6 respectively.

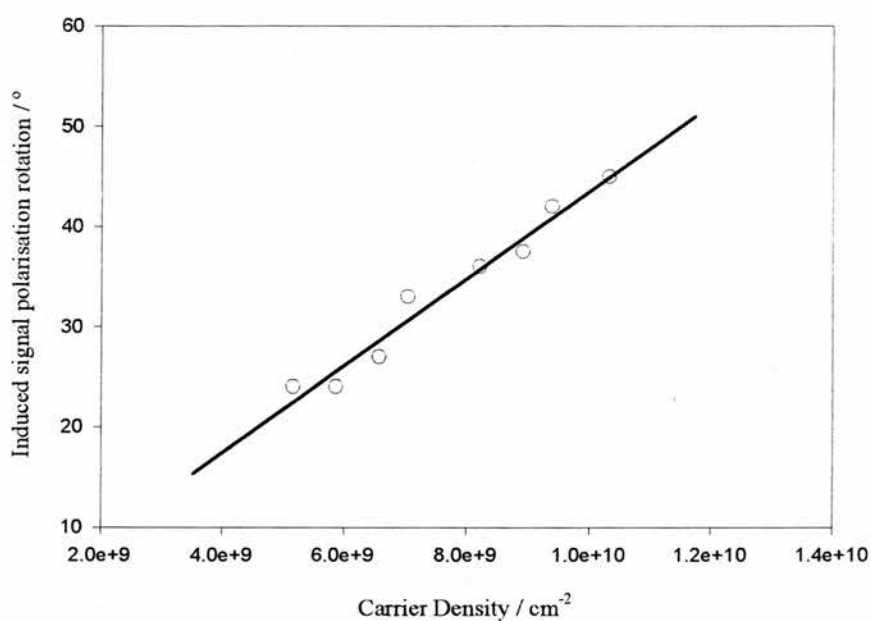


Figure 8.5 *Induced polarisation rotation of signal pulses as a function of carrier density in sample MR850.*

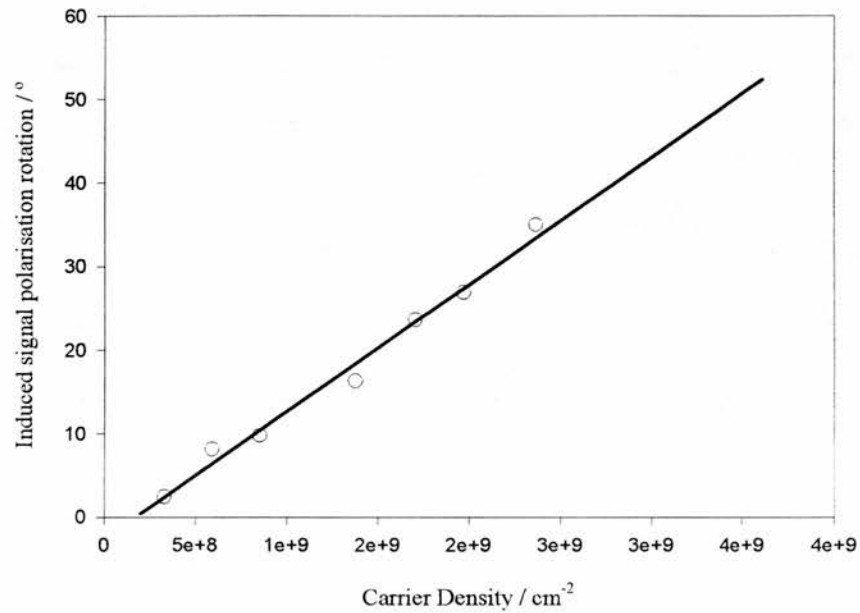


Figure 8.6 Induced polarisation rotation of signal pulses as a function of carrier density in sample MR611.

8.6 Modelling of polarisation switching

The attraction of polarisation switches is the large contrast available between the 'on' and 'off' states. In principle the transmitted signal should be zero in the 'off' state. However in practice, leakage through the polariser gives a background signal of typically a few percent. Optimum performance is achieved with a polarisation rotation of 90°. An optimised structure, which would produce this condition at the lowest pulse energies, requires a compromise between sufficient optical path length to produce the required

phase change and optical loss due to absorption. A model has been developed to determine the optimum structure for a polarisation switch of the type described.

The modelling of the switch is treated phenomenologically, solving three simultaneous rate equations to give a complete description of the output state for varying initial conditions. The rate equations describe the evolution of the pump and probe signals as they propagate through the MQW used in the switch. To a first order approximation the evolution of the circular pump beam is given by

$$\frac{dI_p(z)}{dz} = -\alpha_0 I_p(z) \quad (8.2)$$

where $I_p(z)$ is the pump intensity, α_0 is the absorption coefficient of the sample and z is the propagation direction.

The linear probe beam is split into two opposite circular polarised field components, F_s^+ denoting the component with the same circular polarisation as the pump beam and F_s^- denoting opposite circular component respectively. A first order approximation of the evolution of the same circular component is given by

$$\frac{dF_s^+(z)}{dz} = -(\alpha_0 + I_p(z)[\alpha_1 + \gamma i])F_s^+(z) \quad (8.3)$$

where $\alpha_1 + \gamma i$ is an intensity dependent modification to the absorption coefficient. The effect of this modification is to reduce the absorption coefficient 'seen' by the same circular component of the probe field, while the complex part controls the phase change of the probe field.

The evolution of the opposite circular component of the probe beam is governed by the simpler first order approximation

$$\frac{dF_s^-(z)}{dz} = -\alpha_0 F_s^-(z) \quad (8.4)$$

and the model then solves equations 8.3 and 8.4 and sums the fields to give the probe field at all z . To simplify the calculations the following assumptions are made. Firstly there is no interaction between either the pump or probe beams and the sample in the barrier material. Thus the propagation distance is directly proportional to the number of quantum wells through which the beams travel. Secondly, it is assumed that the absorption does not saturate, allowing α_0 to be determined from the linear transmission measurements of chapter 4. The magnitudes of α_1 and γ were inferred from the measurements of the switching signal and the induced rotation described previously.

8.6.1 Modelling results

The results of the modelling of the induced polarisation rotation for switching in samples MR850 and MR611 are plotted with the experimental results in figures 8.7 and 8.8. It can be seen that in both cases the model gives a good fit to the data. Given the quality of the fits the model was then used to determine the optimum interaction length, z , to switch a 1 mW signal beam and the signal output power for various estimated carrier densities in each sample. Example plots of the predicted output power against interaction length for a pump power of 10 mW, equivalent to carrier densities of $5 \times 10^{18} \text{ cm}^{-2}$ in sample MR850 and $1.55 \times 10^{18} \text{ cm}^{-2}$ in sample MR611, are shown in figures 8.9 and 8.10 for samples MR850 and MR611 respectively. Finally, plots of the predicted maximum output power and optimum interaction length against estimated carrier density are shown in figures 8.11 and 8.12 for samples MR850 and MR611 respectively.

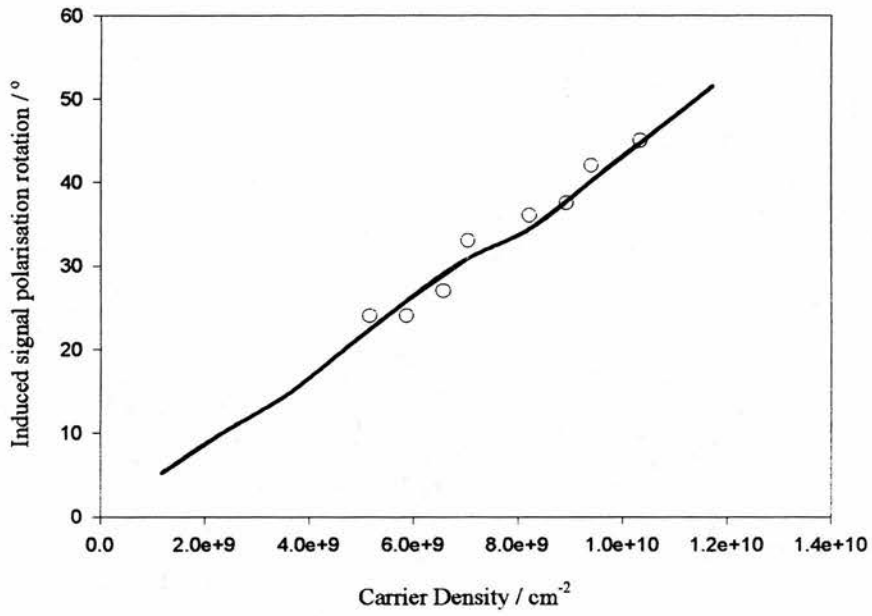


Figure 8.7 Modelled and measured signal polarisation rotation in sample MR850.

The circles show the measured data.

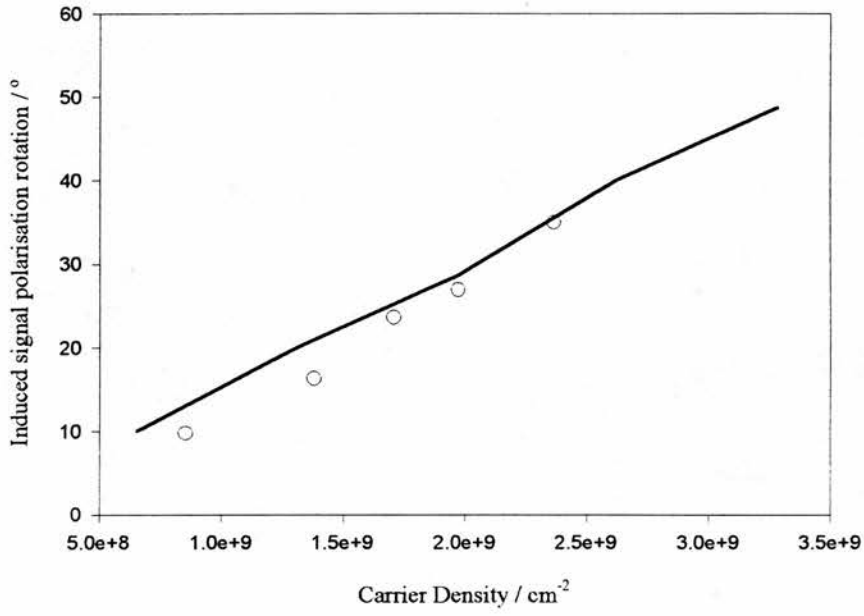


Figure 8.8 Modelled and measured signal polarisation rotation in sample MR611.

The circles show the measured data.

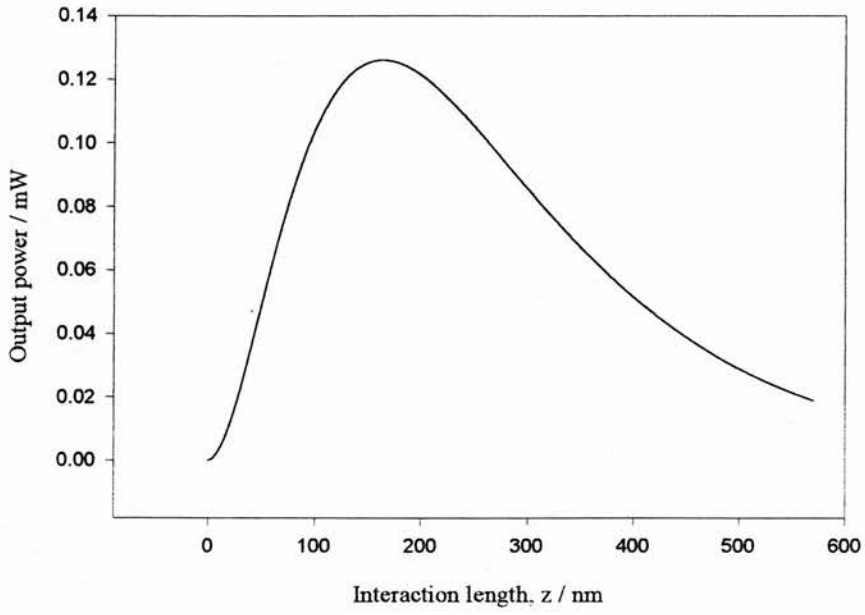


Figure 8.9 Modelled signal output power as a function of interaction length in sample MR850.

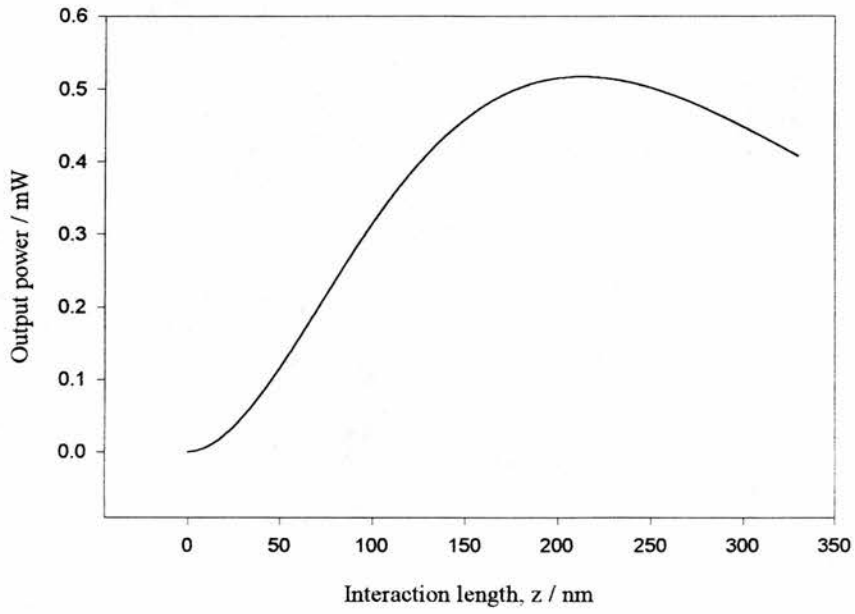


Figure 8.10 Modelled signal output power as a function of interaction length in sample MR611.

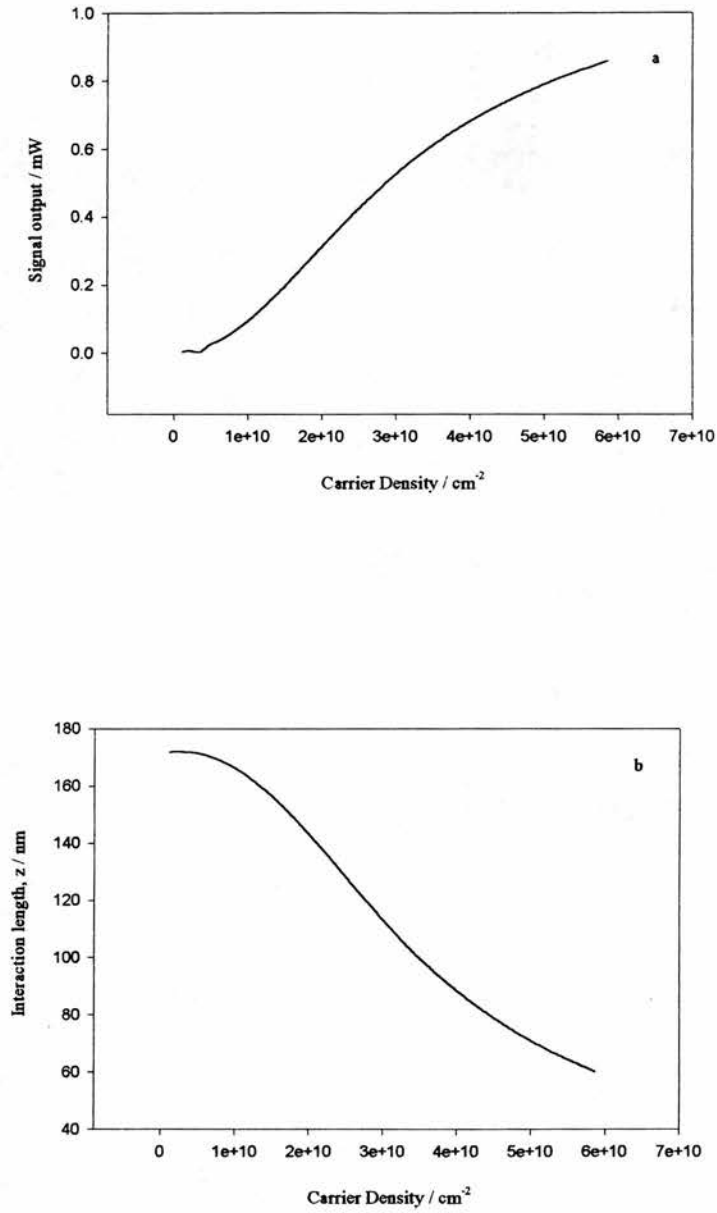


Figure 8.11 Modelled results showing: a, predicted maximum output power and b, optimum interaction length against pump power in sample MR850.

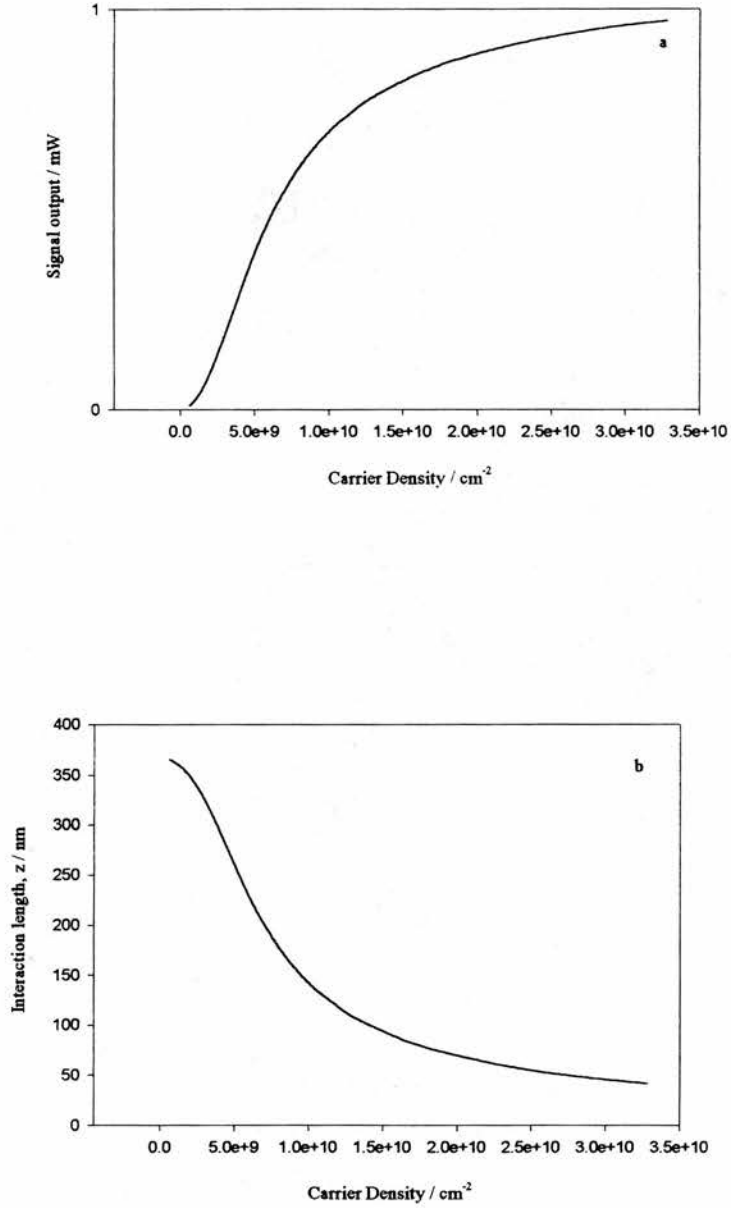


Figure 8.12 Modelled results showing: a, predicted maximum output power and b, optimum interaction length against pump power in sample MR611

8.7 Discussion

The attraction of polarisation switching is the potentially large contrast between the 'on' and 'off' states. In principle the transmitted signal should be zero in the 'off' state. However in practice, leakage through the polariser gives a background signal of typically a few percent. Optimum performance, therefore, would produce a rotation of 90° . An optimised structure, which would produce this condition at the lowest pulse energies, requires a compromise between sufficient optical path length to produce the required phase change and optical loss due to absorption. It is this optimised structure that the modelling is intended to determine. Given that the switching time, determined by the spin relaxation time, is dependent on the quantum well width, it is the number of quantum wells to provide the best balance between polarisation rotation and absorption that needs to be determined.

It can be seen from figures 8.9 and 8.10 that in both samples the optimum output occurs for an interaction length considerably shorter than that of the samples used. It is calculated that the optimum output for a pump power of 10 mW would occur with 17 quantum wells in sample MR850 and with 39 quantum wells in sample MR611.

Figures 8.11 and 8.12 show the modelled optimum output power and the optimum interaction length against estimated carrier density for each sample studied. It can be seen that as the carrier density increases the signal output tends towards 1 mW, which is a consequence of the first order approximations of the model. It is well known that the exciton resonance can never be completely saturated, thus there will always be some absorption of the signal beam. Figures 8.11 and 8.12 clearly show that at low pump powers, while the contrast of the polarisation switch may be good, the loss is extremely

large. For a pump power of 10 mW the loss in the switched signal, using an optimised device structure, would be 87.5% in sample MR850 and 48.4% in sample MR611.

The other attraction of using the spin-dependent nonlinearity in switching applications is that the switching time is independent of the carrier lifetime, and depends solely on the quantum well width. It should be noted, however, that while the switching time is independent of the carrier lifetime, the repetition rate remains restricted by this lifetime unless the carriers are swept out in an electric field [8.17]. It has been suggested, however, that even with this lifetime limitation such a polarisation switch could be applied to demultiplexing operations [8.16].

8.8 Conclusion

All-optical polarisation rotation switching has been demonstrated in samples MR850 and MR611. The switch on time in each case was essentially instantaneous while the exponential decay time was 20 ps for sample MR850 and 4.8 ps for sample MR611.

Modelling of the switching operation showed that throughput tended towards a maximum as the pump power was increased. However, it is clear that the powers required for such a result were in excess of both the damage threshold of the semiconductor samples, and significantly greater than the few milliwatts that would be available in any communications system. The throughputs of the signals switched by a pump power of 10 mW were determined to be 12.5% and 51.6% for samples MR850 and MR611 respectively.

8.9 References

- 8.1 S. Kawanishi, T. Morioka, O. Kamatani, H. Takara, J.M. Jacob, M. Sarawatari, "100 Gbit/s all-optical demultiplexing using four-wave mixing in a travelling wave laser diode amplifier", *Electron. Lett.*, **30**, 12, 981-982, (1994).
- 8.2 D. Hulin, A. Mysyrowicz, A. Antonetti, A. Migus, W.T. Masselink, H. Morkoc, H.M. Gibbs, N. Peyghambarian, "Ultrafast all-optical gate with subpicosecond On and OFF response time", *Appl. Phys. Lett.*, **49**, 13, 749-751, (1986).
- 8.3 R. Jin, J.P. Sozloff, P.A. Harten, C.L. Chuang, S.G. Lee, M. Warren, H.M. Gibbs, N. Peyghambarian, "Ultrafast modulation with subpicosecond recovery time in a GaAs/AlGaAs nonlinear directional coupler", *Appl. Phys. Lett.*, **56**, 11, 993-995, (1990).
- 8.4 J.S. Aitchison, A.H. Kean, C.N. Ironside, A. Villeneuve, G.I. Stegeman. "Ultrafast all-optical switching in $\text{Al}_{0.18}\text{Ga}_{0.82}\text{As}$ directional coupler in $1.55\mu\text{m}$ spectral region", *Electron. Lett.*, **27**, 19, 1709-1710, (1991).
- 8.5 K. Al-hemyari, J.S. Aitchison, C.N. Ironside, G.T. Kennedy, R.S. Grant, W. Sibbett. "ultrafast all-optical switching in GaAlAs integrated interferometer in $1.55\mu\text{m}$ spectral region", *Electron. Lett.*, **28**, 12, 1090-1092, (1992).
- 8.6 I. Glesk, J.P. Sokoloff, P.R. Prucnal, "Demonstration of all-optical demultiplexing of TDM data at 250 Gbit/s", *Electron. Lett.*, **30**, 4, 339-341, (1994).
- 8.7 S. Nakamura, K. Tajima, Y. Sugimoto, "Experimental investigation on high speed switching characteristics of a novel symmetric Mach-Zehnder all-optical switch", *Appl. Phys. Lett.*, **65**, 3, 283-285, (1994).
- 8.8 A. Migus, A. Antonetti, D. Hulin, A. Mysyrowicz, H.M. Gibbs, N. Peyghambarian, J.L. Jewell, "One picosecond optical NOR gate at room

- temperature with a GaAs/AlGaAs multiple quantum well nonlinear Fabry-Perot etalon”, *Appl. Phys. Lett.*, **46**, 1, 70-72, (1985).
- 8.9 E.S. Harmon, H.R. Melloch, J.M. Woodall, D.D. Nolte, N. Otsuka, C.L. Chang, “Carrier lifetime versus anneal in low temperature growth GaAs”, *Appl. Phys. Lett.*, **63**, 16, 2248-2250, (1993).
- 8.10 H.H. Wang, J.F. Whitaker, H. Fujioka, Z. Liliental-Weber, “Arsenic implanted ion implanted GaAs as an ultrafast photoconductor”, *Tech. Dig. Ultrafast electronics and optoelectronics, OSA Topical Meeting*, (1995).
- 8.11 J. Hyland, G. T. Kennedy, A. Miller. “Electron spin relaxation in InGaAs/InGaAsP multiple quantum wells”, *Tech. Dig. QE13 Cardiff*, 85, (1997).
- 8.12 A.L. Lentine, D.A.B. Miller, J.E. Henry, J.E. Cunningham, L.M.F. Chirovsky, “Multistate self-electrooptic effect devices”, *IEEE J. Quant. Electron.*, **25**, 8, 1921-1927, (1989).
- 8.13 A.L. Lentine, H.S. Hinton, D.A.B. Miller, J.E. Henry, J.E. Cunningham, L.M.F. Chirovsky, “Symmetric self-electrooptic effect device: optical set-reset latch, differential logic gate, and differential modulator/detector”, *IEEE J. Quant. Electron.*, **25**, 8, 1928-1936, (1989).
- 8.14 J. Feldmann, K.W. Goossen, D.A.B. Miller, A.M. Fox, J.E. Cunningham, W.Y. Jan, “Fast escape of photocreated carriers out of shallow quantum wells”, *Appl. Phys. Lett.*, **59**, 1, 66-68, (1991).
- 8.15 Y. Nishikawa, A. Tackeuchi, S. Nakamura, S. Muto, N. Yokoyama. “All optical picosecond switching of a quantum well etalon using spin polarisation relaxation”, *Appl. Phys. Lett.*, **66**, 7, 839-841, (1995).

- 8.16 Y. Nishikawa, A. Tackeuchi, M. Yamaguchi, S. Muto, O. Wada. "Ultrafast all-optical spin polarisation switch using quantum-well etalon", *IEEE J. Sel. Top. Quant. Electron.*, **2**, 3, 661-667, (1996).
- 8.17 P.A. Snow, I.E. Day, I.H. White, R.V. Penty, H.K. Tsang, R.S. Grant, Z. Su, W. Sibbett, J.B.D. Soole, H.P. Leblanc, A.S. Gozdz, N.C. Andreadakis, C. Caneau. "Demonstration of polarisation rotation gate in GaAs/AlGaAs multiquantum well waveguides", *Electron. Lett.* **28**, 25, 2346-2348, (1992).
- 8.18 I.E. Day, P.A. Snow, Z. Jiang, R.V. Penty, I.H. White, D.A.O. Davies, M.A. Fisher, M.J. Adams. "Low power all-optical polarisation gate switch in a passive InGaAsP MQW waveguide at 1.53 μm ", *Electron. Lett.* **30**, 13, 1050-1051, (1994).
- 8.19 P. LiKamWa, A. Miller, J.S. Roberts, P.N. Robson, "130ps recovery of all-optical switching in a GaAs multiquantum well directional coupler", *Appl. Phys. Lett.*, **58**, 19, 2055-2057, (1991).

Chapter 9 Conclusions

An investigation into the dynamics of exciton saturation in InGaAs(P) / InGaAsP multiple quantum well semiconductors at room temperature has been carried out using both picosecond and femtosecond laser pulses from a synchronously pumped PPLN OPO and a KCl:Tl⁰(1) colour-centre laser respectively. The optical selection rules in multiple quantum wells allowed the creation of spin polarised populations of carriers using circularly polarised light. Varying the polarisation states of both pump and probe beams causes the saturation effects of phase space filling to be enhanced or negated.

Degenerate pump-probe experiments employing circularly polarised beams were used to study exciton saturation mechanisms. Experiments were carried out with pulses of bandwidth both greater and smaller than the heavy hole exciton linewidth to distinguish the effects of lineshape broadening from those of Coulomb screening and phase space filling. It was found that exciton lineshape broadening was insignificant in the samples studied.

The studies carried out with pulses of bandwidth greater than the exciton linewidth removed any residual effect of broadening on the transmission of the probe beam, while the spin dependent nature of the phase space filling non-linearity allowed the saturation effects of Coulomb screening and phase space filling to be compared. The time resolution of the system allowed room temperature exciton-exciton saturation effects to be observed. Fitting of the data with a rate equation analysis allowed all the saturation mechanisms to be directly compared. The data suggested that the saturation contributions from free carrier screening and exciton-exciton screening were of equal magnitude. The different temperature dependencies of the screening efficiencies of each particle set oppose this

conclusion. Hence, further studies will be necessary to produce a more complete theoretical description of exciton saturation.

The dynamics of electron spin relaxation have been studied as a function of the quantum well width. The results were compared with those of a number of different authors and show good agreement. The fact that results from samples from different sources show good agreement suggests that at room temperature the main scattering mechanism leading to spin relaxation is due to LO-phonon collisions rather than impurity or interface scattering. Combining the results allowed the power dependence of the spin relaxation rate on the electron confinement to be determined. The spin relaxation rate was found to fit a 1.19 power dependence which, in conjunction with the inverse bandgap dependence of the spin relaxation times, implied that the D'Yakonov-Perel mechanism for spin relaxation is the dominant spin flip mechanism for electrons in InGaAs(P) / InGaAsP quantum wells at room temperature, in good agreement with results previously obtained in GaAs / AlGaAs quantum wells. Knowledge of the dependence of the spin relaxation time on well width is important for future device applications.

The spin dependent non-linearity was utilised to demonstrate ultrafast all optical polarisation switching in two of the samples studied. Circularly polarised pump pulses were used to control the transmission of linearly polarised probe pulses through an orthogonally oriented polariser positioned after the sample under investigation. All-optical polarisation switching has been demonstrated with a recovery time of 20 ps for sample MR850 and 4.8 ps for sample MR611. Modelling of the switching operation showed that the probe throughput tended towards 100% as the pump power was increased. However, it was clear that the pump powers required for such a result were in excess of both the damage threshold of the semiconductor samples, and significantly greater than the few milliwatts that would be available in any communications system. The throughputs of the

signals switched by a pump power of 10 mW were determined to be 12.5% and 51.6% for samples MR850 and MR611 respectively.

In summary, this work has shown novel characterisation of the optical properties of InGaAs(P) / InGaAsP multiple quantum wells, allowing the complete separation of the contributions of Coulomb screening, broadening and phase space filling to exciton saturation. The electron spin relaxation time has been shown to agree with the D'Yakonov-Perel mechanism and the first demonstration of an electron spin dependent all-optical polarisation switch in this material system has been achieved.

Chapter 10 Publications

10.1 Journal publications

“Picosecond all optical polarisation switching in InGaAsP MQW’s at 1.52 μm .”

J. T. Hyland, G. T. Kennedy & A. Miller.

Photonics Technology Letters, **10**, 10, pp 1419 (1998).

“Spin relaxation and all optical polarisation switching in InGaAs(P) / InGaAsP multiple quantum wells.”

J. T. Hyland, G. T. Kennedy, A. Miller & C. C. Button.

Semiconductor Science and Technology, March 1999 (To be published).

10.2 Conference publications

“All optical polarisation sensitive switching in multiple quantum wells at 1.5 microns.”

J. T. Hyland.

The Rank Prize Funds Mini Symposium on Devices and Systems for Optical Interconnects and Data Links, Sept 1-4, 1997.

“Electron spin relaxation in InGaAs / InGaAsP multiple quantum wells.”

J. T. Hyland, G. T. Kennedy & A. Miller.

QE13, Cardiff, Sept 9-11, 1997.

“Spin relaxation and all optical polarisation switching in MQWs.”

J. T. Hyland (Invited Talk).

Scottish Chapter of LEOS Meeting on Electro-Optic Devices and Systems, University of Edinburgh, Jan 28, 1998.

“Exciton saturation mechanisms resolved in room temperature $\text{In}_{1-x}\text{Ga}_x\text{As}_y(\text{P}_{1-y})$ / InGaAsP multiple quantum wells at $1.5\mu\text{m}$.”

J. T. Hyland, G. T. Kennedy & A. Miller.

Paper QWC70, Cleo/Europe-EQEC, Glasgow, Sept 13-18, 1998.

“Spin relaxation and all-optical polarisation switching in InGaAsP multiple quantum wells at $1.55\mu\text{m}$.”

J. T. Hyland, G. T. Kennedy, A. Miller & C. C. Button.

Paper QtuA4-1, Quantum Electronics, Snowmass, April 12-13, 1999.

“All-optical polarisation switching at $1.5\mu\text{m}$ in $\text{In}_{1-x}\text{Ga}_x\text{As}_y(\text{P}_{1-y})$ -InGaAsP multiple quantum wells.”

J. T. Hyland, G. T. Kennedy, A. Miller & C. C. Button.

Paper CThF3, CLEO / QELS, Baltimore, May 23-28, 1999.

Chapter 11 Acknowledgements

I would like to thank my supervisor Professor Alan Miller for his support, encouragement and guidance throughout this project and for sending me to Bulgaria. Thanks must also go to Professor Wilson Sibbett and the “W-squad” for letting me squat in their labs for so long.

Special thanks to Alasdair Cameron and Steve French for setting the ball rolling and to Mark Holden for keeping it going, without ever getting depressed or angry.

A special mention must go to Gordon Kennedy for holding my hand with the colour-centre laser for so long and to Michael Mazilu for patiently answering my obvious questions, helping with all the modelling and for learning all those rude words.

Thanks to all the “new boys”, Dawn, Jonathan, Vesselin and Steve, for putting up with me, especially for the last few months. Extra special thanks to Steve for the Bulgarian experience.

Thanks also to the technical staff, especially Reg, for supplying me with liquid nitrogen and understanding my drawings and a special mention must go to Moira Mackenzie for my flexible working hours and all those crosswords.

I should also thank everyone else who has made my stay in St. Andrews so enjoyable. Thanks to the secretaries for all the faxing, and for letting me see Alan from time to time, Ian and Alan for all those nights in the pub, Alan, Neil and Jonathan for all the mountains, Dave for the football tips and the other five-a-siders for overlooking my enthusiastic tackles, Neil and Ian for supporting teams worse than mine and especially Andrew, for cooking when I couldn't be bothered, listening to my whinging and for cleaning the bathroom.

Thanks to my family, who never really understood what I did but still took an interest, if only to check I was eating properly.

Finally I would like to thank Lisa, without whose love and support this thesis would never have appeared.

Thanks everyone, I couldn't have done it without you!

I am grateful to the Engineering and Physical Sciences Research council for financial support.